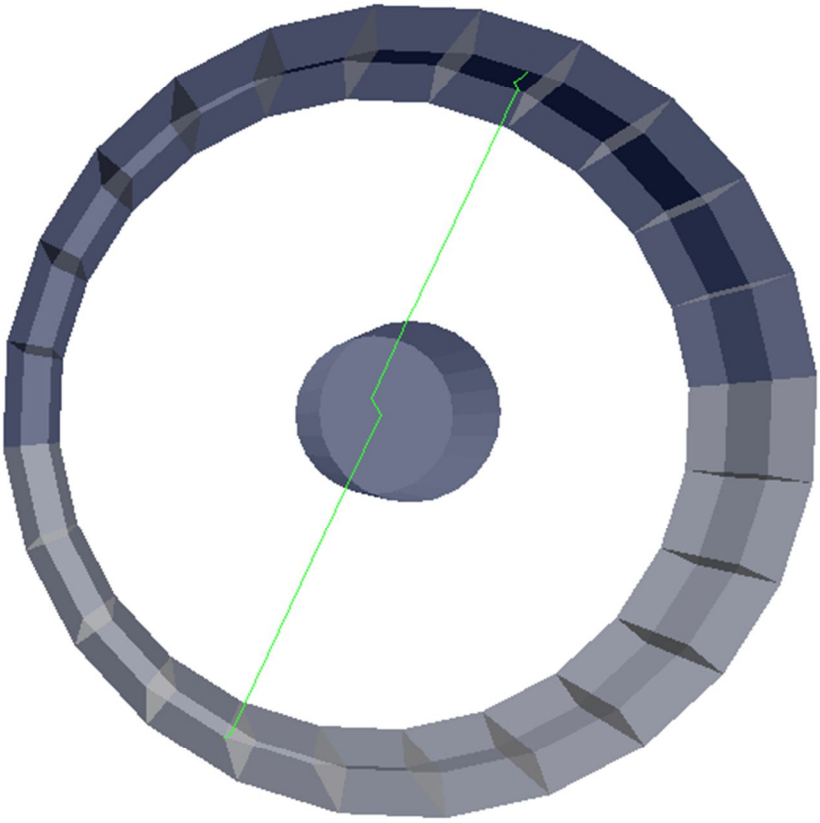

Susana Margarida Vieira da Silva

Study of Compton Scattering in PET

Supervisor Prof. Dr. Vitaly Chepel

Master of Science in Biomedical Engineering
Faculty of Sciences and Technology of the University of Coimbra

September 2011

· U C ·

UNIVERSIDADE DE COIMBRA

University of Coimbra

Faculty of Sciences and Technology

Department of Physics

Study of Compton Scattering in PET

Susana Margarida Vieira da Silva

Coimbra, 2011

Study of Compton Scattering in PET

M. Sc. dissertation

Susana Margarida Vieira da Silva

To obtain the degree of

Master of Science in Biomedical Engineering

Coimbra, Portugal

2011

Scientific Supervisor: Prof. Dr. Vitaly Chepel
In collaboration with: LIP - Coimbra

Submission date: 2011 – 09 – 05

Contents

List of Figures

List of Tables

List of Acronyms and Abbreviations

[^{11}C]PiB	Pittsburgh compound B
6-OH-BTA	([*N*methyl-] 2-(4'-methylaminophenyl)-6-hydroxybenzothiazole)
APDs	Avalanche Photodiodes
BaF_2	Barium Fluoride
BGO	Bismuth Germanate
CAT	Computerized Axial Tomography
CCD	Charge-Coupled Device
CT	Computed Tomography
DOI	Depth of Interaction
FBP	Filtered Backprojection
FDG	2-[^{18}F]fluoro-2-deoxyglucose
FORE	Fourier Rebinning
GSO	Gadolinium Silicate
ICNAS	Instituto de Ciências Nucleares Aplicadas à Saúde
$LaBr_3$	Lanthanum(III) Bromide
LOR	Line of Response
LSO	Lutetium Oxyorthosilicate
LXe	Liquid Xenon
LYSO	Lutetium Yttrium Orthosilicate
MCP-PMT	Micro-Channel Plate PMT
MGH	Massachusetts General Hospital
MLEM	Maximum-Likelihood Expectation Maximization
MPPC	Multi-pixel Photon Counter
MRI	Magnetic Resonance Imaging
NaF	Sodium Fluoride
NaI(Tl)	Sodium Iodide

OSEM	Ordered-Subset Expectation Maximization
PEM	Positron Emission Mammography
PET	Positron Emission Tomography
PHA	Pulse Height Analyzer
PMT	Photomultiplier tube
PS-PMT	Position Sensitive Photomultiplier Tube
PSD	Pulse Shape Discrimination
RP	Radiopharmaceutical
SiPM	Silicon Photomultipliers
SNR	Signal to Noise Ratio
SSRB	Single Slice Rebinning
TOF	Time-of-Flight
VLPC	Visible Light Photon Counters
VRML	Virtual Reality Modeling Language
WLS-fibers	Wave Length-shifting fibers

Abstract

Positron Emission Tomography, PET, is nowadays a widely spread nuclear imaging technique, being the imaging modality of choice for cancer detection. Its importance not only in clinical oncologic applications, but also in cardiology, neurology, and other research investigations, makes studies that procure to enhance performance of PET tomographs of great interest. The purpose of the present thesis is to study the feasibility of using Compton scattered events in the detectors for image reconstruction. Since traditional modern PET systems only make use of the coincident pairs of gamma photons that undergo photoelectric effect on the first interaction with the detector crystals, the possible advantages of including the scattered events are a significant increase of the image statistic, and reduction of radiation dose received by the patient.

The computational methods used in this work include an algorithm for parent gamma rays identification for those events that consist of several interactions with the detector, and two Compton tracing algorithms that decide which of the measured interactions is likely to be the first interaction with the detector. The first Compton tracing method consists in choosing the interaction sites that are closer to the center of the tomograph, and the second consists in choosing those that result in the shortest line of response. The obtained results suggest that using of the scattered in the detector events allows to increase counting statistic without significant degradation of image contrast and true to scatter ratio. Of the two methods tested in this work, the first one presents better results.

Resumo

A Tomografia por emissão de positrões é actualmente uma técnica de imagiologia para medicina nuclear amplamente difundida em uso clinico, sendo o exame imagiológico de primeira escolha para a detecção de cancro. A sua importância não só em aplicações oncológicas, mas também em cardiologia, neurologia, e em investigação científica, fazem com que estudos que procuram o melhoramento de tomógrafos PET sejam de grande interesse. Sendo assim, esta tese visa o estudo da viabilidade do uso de eventos que sofreram dispersão Compton no detector para a reconstrução da imagem. Sabendo que os sistemas PET tradicionais apenas utilizam pares coincidentes de fotões gama que sofrem efeito fotoeléctrico na primeira interacção com os cristais do detector para a reconstrução da imagem, então as possíveis vantagens do uso de eventos de dispersão Compton no detector consistem num aumento significativo da estatística da imagem, e uma redução da quantidade de radiofármaco necessário injectar no paciente.

Os métodos utilizados a fim de realizar o objectivo proposto incluem um algoritmo de selecção do raio gama de proveniência para os eventos que consistem em várias interacções com o detector, e dois algoritmos de detecção do primeiro evento de dispersão Compton. O primeiro método consiste em escolher a interacção mais perto do centro do tomógrafo, o segundo método consiste em escolher os eventos que correspondem a uma linha de resposta mais curta. Os resultados obtidos sugerem que o uso dos eventos que foram dispersos no detector permite o aumento da estatística de contagem sem uma degradação significativa do contraste da imagem e do rácio entre os verdadeiros e os dispersos. Dos dois métodos testados neste trabalho, o primeiro método apresenta melhores resultados.

Acknowledgements

First of all I would like to thank my supervisor Prof. Dr. Vitaly Chepel, for all his scientific advises, explanations, and for always demonstrating much patience and availability. I would also like to thank all the other researchers and professors that aided in the project realization, with good suggestions and solutions.

A special thanks goes also to my parents and sister, for the continuous support, not only during this year, but also in the entire 5 years of the course. And for making it possible for me to obtain a master degree.

Finally, I would also like to express my gratitude to all my friends, especially the ones I met in Coimbra, for expressing interest in my work and for suggesting tips.

Chapter 1

Introduction

The present thesis aims to study the feasibility of Compton tracing in PET detectors, for the potential improvement of the PET image quality and reduction of patient injected radiation dose. This work has been done in the framework of a project carried out by LIP – Coimbra "Feasibility study of using Compton scattering for medical imaging with positrons" funded by Fundação para a Ciência e Tecnologia under the grant NºPTDC/SAU-BEB/67002/2006.

Positron Emission Tomography, PET, is a nuclear medicine imaging technique that makes use of positron-emitting isotopes for the detection of certain functional processes in the body. The idea of using these isotopes for studies of human metabolism was firstly proposed in the early 1950's by researchers at the Massachusetts General Hospital in Boston and the Duke University in Durham, however it was only in the beginning of the 1970's that the first PET systems emerged, at the time only as research tools. In 1976 the first commercial PET scanner was presented, and not many years later PET systems had already proven their potential for medical diagnosis [1]. Nonetheless, the elevated cost of the PET detection system, and the fact that a cyclotron nearby was required, held back its development and growth until the 1990's, when a radiopharmaceutical capable of tracing the glucose metabolism appeared, the fluorodeoxyglucose (FDG) [2].

Nowadays, PET is the imaging modality of choice for the detection of cancer. Its importance not only for diagnosis and pathology monitoring but also for investigation purposes, has promoted PET to one of the most important medical imaging techniques.

PET systems attain data from a body through the injection of a radiopharmaceutical in the patient. This is composed by a molecule of

interest for metabolic processes, for instance glucose, with one of the atoms replaced by a radioactive isotope. The radioisotope is responsible for releasing a positron ($\beta+$ particle) in the body, hence the name of the technique. The positron then experiences positron-electron annihilation with a nearby electron, and a pair of opposite 511 keV gamma rays is emitted. The detection of these two photons allows us to trace a LOR, line of response, and the collection of all the LORs retrieved in the scan is used for the reconstruction of the image.

Unlike CT or MRI, that provide precise morphological information about the body, this technique provides functional information. For that reason, PET is a complementary, not competitive, technique to CT and MRI, and thus most of the actual PET systems utilized in hospitals and health facilities are coupled with a CT system, forming a scanner called PET/CT that provides both anatomic and functional information of the body. PET/MRI coupled scans have recently become commercially available for clinical practice [3][4][5][6][7].

Nevertheless, PET systems are far from being at their full potential, and thus continuous development and studies that procure to enhance the performance of PET tomographs are of great interest. Most of the actual PET systems only make use of the coincident pairs of gamma rays that undergo photoelectric effect on the first interaction with the detector crystals, by selecting events within an energy window around 511 keV per gamma. However, the number of coincidences that satisfy this condition represents only a small percentage of all the detector interactions, and therefore a great number of coincidences is discarded.

It is known that for a 511 keV gamma photon the probability of occurrence of photoelectric effect in the first interaction with the scintillator crystal is usually no more than 50%, and the rest undergoes Compton scattering. For example in BGO scintillators the probability of occurrence is 40% for photoelectric effect and 60% for Compton scattering, whereas in LSO scintillators the probability is 32% for photoelectric effect and 68% for Compton scattering [8]. If both gamma rays are required to be detected through the photoelectric absorption, the number of coincidences is thus only 16% in BGO and about 10% in LSO detectors. Besides this, some emitted gamma rays escape the detector ring and others don't even reach it, being fully absorbed in the body. Considering all these facts, it is easy to conclude that most of the emitted gamma rays that reach the detectors are not used for the image reconstruction in the actual PET systems, and a great amount of the radioactivity injected in the patient turns out to be unutilized.

The main purpose of the present project is therefore to analyze the scattered events that occur in the PET detectors, and attempt to retrieve lines of response from those events. The study has been carried out using the Monte Carlo method in order to simulate the interaction of γ-rays with the object and the detector, as well as the detector response. Two algorithms were further applied to these data with the aim of identifying the probable first interaction with the detector for each of the two photons. The chosen pairs of interactions produce LORs, which are afterwards used for the reconstruction of images. The final aim is, therefore, to study the obtained reconstructed images, and by comparison, infer if it is feasible to use the events that do not experience photoelectric effect in the first interaction with the detector.

The present thesis is subdivided in five chapters that cover the necessary theory inherent to the realization of this project, as well as the performed methods, obtained results, and final conclusions. The first chapter introduces the actual context of PET scans and the relevancy of studying Compton scattering in detectors. Chapter two is dedicated to the theoretical concepts of PET imaging, explaining the physical principles of positron production and annihilation, the used technology, the radiation detection, the factors that affect PET systems performance, the image reconstruction methods along with corrections for better quality, the most important radionuclides and radiopharmaceuticals, and finally the tendencies for future PET generations. In the third chapter a deeper approach on photon detection and interaction with matter is done, so that our choice of algorithms for the project can be justified. Chapter four describes the data simulation tools, the methods and algorithms used for data processing, and the obtained results. At last, the fifth chapter presents the conclusions we obtained from realizing this project and a further discussion on future work.

Chapter 2

Positron Emission Tomography

As stated in the previous chapter, Positron Emission Tomography is a nuclear medicine imaging modality, applied in several fields but mainly in oncology, neurology, and cardiology [9]. This type of tomography differs from the traditional CT in the fact that it provides tissue functional or metabolic information instead of anatomic or structural information, making it a highly compelling imaging tool.

2.1 Basic Principles

Since PET scans require intrabody production of positrons, primarily it is necessary to produce an adequate pharmaceutical labeled with a positron-emitting radionuclide, which will work as a molecular probe inside the object of study. Afterwards, the prepared radiopharmaceuticals are administered to the patient, and certain amount of time before the scan is required so that the injected radiopharmaceuticals are absorbed throughout the body.

Positron-emitting radionuclides are neutron deficient isotopes [2] that stabilize through a radioactive decay known Beta Plus (β+) decay. In this process a proton transmutes into a neutron releasing both a positively charged particle known as β+ particle or positron, and an uncharged particle named neutrino (υ), [10] [11] as shown in the following equation:

$$p \rightarrow n + e^{+} + \upsilon_{e} \qquad (2.1)$$

Given this, the unstable atom that undergoes β^+ decay maintains the atomic mass number (N+Z), but the atomic number (Z) decreases by one unit while the number of neutrons increases one unit [10]:

$$ {}^{A}_{Z}X \rightarrow {}_{Z-1}{}^{A}Y + e^{+} + \upsilon_e \qquad (2.2) $$

After the decay, the released positron and neutrino carry the excess energy from the decay, in the form of kinetic energy. When passing through the surrounding matter, the positron gradually loses its kinetic energy via Coulomb interaction with the atoms constituting the medium. Two mechanisms of energy loss can be distinguished, one resulting in atomic ionizations and excitations (usually called collisional losses) while the other leading to the emission of photons by the positron due to its accelerated motion in the Coulomb field of atomic nucleus. The latter mechanism is also known as bremsstrahlung (figure 2.1). For electrons and positrons, collisional losses dominate at the energy lower than a few MeV, while bremsstrahlung becomes important at higher energies. The rate through which a particle loses its energy depends on the medium and is a function of particle energy. It can be quantified using the stopping power, dE/dx [15] [25] [55].

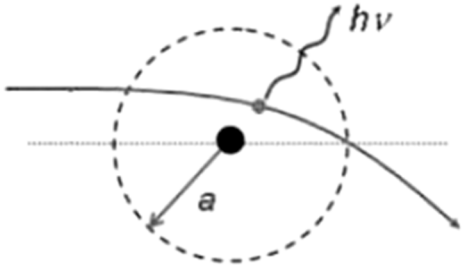

FIGURE 2.1: Bremsstrahlung emission. [15]

When the positron has lost all or almost all of its kinetic energy, it annihilates when colliding with an electron. The electron is the positron's antiparticle, they have the same rest masses ($E = m_e c^2 = 511keV$) and opposite charge (+ for positron, - for electron) [15]. The positron-electron annihilation process may occur directly, or through a transitional stage, where the positron-electron pair forms a quasistable system called positronium [10] [12], as illustrated in figure 2.2. The range that a positron is capable of achieving before annihilation depends on its emission energy and electron density of the surrounding tissue [2].

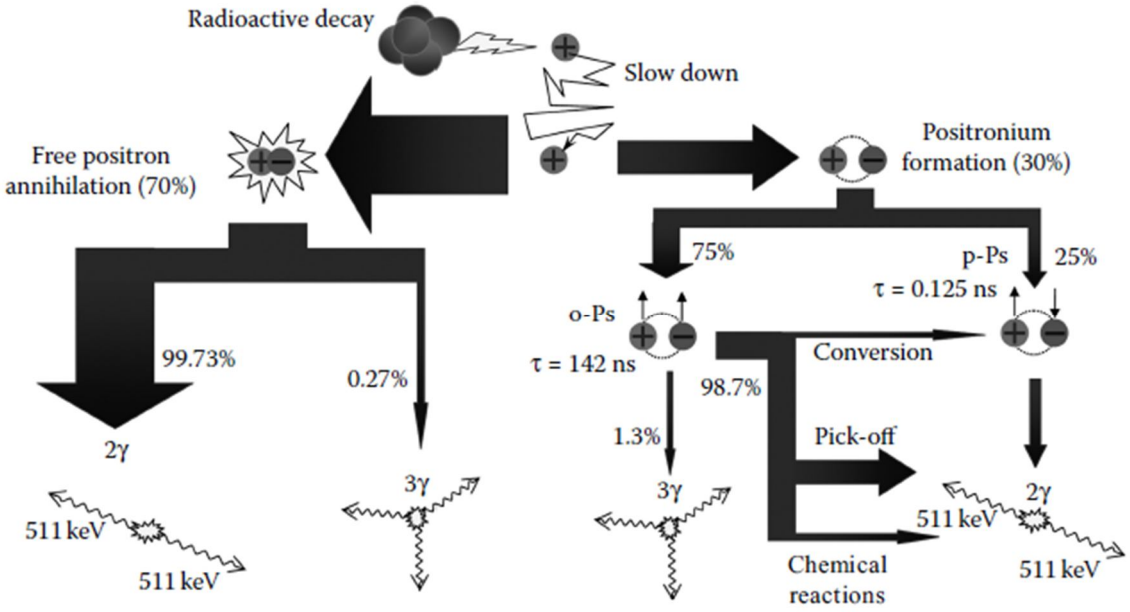

FIGURE 2.2: Positron interactions until annihilation in water. [13]

In the annihilation process, both light charged particles are destroyed, with a probability ~99%, and two collinear 511 keV photons are created, ensuring the total conservation of charge, energy ($2m_ec^2$=1.022MeV), and momentum (photons 180º apart) of the reaction [15].

The effective simultaneous detection of these two photons presents the basic functioning principle of PET imaging. Figure 2.3 resumes the events that lead to the final emission on the γ-rays pair.

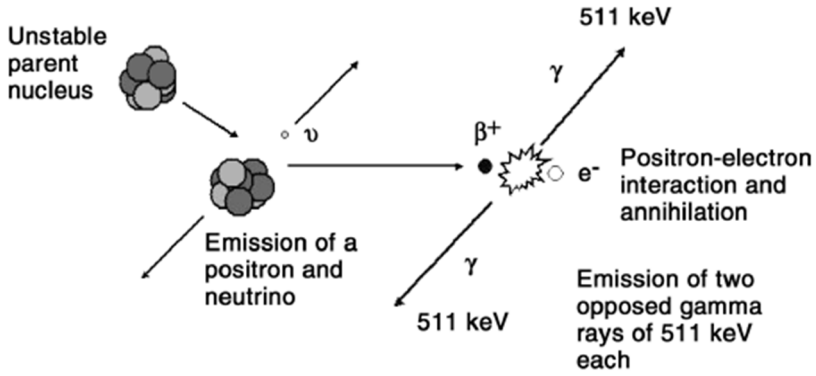

FIGURE 2.3: Event summary from positron emission to g-rays pair production. [10]

Thereafter, if both gamma rays reach the detector ring placed around the patient in two opposing detector sections, then a line where the annihilation occurred can be defined. This line is named Line of Response

and since both photons are produced simultaneously, then the pair detection requires a short coincidence timing window. The set of all successfully detected LORs constitutes the raw data that is afterwards used for image reconstruction. The example in figure 2.4 illustrates the resulting LORs of a region with high radiopharmaceutical concentration.

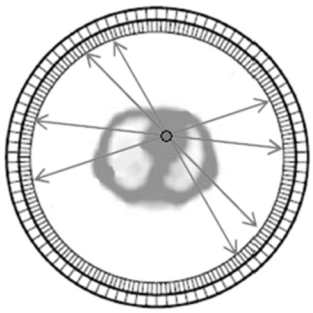

FIGURE 2.4: Example of resulting LORs for a region of high radiopharmaceutical concentration. [14]

2.2 Scanning systems and Instrumentation

The entire apparatus of a PET scanning system is constituted by various components, each responsible for a different function, either vital for the gamma rays detection or having a supporting role. PET scanners are composed by arrays of detector blocks, disposed most commonly in rings, usually from 18 to 32 rings [16], and less commonly in partial rings or in a hexagonal shape, surrounding the object of study. In addition to this, PET scanners are also composed by a moving bed, a computational system that stores and processes the acquired data, and the apparatus that physically supports the scanner, as exemplified in figure 2.5.

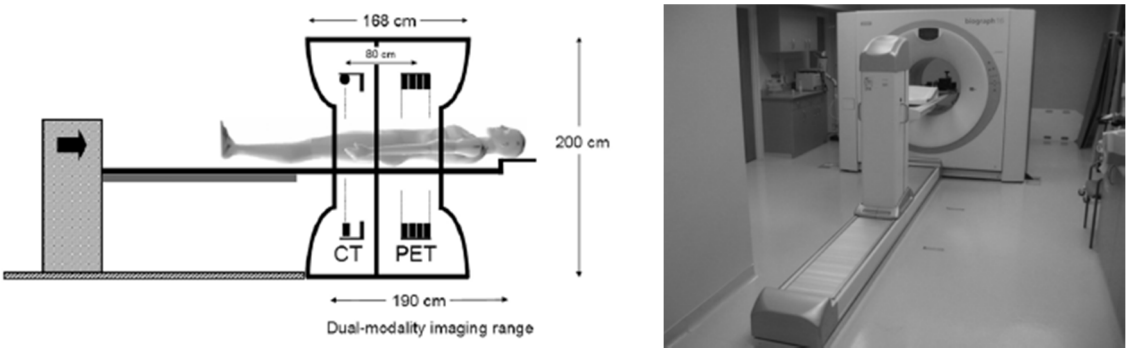

FIGURE 2.5: PET scanning apparatus; *Left* - Siemens PET/CT scanner design; [2] *Right* – PET scanner installed at ICNAS, Coimbra.

2.2.1 PET detectors

A detector ring is most commonly constituted by various block detectors. The traditional block detector proposed by Casey and Nutt in the 1980s, that has been in use for the last two decades [2], is constituted by a solid inorganic scintillation crystal partially divided in various equal elements with cuts of different depths, usually 64 cuts, as illustrated in figure 2.6 (a), and four photomultiplier tubes attached to the subdivided scintillator. The cuts in between the elements of the crystal are covered with an opaque reflective material that prevents light interference of an element to the other, but promotes light sharing in the PMTs. The relative light outputs (P_i) from each of the four PMTs, allow us to obtain the supposed location of the interaction of the photon in the detector block (*X* and *Y* coordinates), as equations 2.3 and 2.4 [14] indicate regarding figure 2.6 (b).

$$X = \frac{P_1 + P_2 - P_3 - P_4}{P_1 + P_2 + P_3 + P_4} \quad (2.3) \qquad Y = \frac{P_1 - P_2 + P_3 - P_4}{P_1 + P_2 + P_3 + P_4} \quad (2.4)$$

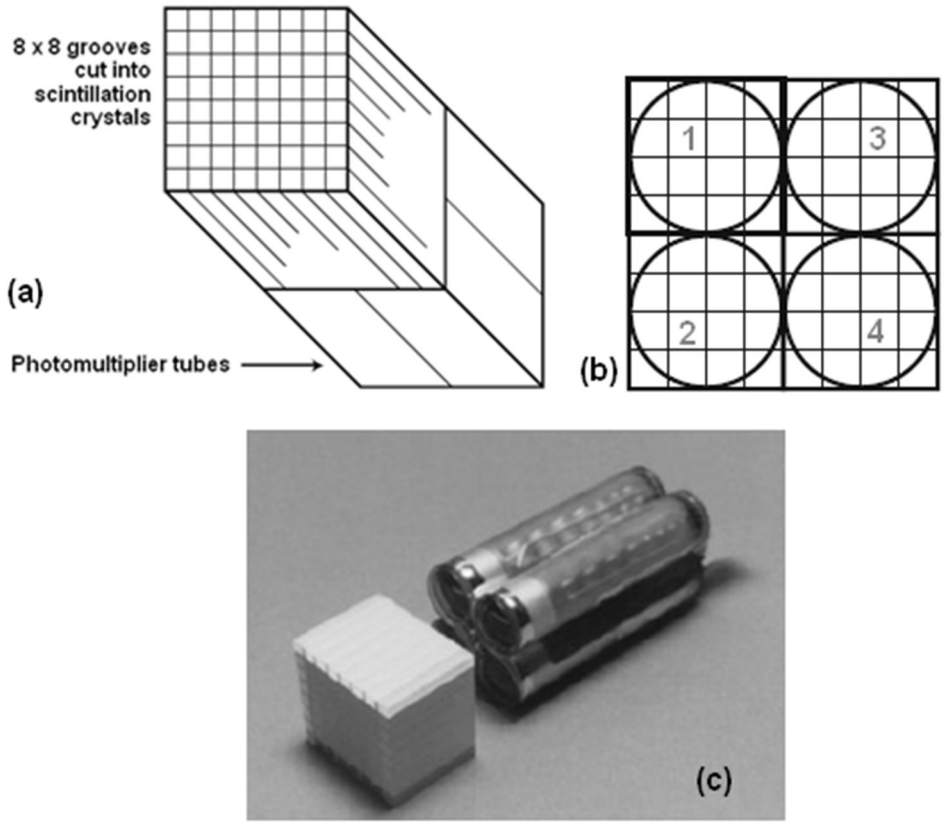

FIGURE 2.6: Block detector; *(a)* Scheme of a commercial block detector; [16] *(b)*Light quadrant sharing of PMTs; [16] *(c)* Photograph of block detector. [24]

2.2.1.1 Scintillators

The detection of incoming γ-rays starts when a photon that effectively reached the scintillator undergoes photoelectric effect in the crystal, depositing there all its energy. Nonetheless, that is not always the case, when a photon hits the scintillator it can interact via Compton scattering, via photoelectric effect or not interact at all [13], as illustrates figure 2.7. If the interaction takes place, the photon energy is transferred to a fast electron that gradually loses it in collisions with atoms and, in a lesser degree, through bremsstrahlung.

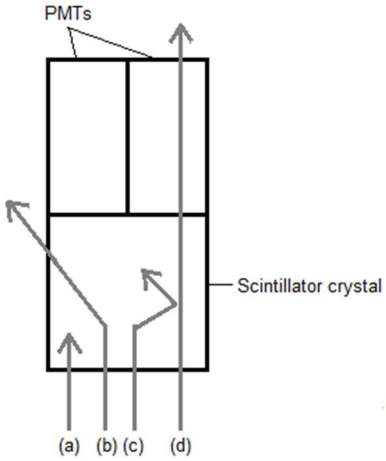

FIGURE 2.7: Probable interactions of a photon with a scintillator; [10] [13] *(a)* photoelectric effect; *(b)* Compton scattering; *(c)* Multiple Compton scattering and final photoelectric effect; *(d)* photon escapes the detector.

In the inorganic scintillation materials, electrons only have available discrete bands of energy, the valence band (lower energy), representing the orbital electrons of atoms, and the conduction band (higher energy), representing the electrons that are free in the crystal. When the incoming gamma ray deposits its energy in the crystal, some electrons from the valence band gains enough energy to ascend to the conduction band, leaving holes in the valence band [12]. When this electron returns to the valence band it emits energy in the form of a photon in the visible light range, which is then detected by the PMTs. Figure 2.8 illustrated this process. Since light photon emission is a rather inefficient process in the pure crystal form, small quantities of impurities called activators are frequently added to scintillators to enhance light emission during the electron de-excitation, and diminish light self-absorption [11].

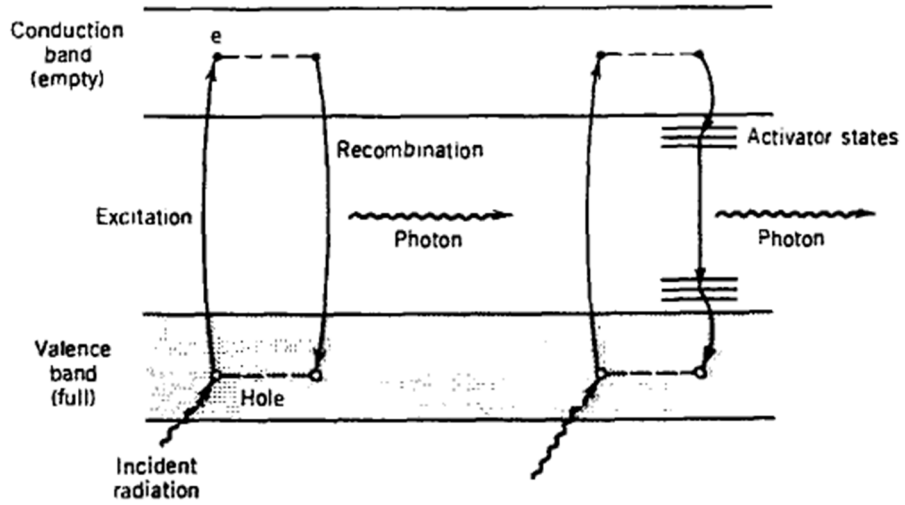

FIGURE 2.8: Energy levels of a scintillator; *Left:* Pure crystal; *Right:* Activated crystal. [11]

The scintillation materials for PET detectors have to meet several requirements. These requirements include short attenuation length 511 keV gamma rays (thus high density and large atomic number), probability of photoelectric absorption as high as possible (large atomic number), high scintillation light yield and absence of self-absorption (affects energy and position resolution of the detector), fast decay time for efficient discrimination of random coincidences, and index of refraction appropriate for coupling with PMTs.

The early PET systems utilized NaI(Tl) crystals, which have a high scintillation light output. Its attenuation length, however, is too long for 511 keV photons, and the photofraction is low. Later, BGO crystals have been introduced. They have a much shorter attenuation length and higher photofraction, but a lower scintillation light output. Following BGO emerged the LSO, and GSO scintillators, both exhibiting a rapid scintillation decay time when in comparison to the earlier crystals, and a good compromise between light output and attenuation length. Even though LSO has a higher light output than GSO, the energy resolution of GSO is better than that of LSO. At the same time emerged BaF_2 crystals, with a very fast scintillation decay time, these are mainly used in time-of-flight (TOF) scanners, which are rarely used commercially in the present days [1] [2] [10] [14] [16]. Table 2.1 describes scintillation materials used in PET.

TABLE 2.1: Characteristics of common PET scintillators. [8] [12] [13] [16] [25] [27] [33] [34] [52] [53] [54]

Characteristic	NaI(Tl)	BGO ($Bi_4Ge_3O_{12}$)	LSO, LYSO	GSO (Gd_2SiO_5: Ce)	BaF_2	$LaBr_3$(Ce)	LXe (liquid xenon)
Effective atomic number	50	74	66	59	52	46.7	54
Density (g/cm^3)	3.7	7.1	7.4	6.7	4.9	5.3	3.06
Scintillation decay time (ns)	230	300	40	60	0.6	~25	27/45* (30%/70%)
Energy resolution at 511 keV (%)	6.6	20	10	8.5	11.4	3.6	10
Relative light output	100	15	75	25	5	175	90/30**
Refractive index	1.85	2.15	1.82	1.85	1.54	—	1.6
Linear attenuation coefficient, μ (cm^{-1})	0.35	0.96	0.87	0.7	0.44	0.47	0.29
Photoelectric fraction (%)	17	40	32	25	17	13	21

* 45 ns corresponds to the recombination component which is suppressed under electric field $E \gtrsim 1\ kV/cm$.
** under electric field $E \gtrsim 1\ kV/cm$.

2.2.1.2 Photomultiplier tube

After scintillation occurs, the emitted light photons are captured and converted to electrical pulses by the photomultiplier tubes. These are composed by a vacuum glass tube that encapsulates a photocathode in one end, an anode in the other end, and dynodes in the middle. A high voltage is applied between the photocathode and the anode (~1000V) and there is incremental voltage from dynode to dynode till the anode.

The photocathode is responsible for absorbing the light photons and proportionally emit electrons to the inside of the tube. These electrons then accelerate to the closest dynode with higher voltage. The dynode's material is chosen so that it has a high probability of secondary electron emission, so

that when incoming electrons collide with a dynode, they cause emission of more electrons in this dynode, augmenting the number of accelerating electrons towards the next dynode and so on. Finally, the number of electrons that arrive the anode is much higher than the original number of electrons that left the photocathode, and an electron pulse with high enough amplitude is delivered to the adjunct electronics [11] [16]. A schematic figure of a PMT is present on figure 2.9.

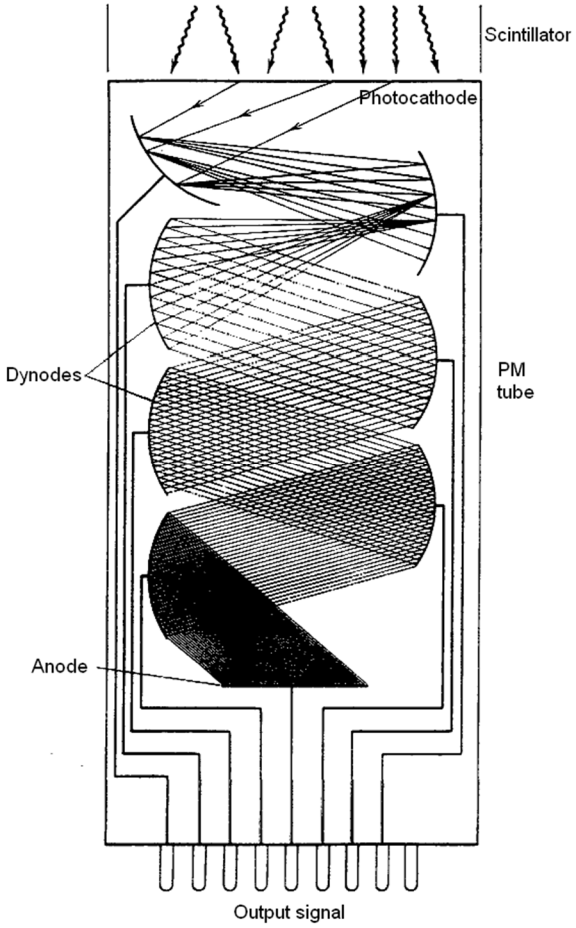

FIGURE 2.9: Schematic of a photomultiplier tube. [11]

2.2.2 Physical factors affecting performance

The deduction of the exact locations of radionuclides inside the body from a PET scan data is conditioned by several factors that affect the final image quality. Such factors include detector and electronics limitations, as well as physical limitations imposed by the propagation of positrons in the human tissue, the annihilation process, and the interaction of gamma rays with the patient's body and the detectors.

2.2.2.1 Detected events

In traditional PET systems, events are accepted when they are within an energy window whose width can vary, for instance 511±70 keV, and within a coincidence timing window. When only one event or more than two in the same coincidence timing window are recorded these are discarded. Nonetheless, some unwanted events are still accepted as valid data:

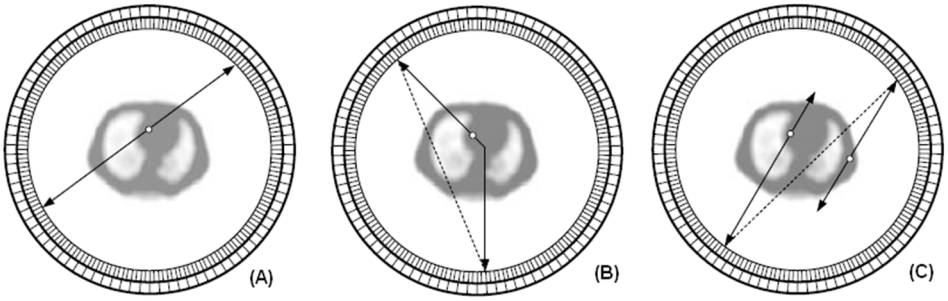

FIGURE 2.10: Types of coincidence events recorded by a PET system; *(a)* True coincidences; *(b)* Scatter coincidence; *(c)* Random coincidence. [14]

- *Scatter Coincidences* – When one or both the emitted 511 keV photons undergo Compton scattering in the body or in the detector they change directions. If accepted in the energy window of the pulse height analyzer they are considered valid data and contribute to diminish image contrast, and signal to noise ratio (SNR) [14].
- *Random Coincidences* – When two unrelated photons, not originated in the same coincidence, reach the detector in the same coincidence timing window, and the other 511 keV from the annihilations escape the detector, then the two photons are accepted as a coincidence and contribute to decrease the SNR [14][16].

2.2.2.2 Technology limitations

- *Normalization* – Small variations in the PMT gains and the position of the scintillators in the block may affect the detection sensitivity of each block. Given this, the raw data produced is not totally uniform, and normalization of the block detectors is required, by exposing uniformly all the detectors to a 511 keV photon source [16].

- *Dead Time* – The dead time is the time that passes from the photon interaction with the scintillator to the pulse generation in the anode of the PM tube and its amplification by an amplifier. During this period the system cannot process another event, and thus if a second event occurs in this period its signal will not be recorded and information is lost. This problem is reduced with better and faster electronics and scintillators with short scintillation decay time [16].
- *Parallax error* – The parallax error, also called radial elongation, is due to photon interactions in the deeper part of the scintillator, resulting in the misplacement of the off center LORs, as explained in figure 2.11, and blurring the final image [16].

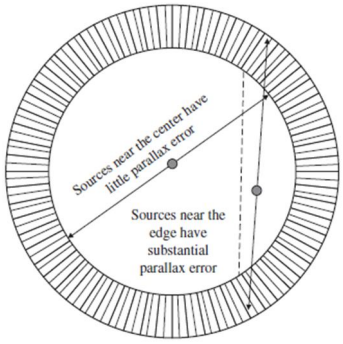

FIGURE 2.11: Parallax error, LOR is allocated to the surface of the opposing detectors (dashed line), and does not pass in the site where the annihilation really occurred. [24]

- *Detector size* – The intrinsic resolution of the scintillator is related to the size of each of the detector crystals elements, for instance, for a PET detector constituted by block detectors of 8x8 BGO crystal matrixes, being each element of the matrixes of 6x6 mm, then the intrinsic resolution varies from 3 mm at the center of the field of view, to 6 mm at the limit of the field of view. As such, the intrinsic spatial resolution is also related to the detector matrix's elements sizes [16].
- *Image reconstruction parameters* – The fact that PET data is stored in sinogram and image matrixes means that this data has to be sampled into fixed sized bins, and thus pixel size limits the image resolution. Besides this, the reconstruction filter and algorithm also have an effect on the image resolution.

2.2.2.3 Photon and positron physics limitations

- *Non-colinearity* – The positron, at the time of the annihilation, may still be carrying some residual kinetic energy from the emission, and consequently the momentum is not zero. Thus, the emitted photons may not be exactly 180º apart, but instead 180º ± 0.25º, causing slight deviations in the LORs and degrading the spatial resolution [16] [2].
- *Positron range* – PET scans aim to obtain the distribution of the radiopharmaceuticals in the body, through procuring to obtain the locations of annihilation events. However, knowing that the emitted positrons still travel for some distance before the annihilation, then the spatial resolution of the radiopharmaceutical distribution is at best as good as the maximum positron range of the used radionuclide [16] [26].
- *Photon attenuation* – Before reaching the detector, the photons have to cross up to ~20 cm of tissue. The more tissue a photon has to cross the higher the probability that it will undergo scattering or be absorbed by the tissue, thus exiting the body deviated from the origin point or not exiting at all. Therefore, photon attenuation in the tissue results in a larger number of detected coincidences from the object surface than in its core. This effect can be taken into account with proper attenuation correction described in Section2.3.3.

2.2.3 Acquisition Modes

PET scanning systems include two modes of data acquisition, the 2-dimentional (2-D) mode and the 3-dimentional (3-D) mode, as schematized in figure 2.12.

The 2-D PET mode was the first type to become available, and presents a physical collimation in the stationary rings of detectors. This collimation consists of fixed or retractable thin annular septa, usually composed by tungsten or lead, placed between the detector rings. The septa serve, first of all to select pairs of photons perpendicular to the ring axis, and secondly to help reduce the scattered and random events count. The acquisition (and reconstruction) is, as such, done in slices (2-D). Despite reducing the effect of scattered events, from ~40% without septa to ~15% with septa, this acquisition mode also reduces significantly the system sensitivity [9] [14] [16].

Later on, in the early 1990s [2], the 3-D PET mode was introduced, presenting retracted or inexistent septa, which allows for a great improvement in the scanner's sensitivity, about a factor of ~6 in comparison to the 2-D acquisition mode [2]. On the other hand, the absence of septa leads to more scattered and random events being detected, hence a worse spatial resolution, and requires more complex reconstruction algorithms, more processing power, and more computer memory [9] [14] [16]. Nevertheless, the 3-D mode is now the dominant modality in PET systems.

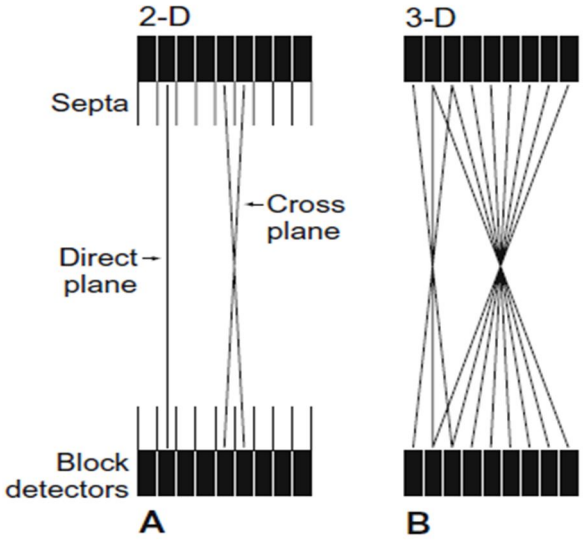

FIGURE 2.12: PET acquisition modes; *(A)* 2-D data acquisition; *(B)* 3-D data acquisition. [16]

2.3 Image reconstruction

PET images are reconstructed using the LORs data resulting from coincidence events. The input LORs must comply with the coincidence criterion, which states that the two photons assumed to be from the same coincidence must be detected within the same very short coincidence time window. Additionally they must also be within an energy window that allows the elimination of some scattered events, and finally the resulting LORs must be within a valid angle in the tomograph [14].

2.3.1 Sinogram

The image reconstruction starts with the storage of the LORs in a (r, φ) matrix called sinogram. The *r* is the distance of the LOR from the ring

center. The angle formed between the x-axis and the same LOR is stored as "φ". This LOR is then assigned to the cross point of the "r" and "φ" values [16], as shown in figure 2.13.

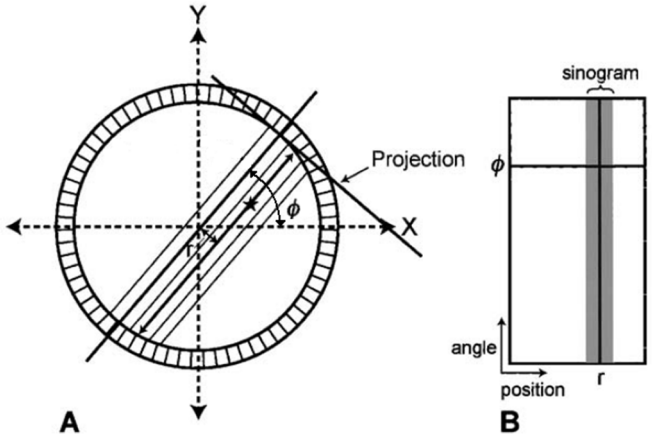

FIGURE 2.13: *(A)* Example of a LOR plotted in (r,φ) coordinates; *(B)* Example of a sinogram. [16]

Therefore, a sinogram is a 2-D histogram representation of all LORs in in the (r, φ) coordinates.

2.3.2 Image Reconstruction

The image reconstruction from sinogram data can be performed in various ways:

- *Simple backprojection* – Consists of constructing a pixel matrix of defined size, for instance of 128x128 pixels. The pixels in the image matrix are in Cartesian coordinates and the sinogram is in polar coordinates. The value that each image pixel attains is given by equation 2.6, being p(r, φ) the count density in the sinogram element and N the number of angle projections, so for any given image pixel (x,y) one sums over all sinogram angles φ with *r* as defined by equation 2.5.

$$r = x.\sin(\varphi) + y.\cos(\varphi) \quad (2.5)$$

$$A(x,y) = \frac{1}{N}\sum_{N=1}^{N} p(r,\varphi) \quad (2.6)$$

Besides this approach, simple backprojection may also consist in projecting back along each LOR line, and add each backprojection to the previous one already formed. When all LORs are considered an image is formed [16].

- *Filtered backprojection (FBP)* – The previous image reconstruction method causes "star pattern" artifacts in the image, resulting in a degraded and blurred image. This effect can be reduced by applying a filter in the acquisition data, through the Fourier method. This method affirms that the line integral $p(r, \varphi)$ in the sinogram relates to the $A(x, y)$ count density distribution in the image by the Fourier transformation. According to this method a Fourier transformation from spatial domain to frequency domain is applied to each row of the sinogram, followed by the multiplication of a frequency domain filter ("ramp" filter) to the sinogram data. At last, the filtered sinogram is obtained by applying the inverse Fourier transformation, and the final image is retrieved by simple backprojection [16].

- *Iterative reconstruction* - In the iterative reconstruction an initial image estimate is performed. Subsequently, projections from the image are computed (forward projection) and compared to the original acquired projections in the sinogram. If the differences between the original acquired projections and the computed projections are significant, then a new image estimate is done, and new projections are computed. Iterations like the previous one are done until the two sets of projections are identical, meaning that the final iteration gives an accurate enough image. The actual computing power has enabled iterative reconstruction methods to be widely used in clinical practice nowadays, such as the "Maximum-likelihood expectation maximization" (MLEM) method and the "ordered-subset expectation maximization" (OSEM) algorithm [16].

- *3-D Reconstruction* – The previous methods can be applied to 3-D data. However, since a 3-D scanning provides a very large volume of data, iterative methods of reconstruction are sometimes not applied on account of taking more time and power to process. Generally 3-D reconstruction comprises the rebinning of the 3-D sinogram into

various 2-D sinograms. Rebinning is accomplished by allocating the LORs that traverse various planes to the plane that comprises the LORs axial midpoints. This method is called the single slice rebinning algorithm (SSRB), and is analogous to acquiring data in a 2-D multiring scanner. Another approach to 3-D reconstruction is the Fourier rebinning algorithm (FORE), which consists of applying the frequency domain Fourier method to each oblique sinogram. After applying either the SSRB or the FORE method, the 2-D obtained sinograms are used to reconstruct images through the filtered backprojection or through the iterative reconstruction [16].

2.3.3 Corrections

Some resolution degrading factors cannot be corrected, such as the positron range for example, yet others can be improved either with better technology, or by applying correction algorithms directly upon the raw data:

- *Photon attenuation* - If the object in study presents a relatively uniform linear attenuation coefficient (μ) then the photon attenuation can be calculated using the theoretical equation 2.7 in order to get to equation 2.8, i.e., by multiplying each sinogram pixel value (N attenuated counts) by the probability of the photon pair detection in that distance to the tomograph center, "r", in order to obtain the number of non-attenuated photons, N_0. Figure 2.14 helps illustrate the deduction of equation 2.8.

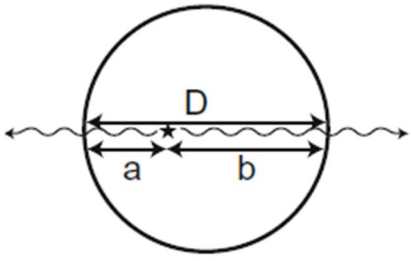

FIGURE 2.14: Photons traversing tissue thickness. [16]

P → Probability of coincidence detection
μ → Linear attenuation coefficient of 511 keV γ-rays
D → Total thickness crossed by photons

$$P = e^{-\mu a} \times e^{-\mu b} = e^{-\mu(a+b)} = e^{-\mu D} \quad (2.7)$$

$$N_0 = Ne^{\mu D} \quad (2.8)$$

However, for objects that present areas with different linear attenuation coefficients, for instance, the human thorax, other attenuation correction methods are used, such as the transmission method. This method utilizes rotating sets of thin rods or point sources of gamma rays with long half-lives, for example ^{68}Ge (a positron source; emits annihilation of γ-rays; $t_{1/2}$=270d) or ^{137}Cs (emits γ-rays with the energy of 662 keV; $t_{1/2}$=30years), and consists of two extra scans, a blank scan and a transmission scan, as in figure 2.15. After the extra scans the attenuation correction factors are obtained for each pixel, by dividing each sinogram's pixel value of the blank scan, I_0, by each sinogram's pixel value of the transmission scan, I, as in equation 2.9 [14] [16]. Afterwards, the obtained attenuation correction factors are multiplied by each of the real scan sinogram pixel. Notwithstanding, this correction is not without disadvantages, it contributes to more noise in the signal, and takes about 40% of a total scan duration [2].

$$\frac{I_0}{I} = e^{\mu D}, for\ each\ pixel \quad (2.9)$$

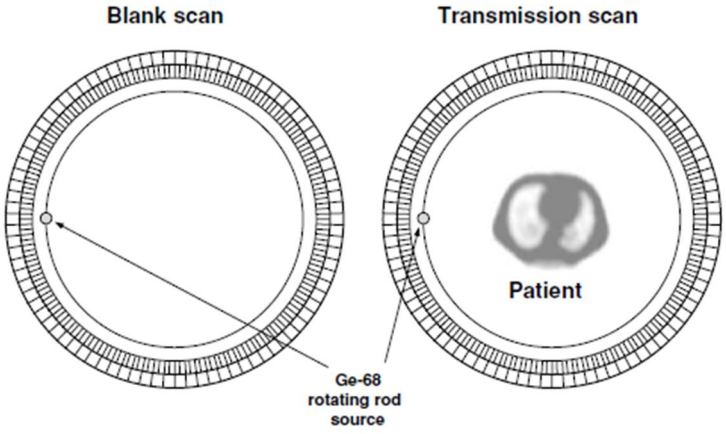

FIGURE 2.15: Transmission method of attenuation correction. Blank scan without patient, and transmission scan with patient without tracer administration. [14]

Besides the transmission method, in PET/CT scanners a CT-based attenuation correction method is used. Since most PET systems is clinical practice are multimodal PET/CT systems, the CT-based

attenuation correction is the most commonly used nowadays. This method takes significantly less time than the transmission method, about 1 minute for the CT-based correction and about 20 to 40 minutes for the transmission method. Firstly a blank (without the patient) CT scan is performed, and the information obtained is stored for the same day's scans. Afterwards, the CT scan in each patient is performed, and the attenuation correction factors are obtained as in equation 2.9 [16].

- *Scatter correction* – In 2-D scans the contribution of Compton scattering in the body is small and is in most cases ignored. In 3-D scans however, the fraction of detected events with Compton scattering is high, and correction is necessary. One way of correcting Compton scattering involves fitting an analytical function to the edges outside the traced object in the profile count and thus deduce the scatter fraction. Another way consists in measuring the differences in counts when the collimator septa are in-place and when they are retracted. Furthermore, Compton scattering can also be corrected utilizing multiple energy window techniques, convolution and deconvolution modeling methods of the scatter distribution, and finally Monte Carlo simulation methods, which can provide theoretical information on the scatter distribution [14].

- *Random coincidences* – The rate of random events per detector pair (R_{ij}) can be obtained by measuring the rate of single events on each detector (C_i, C_j) for a predefined coincidence time window (τ), according to equation 2.10. Another method for estimating the randoms rate, and currently the most commonly used, is the delayed channel method. In this method timing signals from one channel are delayed by a time much greater than the coincidence timing window. This delay implicates that no true coincidences are detected in the delayed coincidence channel, and so any detected coincidences are random. Finally, the random correction is complete when the estimated random events rate is subtracted to the accepted events between each detector pair [14] [16] [71].

$$R_{ij} = 2\tau . C_i C_j \qquad (2.10)$$

2.4 Radionuclides and radiopharmaceuticals

A radioisotope is an unstable isotope that suffers radioactive decay in order to mutate to a more stable form. Most radioactive isotopes are artificially produced, but some are found in nature, such as ^{238}U, ^{235}U, and ^{232}Th. However, natural radioactive nuclei are not suitable for clinical uses, as they only suffer α and β^- decay, not β^+, present too long half-lives, and do not have proper chemical properties for pharmaceutical labeling [10]. Given this, all radionuclides used for nuclear medicine imaging are artificially produced.

2.4.1 Radionuclides production

Among all possible artificially produced radionuclides, PET technology only makes use of a small percentage of these. The required radioisotopes have to be positron-emitting, and suitable for clinical purposes [16]. The mean through which biomedical radioisotopes are produced is the cyclotron, an accelerator advantageous for the considered energy range, and relatively small size [13].

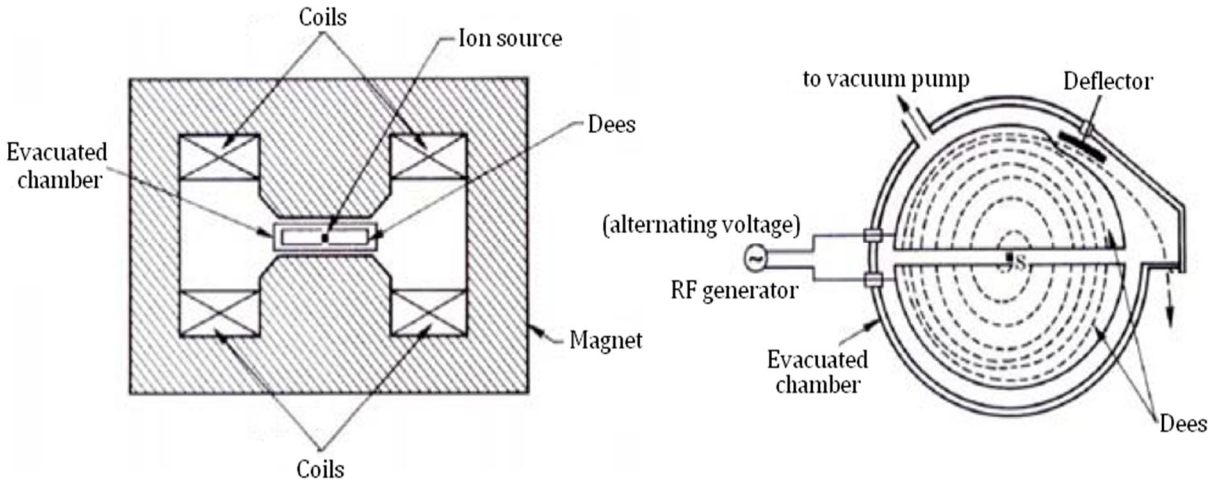

FIGURE 2.16: Simplified schematic of a cyclotron;
left: vertical cross section, *right:* top view. [15]

Inside a cyclotron the trajectory of the particles from the ion source are bent by a magnetic field along a spiral trajectory within two half-cylindrical D-shaped electrodes, called *dees*. The radiofrequency generator

creates a voltage between the two electrodes, and the charged particles accelerate when passing in the gap between the electrodes. After several gap crossings and gradually enlarging orbit, the charged particles increasingly gain kinetic energy [15]. The cyclotrons used for PET radioisotopes production, accelerate protons or deuterons. A schematic diagram of a cyclotron is illustrated in figure 2.16.

2.4.2 Common PET radioisotopes

Nowadays, the most commonly used radionuclides in PET are Nitrogen-13, Carbon-11, Oxygen-15, and Fluorine-18 [18], which are chemical elements that are consumed, or constitute living tissues of the body, and therefore are easily integrated in biologically significant compounds. Table 2.2 lists their attributes. Among these ^{18}F is considered the most adequate radionuclide for commercial PET usages, as it presents a relatively higher half-life [2].

TABLE 2.2: Most common PET radioisotopes. [16]

Isotope	Half-life ($t_{1/2}$)	Mode of decay (%)	Common production method	$E_{\beta+,max}$ (MeV)	Average range of emitted positron in water (mm)
$^{11}_{6}C$	20.4 min	β^+ (100)	$^{10}B(d,n)^{11}C$ $^{14}N(p,\alpha)^{11}C$	0.97	0.85
$^{13}_{7}N$	10 min	β^+ (100)	$^{12}C(d,n)^{13}N$ $^{16}O(p,\alpha)^{13}N$ $^{13}C(p,n)^{13}N$	1.2	1.15
$^{15}_{8}O$	2 min	β^+ (100)	$^{14}N(d,n)^{15}O$ $^{15}N(p,n)^{15}O$	1.74	1.8
$^{18}_{9}F$	110 min	β^+ (97)	$^{18}O(p,n)^{18}F$	0.64	0.46

Besides being biologically significant, PET radioisotopes also have to present a lifetime that is adequate for the time consumed from the radiopharmaceutical production, dose injection and absorption in the body, to the final scan. Moreover, it is of great importance that these radionuclides emit positrons with a low maximum energy, less than a few MeV, so that the

range of the positron is short and thus the annihilation event is very close to the actual location of the radiopharmaceutical.

2.4.3 Radiopharmaceuticals

A radiopharmaceutical is a compound that arises from the opportune combination of a molecule that is capable of following metabolic pathways, integrating or interacting with tissues, cells, or specific chemical substances inside the body *in vivo*, and a labeling radionuclide that is able to integrate or bond to the previous molecule without altering its functional manner. A good radiopharmaceutical is characterized by an effective accumulation and fixation in target cells, absence of accumulation in non-target cells, fast clearance from background tissue or blood, and no side effects. Additionally it should also be economically viable, and of simple preparation [10]. Nevertheless, often, at the expense of radiopharmaceutical quality, the overall production is expensive and complex, considering the radionuclide production and the chemical synthesis that bonds the two substances.

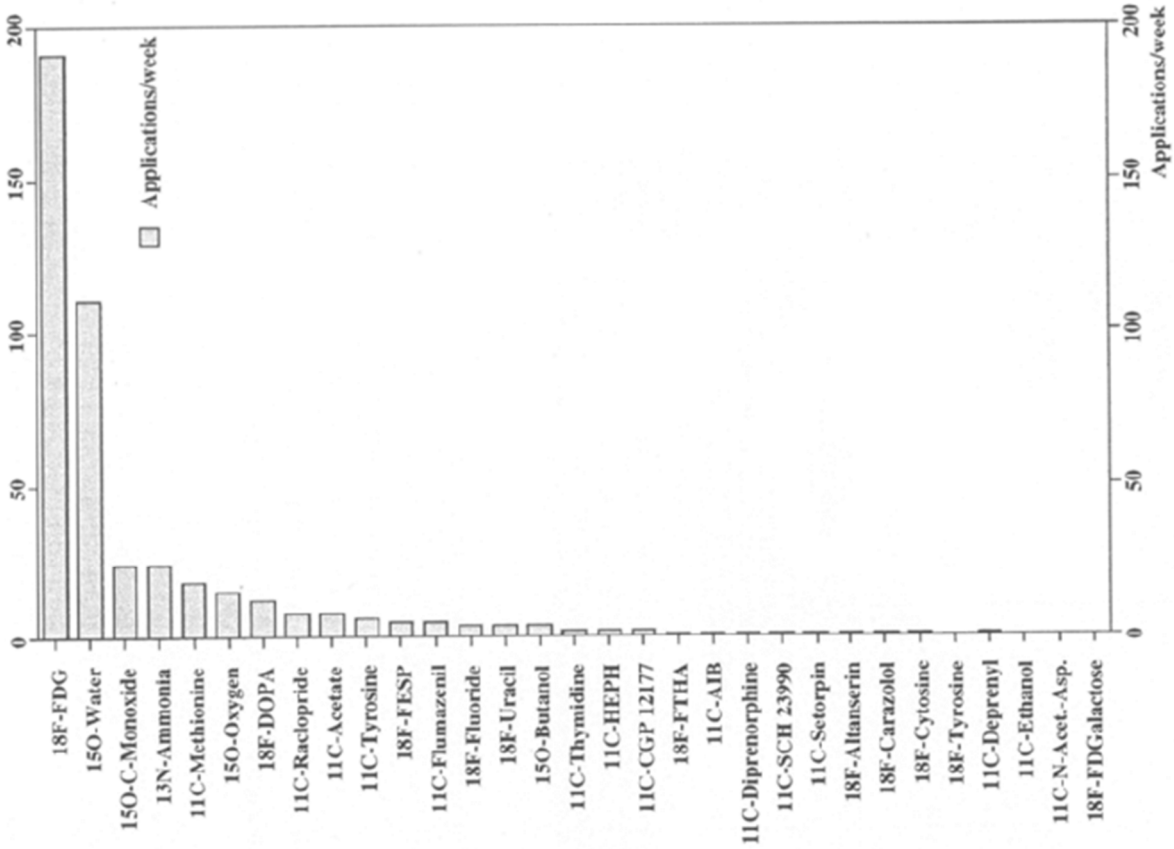

FIGURE 2.17: Frequency of applications of PET tracers in Europe. [21]

Presently, 2-[^{18}F]fluoro-2-deoxyglucose (FDG), a radiopharmaceutical used for studying regional glucose metabolism, is by far the most widely used RP in PET, not only in Europe as figure 2.17 illustrates but also worldwide. Additionally, [^{15}O]water, [^{15}O]carbonmonoxide, [^{13}N]ammonia, [^{11}C]-L-methionine, and L-6-[^{18}F]fluoro-DOPA also count among the most important ones [20] [21]. Table 2.3 describes the imaging application and synthesis method of some of the most common PET radiopharmaceuticals.

TABLE 2.3: Most common PET radiopharmaceuticals. [21] [1] [16] [20] [23]

Radiopharmaceutical	Synthesis method	Imaging application
2-[^{18}F]fluoro-2-deoxyglucose (FDG) ($C_8H_{11}{}^{18}FO_5$)	Electrophilic substitution with ^{18}F-fluorine gas or Nucleophilic displacement with ^{18}F-fluoride ions.	Regional glucose metabolism for oncology, neurology, and cardiology
[^{15}O]water ($H_2{}^{15}O$)	Cyclotron irradiated gas is transferred to water generator	Blood flow and perfusion studies in oncology, neurology, and cardiology
[^{15}O]carbonmonoxide ($C^{15}O$)	Target gas with [^{15}O] is heated at 1000ºC with carbon, and purified passing through charcoal-soda lime column	Cerebral blood volume
[^{13}N]ammonia ($^{13}NH_3$)	Reduction of ^{13}N-labeled nitrates and nitrites produced by proton irradiation in acyclotron of water	Myocardial and cerebral perfusion
[^{11}C]-L-methionine	Reaction between ^{11}C-CO_2 precursor and carbanion,followed by hydrolysis with an acid. Alkylation of the sulfide anion of Lhomocysteine with ^{11}C-iodomethane.	Aminoacids transport and protein synthesis for oncologic studies
L-6-[^{18}F]fluoro-DOPA	Fluorodemetallation using electrophilic fluorinating agents	Presynaptic dopaminergic function in the brain

2.5 Latest developments and future trends

The benefits for medical investigation and diagnosis brought by the introduction of PET scans in clinical practice have caused a great impact on the medical imaging field. Nonetheless, there is still plenty of room for improvements in PET technology.

As already mentioned in the introduction, the greatest tendency of commercial uses for PET systems nowadays always includes coupling with an anatomic imaging system, such as CT or MRI, as there is great medical advantages for diagnosis in acquiring superimposed anatomic and functional images. Functional PET/CT multimodal systems were achieved and put to commercial use about a decade ago relatively without major difficulties. PET/MRI systems have presented a challenge for imaging scanner producers due to the fact that most PET systems utilize photomultipliers as photodetectors, and these are sensitive to magnetic fields [13].

In order to surpass the magnetic field interference for PET/MRI coupling, and other limitations, some alternatives to the traditional PMTs have been considered, such as position sensitive multianode PMTs (PS-PMT), metal channel dynode PMTs, hybrid PMTs, micro-channel plate PMTs (MCP-PMT), visible light photon counters (VLPC), avalanche photodiodes (APDs), Geiger-mode avalanche photodiodes (G-APDs), and charge-coupled devices (CCDs). Among these, avalanche photodiodes have gained special attention because of their cost effectiveness, small size, good time resolution, and insensitivity to magnetic fields [13] [32] [48]. Silicon photomultipliers (SiPMs), also called Multi-pixel photon counters (MPPCs), are examples of PET employing G-APDs [49] [50].

The PET tomograph design is heading towards two major advancements that will possibly be part of the standard commercial PET scans in the future. The time-of-flight (TOF) PET scans and the detectors with depth of interaction (DOI) for parallax error correction [29].

A TOF-PET system is based in accurately measuring the arrival time differences between two coincidence photons. This enables the deduction of the location of the annihilation site along the line of response, and 3-dimensional images can be directly retrieved. In order to achieve a sub-centimeter position resolution, the time resolution of the detectors must be of less than 50 ps. As this resolution is not yet possible, the deduced location of the annihilation site is restricted to a segment line of a few centimeters. The advantage of this PET configuration is the reduction of statistical noise [42] [43] [44] [45] [46]. Figure 2.18 explains the reconstruction mode of TOF-PETs.

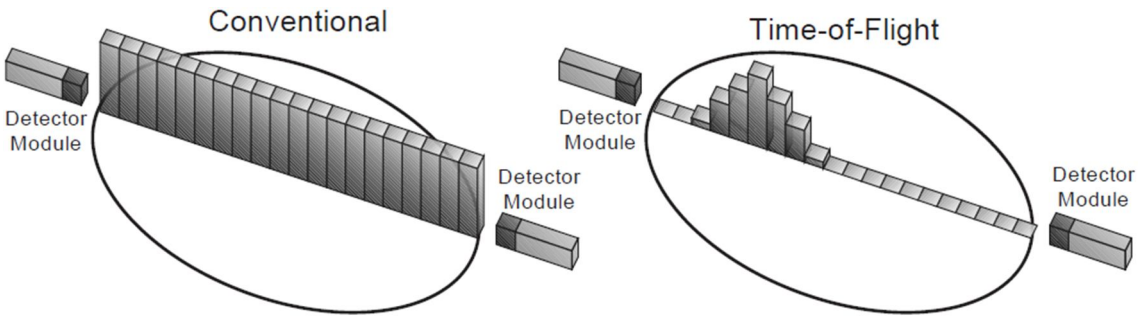

FIGURE 2.18: *Left:* Conventional reconstruction, where all pixels along a LOR are incremented in the same amount; *Right:* TOF reconstruction, each pixel along a LOR is incremented according to the probability of the annihilation having occurred in that pixel. [42]

DOI measurements can be done in various ways, including PET systems equipped with multi-layer detectors, DOI direct measurements, single ended readouts, or duel-ended detectors. The two main methods are the multi-layer detectors, and the dual-ended detectors. The multi-layer design is constituted by various arrays of scintillation crystals and obtains discrete measurements. In this design, the depth of interaction is given by determining in which crystal layer the event occurred, either through the pulse shape discrimination method (PSD, also known as the phoswich method in which the scintillators have different decay constants), through the relative offset structure, or through the light sharing method [47], as illustrated in figure 2.19.

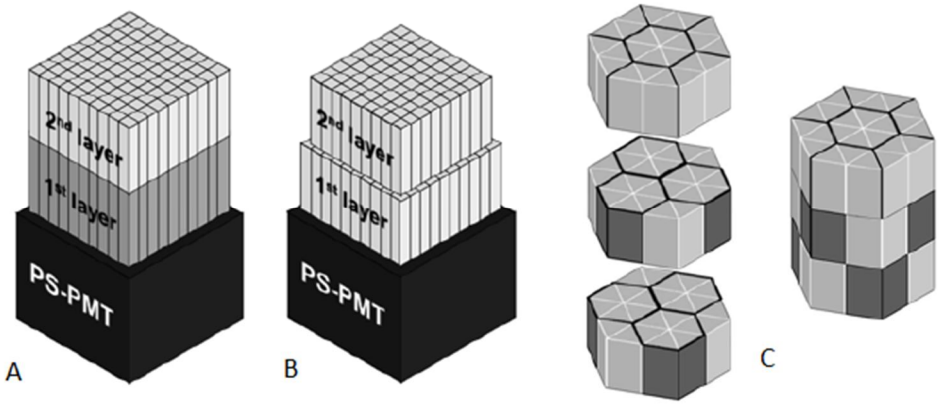

FIGURE 2.19: Multi-layer DOI detectors; *(A)* Pulse shape discrimination method (PSD); *(B)* Relative offset structure; *(C)* Light sharing method. [47]

In dual-ended detector modules, two arrays of photosensors are attached to both the scintillator crystal ends. The depth of interaction is then deduced

by comparison of the detected light outputs of each array of photodetectors. The photosensors utilized for this module are various position sensing APDs, SiPM or WLS fibers [47].

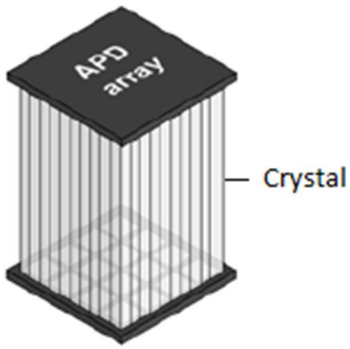

FIGURE 2.20: Dual-ended detector module. [47]

Despite considerably improving the spatial resolution of PET, the DOI designs highly increase the manufacturing cost, due to the presence of more crystals, photosensors, and more complex electronics. This has been the main drawback for commercial implementation of these systems [47].

Besides tomograph designs and multimodal systems, new PET scintillators and electronics that have a better energy, spatial and time resolution are always procured for obvious reasons. The state of the art scintillator in modern commercial PET scans is the LSO, or LYSO crystals, however future generations of PET scintillators are likely to incorporate the Lanthanum scintillator [34] $LaBr_3$ since it shows adequate properties for regular PET and TOF-PET detectors [51] stated in table 2.1. There have also been proposed modules in which the detector is a rare gas liquid, such as the liquid Xenon (LXe) emphasized in this paper. One example of a proposed module for LXe PET is the Multiwire ionization chamber filled with liquid xenon, for more details read Ref. [70]. The advantages of LXe in comparison to the more popular solid inorganic scintillators are that it is capable of using both scintillation and ionization signals for event position and energy detection, it is also a low cost compact detector capable of depth of interaction and a high count rate, along with a good spatial, energy and timing resolution. Moreover, with Compton reconstruction the scatter and random noise can be diminished [27]. It is in this context that the present project gains relevance.

Furthermore, PET technology has also been applied for specific applications, for instance in high resolution small animal scanners used

mainly in animal research [16], and the Positron Emission Mammography (PEM) that has recently been introduced and shows great potential in clinical practice. This system is able to co-register positron emission metabolic information with the mammography information [35], in order to provide breast cancer information efficiently, with a higher spatial resolution and at lower price than a PET scan [30] [31] [40]. PEM's major advantages reside in the fact that the scanning quality is not affected by breast density, or hormonal induced changes, and it considerably reduces the number of false positives for breast cancer when in comparison to MRI or traditional mammography, thus reducing the number of unnecessary biopsies [36] [37].

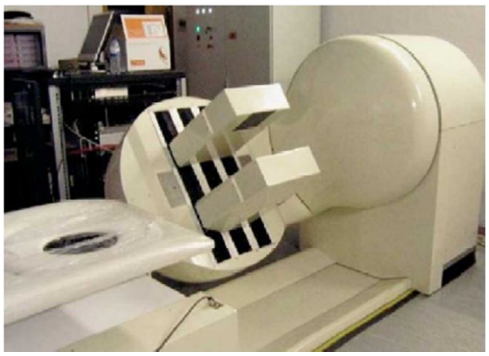

FIGURE 2.21: Clear PEM Sonic machine installed at ICNAS, Coimbra, Portugal. [39]

Moreover, the continuous development of computer systems, producing increasingly faster processors and higher storage capacity drives with smaller dimensions, permits constant advances on reconstruction methods for PET images and artifact corrective algorithms. For instance, algorithms for correction of patient motion artifacts, and gating the registered activity in order to offset for cardiac and respiratory movements are becoming more and more popular [10] [40] [41].

Concerning radiopharmaceutical development, the latest trends in researches show an increasing interest in imaging brain beta amyloid for neurologic disease studies, such as Alzheimer disease, by injecting tracers with high affinity for β-amyloid agglomerates, and high brain entrance [28]. ^{18}F-NaF has also demonstrated good potential for clinical use in detecting bone metastases, by identifying irregular osteogenic activity, and the vesicular monoamine transporter type II has been emphasized for studying the passage of neurotransmitters. Additionally, clinical tracers that study the

myocardial perfusion are given importance due to earlier diagnosis of ischemic heart disease, [^{15}O]Water, [^{13}N]Ammonia, and Flurpiridaz F-18, are examples of RPs used in myocardial blood flow studies. Furthermore, for oncologic studies, amino-acid analogs traced with ^{18}F and ^{11}C, such as [^{18}F]FACBC and [^{11}C]L-methionine, have been developed to work as amino-acid transport tracers, providing information on tumor growth, as it involves an augment in protein synthesis. Finally, angiogenesis, DNA synthesis, gene delivery and expression for studies with gene therapy, and tumor antigen expression have also been under study [20].

Chapter 3

Photon interaction with matter

Photons are electromagnetic radiation that have zero rest mass, zero charge, and travel at the speed of light *c* [55]. When a photon enters an absorbing medium it can escape without alterations, or interact either with the medium's atoms orbital electrons or with the atomic nuclei. Consequently, if interactions occur, photons can either disappear, by transferring all their energy to light charged particles, or be scattered, with or without partial energy transfer to light charged particles [15]. The four main processes through which gamma rays interact with matter are the photoelectric effect, the electron-positron pair production, the coherent scattering called Rayleigh and Thomson scattering, and the incoherent scattering called Compton scattering [56]. However, photoelectric effect and Compton scattering are described in more detail in this paper, since PET photons are of 511 keV energy, which is too low for pair-production, but too high for Rayleigh scattering.

3.1 Photoelectric effect

The photoelectric effect arises from the interaction of the incident photon and a tightly bound orbital electron. This occurs when the photon energy, *hv*, is higher than the orbital electron's binding energy, E_B. The photon is completely absorbed by the orbital electron, which is then emitted with kinetic energy, E_K, given by equation 3.1, and illustrated in figure 3.1 [15] [25].

$$E_K = hv - E_B \quad , \qquad \begin{matrix} h - Plack's\ constant \\ v - photon\ frequency \end{matrix} \tag{3.1}$$

The conservation of momentum and energy dictates that the photon cannot transfer all its energy to a free electron, and thus this effect is restricted to tightly bound electrons, so that the respective atom absorbs the excess of momentum. The resulting ejected electron becomes a free electron called photoelectron [15].

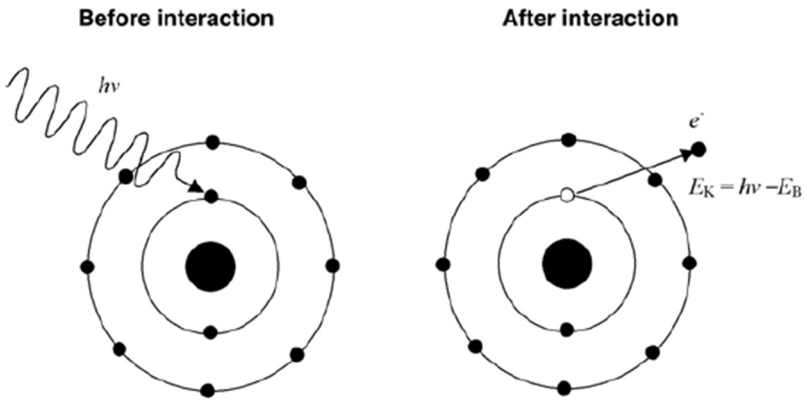

FIGURE 3.1: Scheme of a photoelectric effect example. [15]

When the photoelectron is emitted, a free vacancy is left in the respective shell. This vacancy is then occupied by a higher shell electron, and the differential energy of this transition can be emitted in the form of a characteristic photon, or in the form of an Auger electron [15].

The binding energies of orbital electrons depend on the atomic number (Z) of the atom, and the electron shell where they are located. These energies decrease towards outer shells. When the incident photon energy exceeds the binding energy of the absorbing atom's K-shell, around 80% of the photoelectric effects in this case occur with the K-shell electrons [25].

The probability of occurrence of photoelectric effect can be expressed in terms of photoelectric cross section, τ [55]. This probability depends on the photon energy, and the atomic number of the material. The characteristic curve of the photoelectric cross section as a function of the incident photon energy presents sudden discontinuity peaks, called absorption edges, that occur when the photon energy is close to the electron shells binding energies, as demonstrated by figure 3.6 [15].

There are three energy regions for the photoelectric cross sections, the first region immediately close to the absorption edges, the second region somewhat far from the K absorption edge, and the region far from the K absorption edge, called the relativistic region ($\varepsilon>>1$). For the middle energy

region, that includes 511 keV, the atomic cross section for photoelectric effect for K-shell electron can be written as in equation 3.2 [15].

$$_{a}\,\tau_K = \alpha^4 Z^n \frac{8\pi}{3} r_e^2 \sqrt{\frac{32}{\varepsilon^7}} \qquad (3.2)$$

$$where \;\; \alpha = \frac{1}{137} is\ the\ fine\ structure\ constant$$

$$r_e = 2.818\ fm \;\; is\ the\ classical\ radius\ of\ the\ electron$$

$$\varepsilon = \frac{hv}{m_e c^2} \;\; is\ the\ normalized\ photon\ energy$$

$$Z\ is\ the\ atomic\ number\ of\ the\ absorber$$

$$n \;\; ranges\ from\ 4\ at\ lower\ energies\ to\ 4.6\ at\ higher\ energies$$

For low energy photons, the emitted photoelectrons tend to have a 90° angle with the incident photon, however as the photon energy increases, the photoelectrons tend to be emitted progressively in a forward direction [15]. Figure 3.2 illustrates the angular distribution of photoelectrons for various incident energies, where it is possible to see that most photoelectrons produced by PET 511 keV photons are in a forward direction.

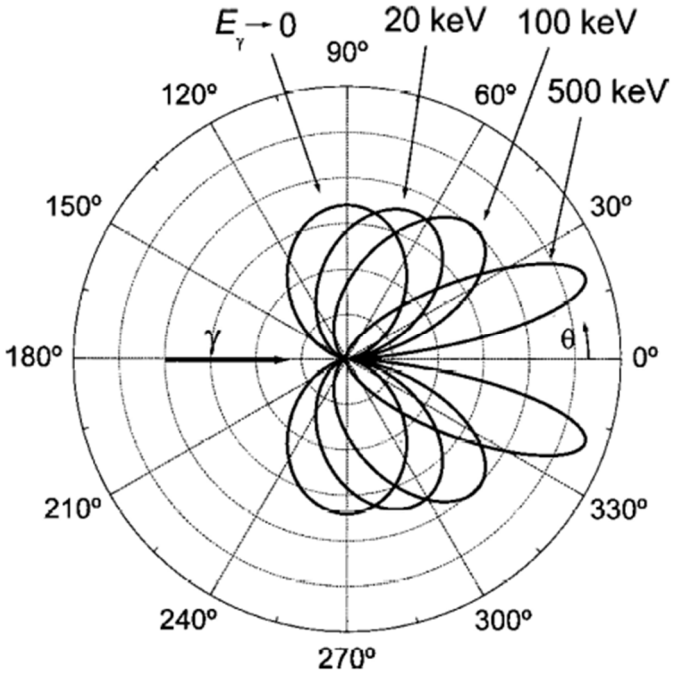

FIGURE 3.2: Angular distribution of photoelectrons for unpolarized photons. [56]

3.2 Compton Scattering

The Compton effect, also named Compton scattering, consists in the interaction between a photon and an orbital electron, usually considered free. The interaction results in the emission of another photon with different momentum and less energy, called scattered photon, and an electron with kinetic energy, E_K, called the Compton electron or recoil electron [15]. This effect can be most easily described on the basis of the corpuscular behavior of photons and it is an incoherent scattering [25]. Figure 3.3 illustrates the Compton effect.

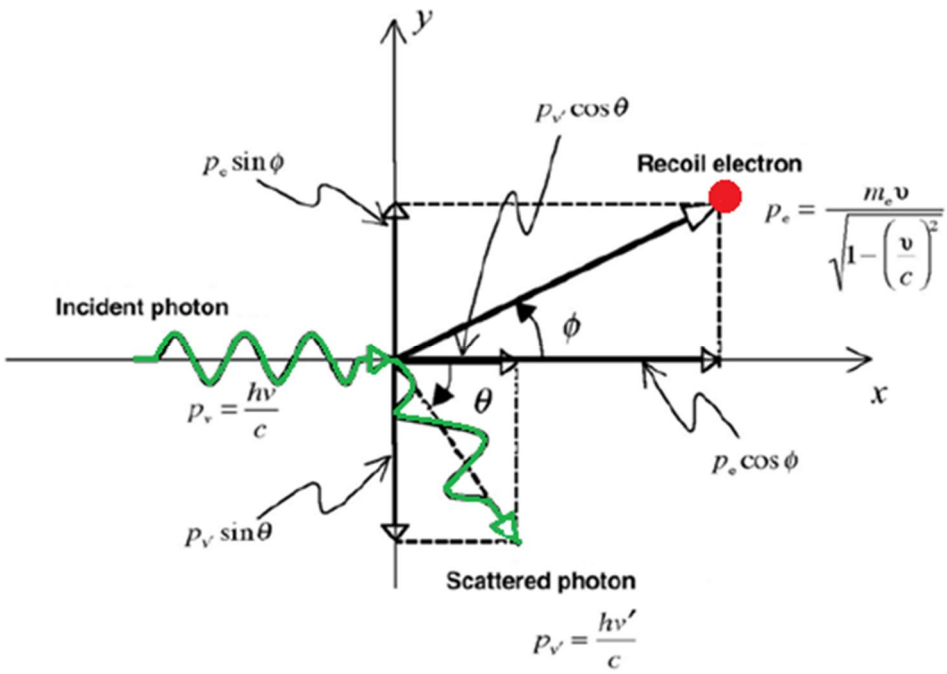

FIGURE 3.3: Scheme of Compton scattering. [15]

The assumption of the corpuscular behavior of photons allows us to use the relativistic law of complete energy and momentum conservation for the Compton effect. Equation 3.3 states the energy conservation equation of this interaction, equation 3.4 states the momentums conservation equation in the x-axis, and equation 3.5 states the momentums conservation equation in the y-axis [15].

$$hv + m_e c^2 = hv' + m_e c^2 + E_K \quad \Leftrightarrow \quad hv = hv' + E_K \tag{3.3}$$

$$p_v = p_{v'} cos\theta + p_e cos\varphi \quad (3.4)$$

$$0 = -p_{v'} sin\theta + p_e sin\varphi \quad (3.5)$$

$hv \rightarrow$ incident photon's energy

$p_v=(hv)/c \rightarrow$ incident photon's momentum

$hv' \rightarrow$ scattered photon's energy

$p_{v'}=(hv')/c \rightarrow$ scattered photon's momentum

$m_e c^2 \rightarrow$ rest energy of the electron

$E_K \rightarrow$ kinetic energy of the emitted electron

$p_e = m_e v/\sqrt{1-(v/c)^2} \rightarrow$ Compton electron's momentum

The above equations along with the relativistic expression $p=mv$, allow obtaining the Compton wavelength shift equation, the scattered photon energy and the recoil electron energy, transcribed in equations 3.6, 3.7 and 3.8 respectively, where λ is the wavelength of the incident photon, λ' is the wavelength of the scattered photon, $\Delta\lambda$ the difference between them, and λ_c the Compton wavelength of electron [15].

$$\Delta\lambda = \lambda' - \lambda = \lambda_c(1 - cos\theta) \quad (3.6)$$

$$hv' = hv\frac{1}{1+\varepsilon(1-cos\theta)} \quad (3.7)$$

$$E_K = hv\frac{\varepsilon(1-cos\theta)}{1+\varepsilon(1-cos\theta)} \quad (3.8)$$

$\varepsilon = hv/m_e c^2$ *normalized incident photon energy*

Figure 3.4 depicts the relationship between the fractional energy of the scattered photons and the scattering angle for a 511keV incident photon (PET photons), when ε is equal to 1. Equation 3.8 allows us to deduce that the larger the scattered photon's angle (θ) the higher the electron's kinetic energy, so the maximum kinetic energy of the Compton electron is achieved when the photon is scattered back ($\theta=180^o$). Moreover, one can also deduce

from this equation that for a given θ angle the higher the incident photon's energy the more energy is transferred to the recoil electron [15] [56].

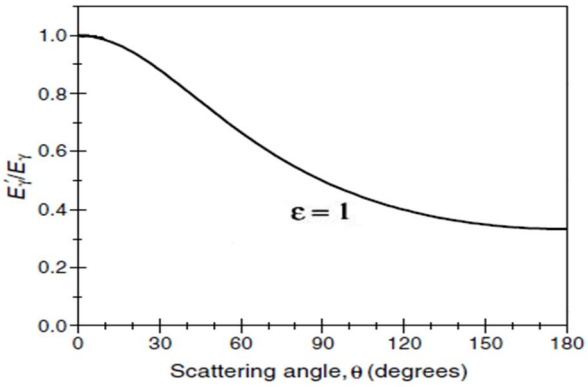

FIGURE 3.4: Scattered photons' fractional energy versus the scattered angle. [56]

The scattered angle, θ, and the recoil electron angle, φ, are related as stated in equation 3.9, which means that with the increase of the scattered photon's angle, the recoil electron's angle decreases [15].

$$\cot\varphi = (1+\varepsilon)\tan(\theta/2) \tag{3.9}$$

The maximum Compton electron angle, φ is of 90º and it is obtained when the scattered photon is in the same direction as the incident photon, θ=0º. When the scattered photon makes 180º with the incident photon, the recoil angle is 0º. Figure 3.5 shows the θ and φ relation for a ε=1.

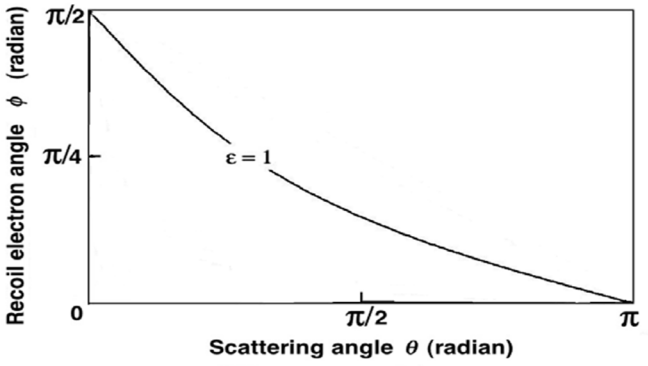

FIGURE 3.5: Recoil angle and scattering angle relation. [15]

Compton cross section equations are complicated functions of the scattering angle and incident photon energy. For information on these equations, not transcribed in this paper, we refer the reader to subchapter

7.3 of reference [15]. Figure 3.6 demonstrates the relationship between the mass attenuation coefficients for Compton scattering and photoelectric effect, and the incident photon's energy for four PET scintillators.

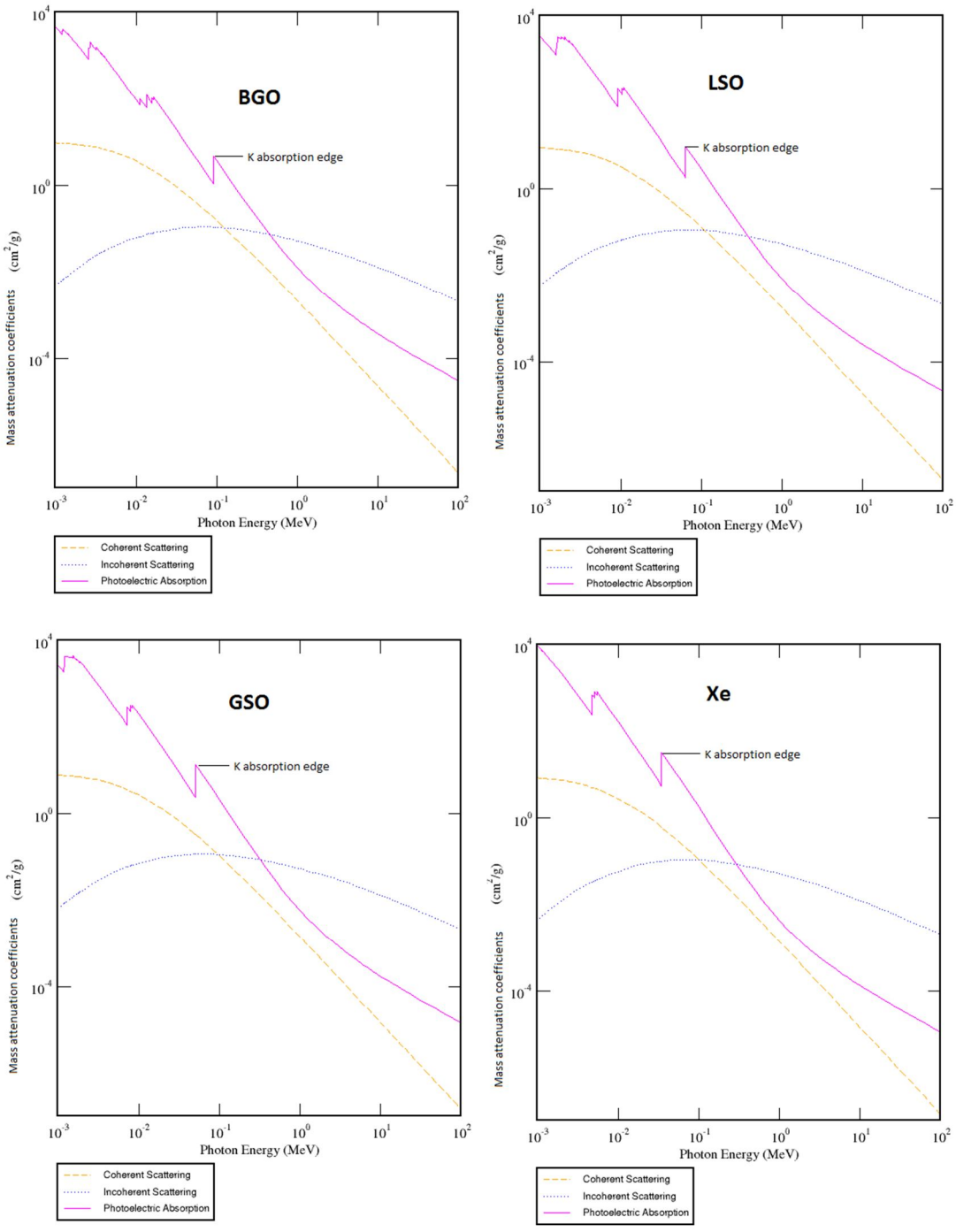

FIGURE 3.6: Mass attenuation coefficients for various PET scintillators versus the incident photon energy. [57]

The differential electronic cross section for Compton effect, also called the differential Klein-Nishina electronic cross section, gives us the

probability for Compton scattering of photon on a free electron, as well as the angular distributions of the scattered photons [55]. Figure 3.7 shows the angular distribution of the scattered Compton photons for various incident photon energies, where it is possible to verify that for a ε=1 value (PET incident photons), the grand majority of the scattered photons continue in a forward trajectory. This fact justifies our choice of Compton tracing algorithms, explained in the next chapter [15] [56].

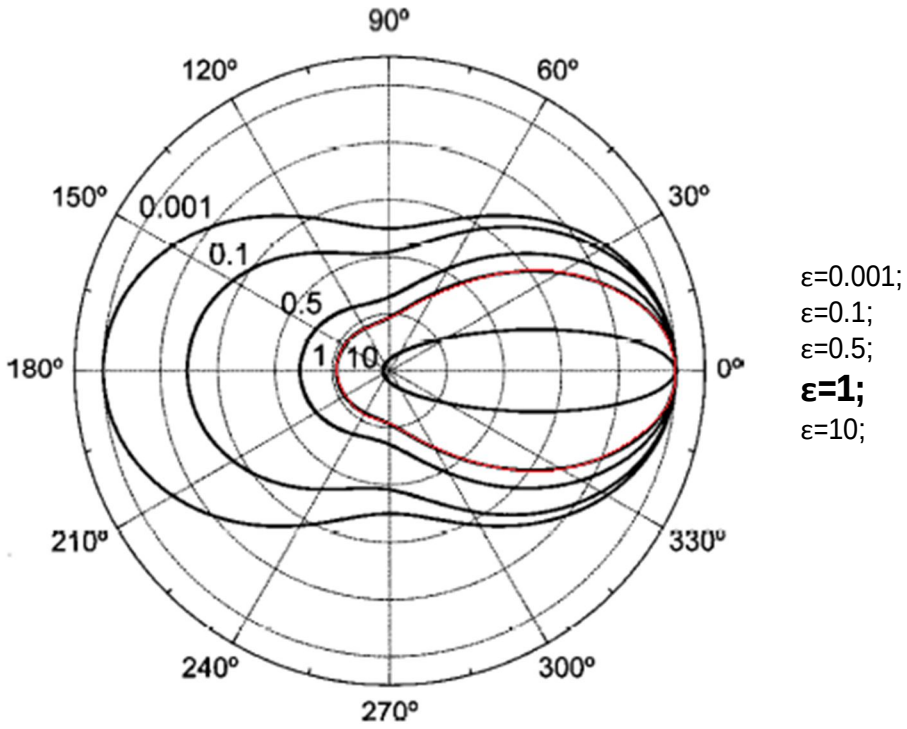

FIGURE 3.7: Angular distribution of Compton scattered photons for various normalized incident photon's energy. [56]

3.3 Rayleigh scattering

Rayleigh scattering is a process, through which incident photons undergo coherent scattering, i.e., the photon's energy practically does not change (elastic scattering) [56]. In the Rayleigh scattering, the entire atom receives the transferred momentum, but it is not ionized or excited, as the electrons return to their original state after the interaction.

The Rayleigh scattering is more probable than Compton scattering at low energies (<100keV). However since the scattering angles are small and

the change in the photon energy is negligible, the Rayleigh scattering does not have significant practical impact on medical imaging with radioisotopes.

Figure 3.6 illustrates the mass attenuation coefficients of various PET scintillators for the coherent scattering in comparison to incoherent scattering and photoelectric effect.

3.4 Pair Production

When the incident photon's energy is higher than 1.022 MeV, which is twice the rest energy of an electron ($m_e c^2$), the production of an electron-positron pair becomes energetically possible. Since this process can only occur if energy, charge and momentum are conserved, a collision partner is required [15], reason why it has to take place in the electromagnetic field of a nucleus or of a bound electron, being the cross section of the second smaller by ~10^3 [56]. Since PET photons have less than 1.022 MeV, pair production in this application is inexistent, reason why it is not considered in PET algorithms. The pair and triplet production by a high energy photon (>1.022 MeV) is illustrated in figure 3.8.

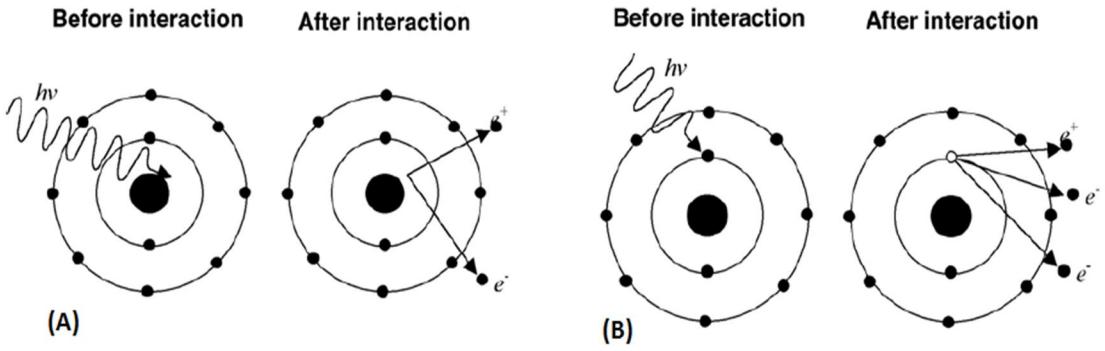

FIGURE 3.8: *(A)* Pair production scheme in the electromagnetic field of a nucleus; *(B)* Triplet production in the electromagnetic field of an orbital electron. [15]

Chapter 4

Methodology

In order to analyze the feasibility of using Compton scattered events in the detector for the image reconstruction, as predicted for the project's aim, we firstly needed to produce simulated data that depicted, in most ways, an object emitting 511 keV pairs of photons, and the detection in a detector ring of the object's incoming radiation. Afterwards, the generated data is processed in order to simulate a real detector's response, and lines of response are obtained according to two Compton tracing algorithms further explained.

4.1 Simulation data with GEANT4

Monte-Carlo methods have become an important tool in medical physics analysis, for instance in dose calculations for radiation therapy, in nuclear medicine imaging, and in X-ray imaging [59]. In this work the GEANT4 simulation toolkit has been chosen, which is, according to reference [58], *"a software toolkit for the simulation of the passage of particles through matter. It is used by a large number of experiments and projects in a variety of application domains, including high energy physics, astrophysics and space science, medical physics and radiation protection"*.

The PET detector geometry and materials, along with the emitted radiation, and the phantoms' activity, materials and dimensions, were programmed in C++ files using the GEANT4 structure.

4.1.1 Detector

The detector was defined to be a cylinder of 40 cm inner radius, 45 cm outer radius, and 20 cm length. Moreover, the cylinder was divided in 36 detector sections, being each section 10º apart from the neighboring blocks. Figure 4.1 illustrates our GEANT4 model of the detector ring.

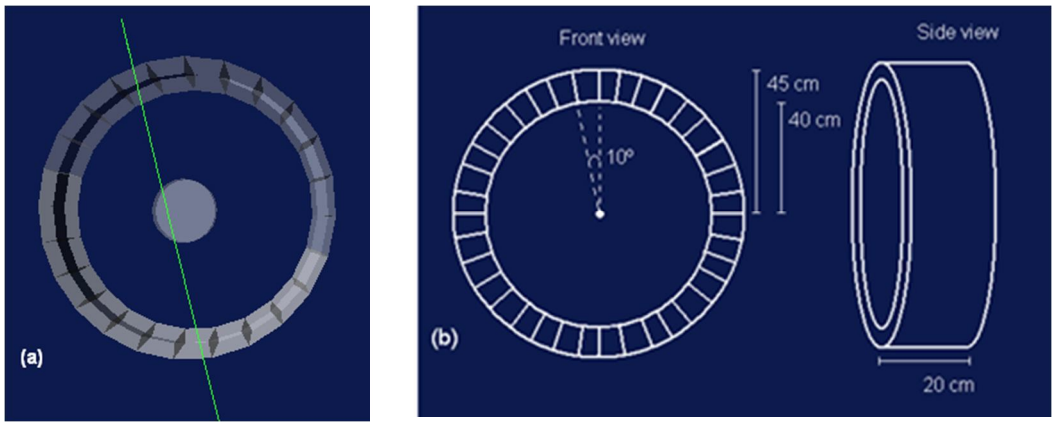

FIGURE 4.1: Simulated detector ring; *(a) 3-D view* (obtained with VRMLview graphical interface); *(b)* Schematic.

The chosen detector material is Xenon, which, as explained in section 2.5, is a possible detector for future generations of PET systems, and requires Compton reconstruction for better performance. The used isotope fractional composition was the isotopic composition of natural Xenon, present in table 4.1.

$_{54}$Xe Isotope	Fraction (%)
^{124}Xe	0.095
^{126}Xe	0.089
^{128}Xe	1.91
^{129}Xe	26.4
^{130}Xe	4.071
^{131}Xe	21.232
^{132}Xe	26.909
^{134}Xe	10.436
^{136}Xe	8.857
Total	131,293 g/mol

TABLE 4.1: Isotope fractional Composition of the simulated Liquid Xenon detector. [60]

The established laboratory (world) volume in which the detector ring is inserted is defined to be a cube, 100 cm in each of the three axis of the Cartesian coordinate system *(x,y,z)*, centered at (0,0,0).

4.1.2 Phantom types

Three phantom types were defined: A phantom similar to the UTAH phantom (phantom 1) in order to access the image contrast, and two other phantoms (phantom 2 and 3) similar to the NEMA scatter fraction phantoms [61] for scatter fraction measurements. All phantoms were simulated to be either filled with water (phantom's material is water), or empty.

Phantom 1:

<u>Dimensions:</u>
Phantom radius = 10 cm;
Phantom centered at (0,0,0);
Insert 1 radius = 2.5 cm;
Insert 1 x-position = -5 cm;
Insert 1 y-position = 0 cm;
Insert 2 radius = 2.5 cm;
Insert 2 x-position = 5 cm;
Insert 2 y-position = 0 cm;
Phantom length = 5 cm;

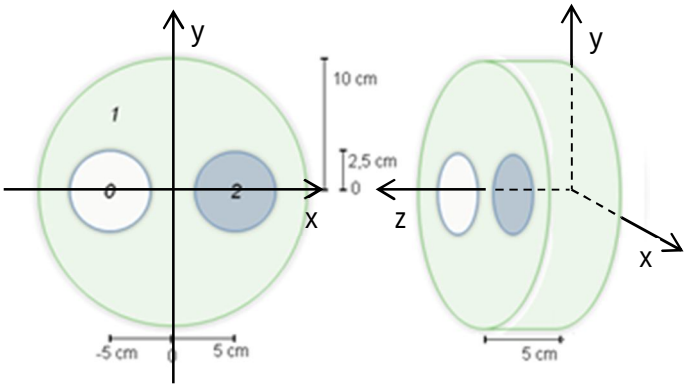

FIGURE 4.2: Schematic of the simulated phantom number 1.

<u>Activity fractions:</u>
Insert 1 = 0;
Insert 2 = 2;
Phantom = 1;

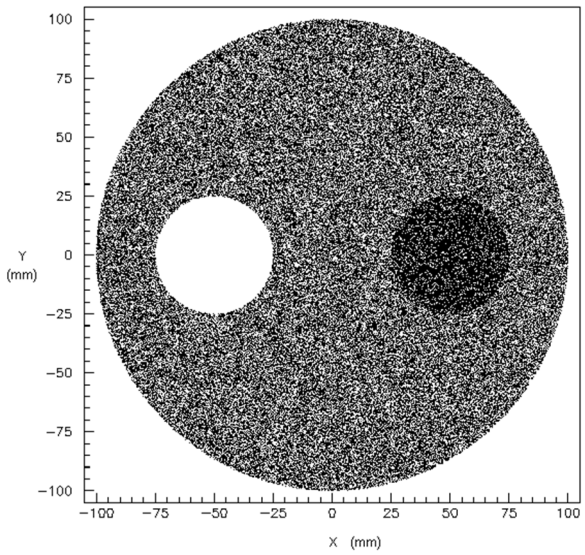

FIGURE 4.3: Simulated activity distribution for phantom 1.

Phantom 2:

Dimensions:
Phantom radius = 10 cm;
Phantom centered at (0,0,0);
Insert radius = 0.16 cm;
Insert x-position = 0 cm;
Insert y-position = 0 cm;
Phantom length = 20 cm;

Activity fractions:
Phantom = 0;
Insert = 2;

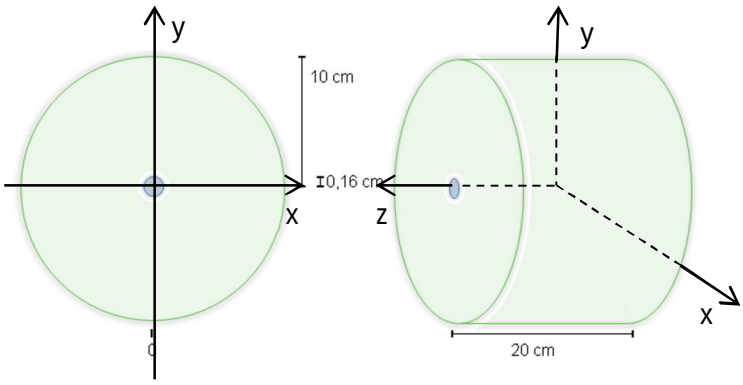

FIGURE 4.4: Schematic of the simulated phantom number 2.

Phantom 3:

Dimensions:
Phantom radius = 10 cm;
Phantom centered at (0,0,0);
Insert radius = 0.16 cm;
Insert x-position = 0 cm;
Insert y-position = 4.5 cm;
Phantom length = 20 cm;

Activity fractions:
Phantom = 0;
Insert = 2;

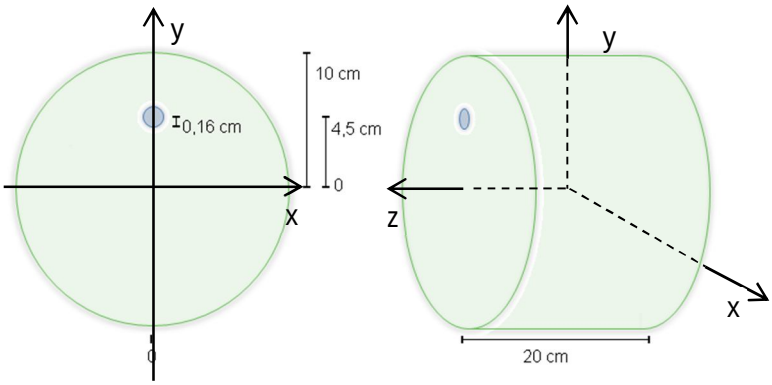

FIGURE 4.5: Schematic of the simulated phantom number 3.

4.1.3 Radiation emission and interaction physics

The collinear pairs of 511 keV photons were generated in randomly chosen directions. All events that occur in the detectors are recorded, both photons and electrons being traced.

This simulation does not include non-colinearity, neither positron range. The concept of time is also not present in this simulation, so there is no consideration on coincidence timing.

The interactions sequences are stored in an ASCII file, for each 511 keV γ-ray separately. For each detector event and for each of the two γ-rays, the following attributes are recorded:

- Type of particle that underwent a physical process (particle index can either be a gamma-ray, an electron, or an X-ray);
- The parent particle of the previous one (parent ID);
- The particle's origin location;
- Type of physical process that the particle suffered. For photons the included processes are Compton scattering and photoelectric effect. The fluorescence X-rays are not followed in the present simulation being the respective energy deposited at their origin. For electrons, the included processes are Bremsstrahlung emission, ionization, and multiple scattering. The ionization is not considered as a continuous process along the path but instead as deposited energy on the stopping site;
- The number of the detector section where the event occurred;
- The event local energy deposition;
- Accumulated energy deposited in the detector.

For water phantom simulations, no limitations on the γ-rays emission angles were imposed as photons can be scattered before reaching the detector. However, for vacuum phantoms simulations, the produced collinear photons emission was limited in θ, as shown in figure 4.6, in order to speed up the simulation. The photons cannot be scattered in vacuum, and thus it is redundant to produce photon pairs that for certain do not reach the detector.

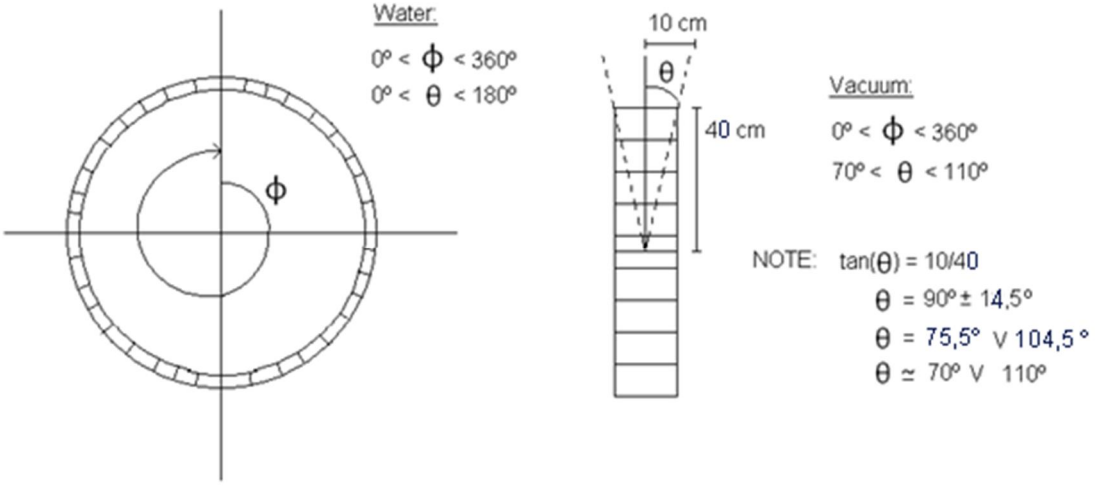

FIGURE 4.6: Angles limitations of the collinear photons emission.

4.2 Simulation of detector response

The obtained data from GEANT4 gives us the exact locations and deposited energies of the events. However in a real detector, the measured position and energy are not exact due to finite detector resolution. In addition, events that occur too close to each other are detected not as separated events but as one.

Given this, we processed the obtained data from GEANT4 in order to take into account the response of the detector, by firstly smearing the coordinate *x, y, z,* and the energy of each event, and secondly by clustering close events. This was done using a specially develop code in C++.

The smearing algorithm is based on the Pólya distribution, exemplified in figure 4.7, also named the negative binomial distribution, which states that the probability density function of a random variable X is given by equation 4.1. The Pólya distribution was considered instead of the Poisson distribution due to the fact that the Poisson distribution is a discrete function, unlike the Pólya distribution with a similar but continuous function that is adequate to our continuous events' coordinates and energies values [62] [63] [64] [65]. Besides this, the Gaussian (normal) distribution was also not implemented as it could result in negative values when smearing low energies.

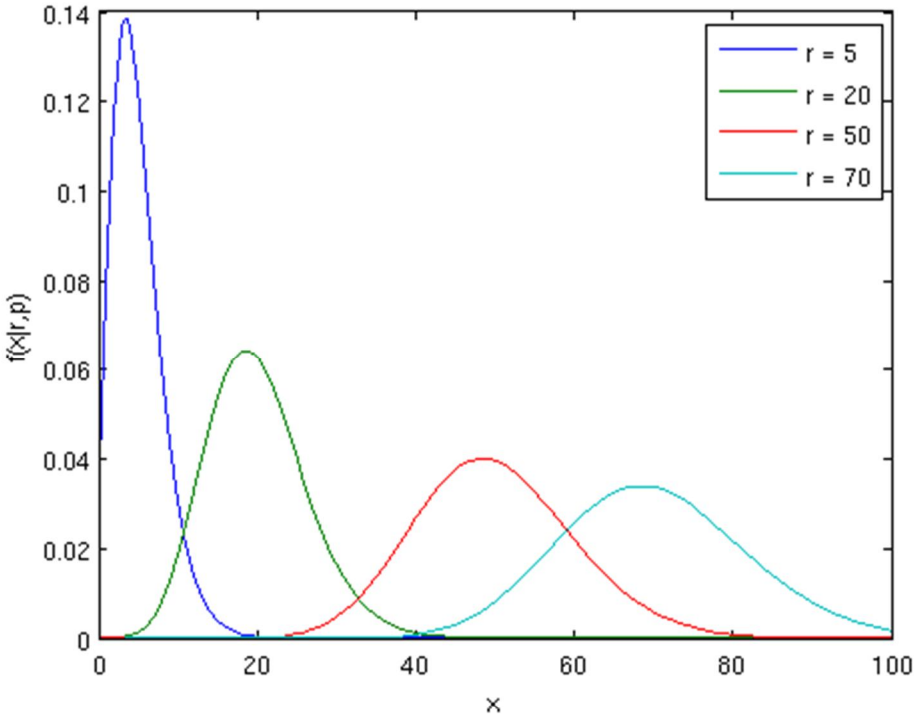

FIGURE 4.7: Negative binomial probability density function for various values of the *r* parameter, for the same parameter *p=0.5* (Matlab). [65]

$$f(x) = \binom{x + r - 1}{r - 1} p^r (1 - p)^x, \quad (4.1)$$

with the following properties:

$Mean$: $\mu = \frac{r}{p} - r$ (4.2)

$Variance$: $\sigma^2 = \frac{r}{p}\left(\frac{1}{p} - 1\right)$ (4.3)

$Standard\ deviation$: $\sigma = \sqrt{\frac{r}{p}\left(\frac{1}{p} - 1\right)}$ (4.4)

$Moment\ generating\ function$: $G(t) = p^r[1 - (1 - p)e^t]^{-r}$ (4.5)

where *r* and *p* are parameters.

A C++ function *polya(μ,σ)* was used with μ being the original coordinates or energy, and σ the respective resolution values as follows.

The resolution is defined by the user for the energy 511 keV at <u>full width at half maximum</u> (FWHM):
Energy resolution =RE511 (%)
X-axis resolution=RX511 (mm)
Y-axis resolution=RY511 (mm)
Z-axis resolution=RZ511 (mm)

From this the respective sigma values are calculated:
$\sigma E511 = (RE511 \times 0.511) / 2.35$ *(MeV)*
$\sigma X511 = (RX511) / 2.35$ *(mm)*
$\sigma Y511 = (RY511) / 2.35$ *(mm)*
$\sigma Z511 = (RZ511) / 2.35$ *(mm)*

Further, for an energy deposit of *E* the resolution is scaled according to the $E^{-1/2}$ law as below:

$$\frac{\sigma_E}{E} \sim E^{-\frac{1}{2}} \ and \ \ \sigma_{x,y,z} \sim E^{-\frac{1}{2}} \ \ which\ result\ in$$

$$\sigma E = \sigma E511\sqrt{E/0.511}$$
$$\sigma X = \sigma X511\sqrt{0.511/E} \quad (4.6)$$
$$\sigma Y = \sigma Y511\sqrt{0.511/E}$$
$$\sigma Z = \sigma Z511\sqrt{0.511/E}$$

The *polya(μ,σ)* function returns new coordinates and energies for each of the detected events.

In this project two sets of detector resolutions were used. The first set is $R1_{E511}$=20%, $R1_{X511}$=2mm, $R1_{Y511}$=2mm, $R1_{Z511}$=2mm, and the second one is $R2_{E511}$=10%, $R2_{X511}$=0.5mm, $R2_{Y511}$=0.5mm, $R2_{Z511}$=0.5mm. The first set approximates the performance of the current PET detectors while the second one corresponds to the expected resolution of the liquid xenon PET detector, which is being developed at TRIUMF [66].

The new coordinates and energies were then used as input for the clustering routine. The algorithm used for clustering consists of successive aggregations of the energy depositions spaced by less than 1 mm, and which were detected in the same detector section, until all resulting "new" events are > 1mm. Below, in equations 4.7, are transcribed the transformation equations used to produce the "new" event coordinates and energy, from two events spaced by less than 1 mm.

$$x_c = \frac{x_1.E_1+x_2.E_2}{E_1+E_2} \quad y_c = \frac{y_1.E_1+y_2.E_2}{E_1+E_2} \quad z_c = \frac{z_1.E_1+z_2.E_2}{E_1+E_2}$$
$$E_c = E_1+E_2 \quad \text{c} - \textit{clustered}, 1 \textit{ and } 2 - \textit{unclustered values} \tag{4.7}$$

Finally, after smearing the original GEANT4 sequence points, and clustering the events, the real detector simulation data files are saved containing the new events positions and energies, as well as information regarding the true original parent γ-ray and the number of the crystal section where they are located. These files maintain the original interaction sequence order, because the clustering algorithm starts clustering from the first event, checking if other points will be clustered to it, and moving on to the next unclustered event, checking if other points will be clustered to it, and so on.

A schematic of the whole real detector simulation process is presented in figure 4.8.

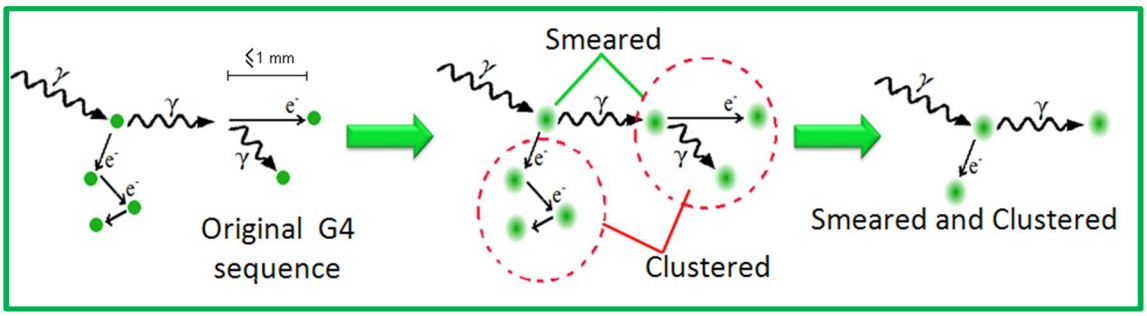

FIGURE 4.8: Scheme of the real detector simulation process.

4.3 LOR retrieval and Compton tracing algorithms

Both the GEANT4 original data files, and the real detectors simulation data files are used as input data for the lines of response retrieval, so that comparisons can be made between the processed data and the control data (GEANT4 files). This part of the project was also programmed in C++.

4.3.1 Parent gamma ray allocation

Contrary to a Monte Carlo simulation, in a real detector it is not known to which of the two γ-rays belong a detected interaction. Therefore, an algorithm was implemented that decides, among all the events of each sequence, which are originated from γ-ray 1 and which are originated from γ-ray 2. This algorithm takes into account the positions of all detected interactions, and computes the angles between them, having the ring axis as a reference, for the final purpose of separating two groups of events, according to the following steps:

1. If only one event is recorded, sequence is discarded.
2. Limiting angle is chosen (α_{lim}), in this work $\alpha_{lim}=45^{o}$.
3. Distances between all events are computed (R_{events}).
4. The shortest distance of R_{events} is found ($R_{Shortest}$).
5. Angle between events 1 and 2 correspondent to $R_{Shortest}$ is calculated (α_{12}).
6. If $\alpha_{12} \leq \alpha_{lim}$, and there are more events besides event 1 and 2, then event 1 and 2 attributed to γ-ray 1, and we proceed to step 7, else the sequence is discarded. If $\alpha_{12} > \alpha_{lim}$ and the sequence only has two

events, then event 1 is attributed to γ-ray 1 and event 2 is attributed to γ-ray 2. If $\alpha_{12} > \alpha_{lim}$ and the sequence has more than two events, the sequence is discarded.

7. Events within α_{lim} to the left and to the right of event 1 and 2 are attributed to γ-ray 1 as well, as illustrated in figure 4.9.
8. If only one event is left, then this event is attributed to γ-ray 2. Else we proceed to step 9.
9. Distances between the rest of the events are computed ($R2_{events}$).
10. The shortest of all $R2_{events}$ is found ($R2_{Shortest}$).
11. Angle between events 3 and 4 correspondent to $R2_{Shortest}$ is calculated ($\alpha 2_{12}$).
12. If $\alpha 2_{12} \leq \alpha_{lim}$, event 3 and 4 are attributed to γ-ray 2. If $\alpha 2_{12} > \alpha_{lim}$ the sequence is discarded.
13. Events within α_{lim} to the left and to the right of event 3 and 4 are attributed to γ-ray 2 as well, as illustrated in figure 4.9.
14. If there are no more events left, the process is complete. If there are events that were not allocated to γ-ray 1 or γ-ray 2, then the whole sequence is discarded.

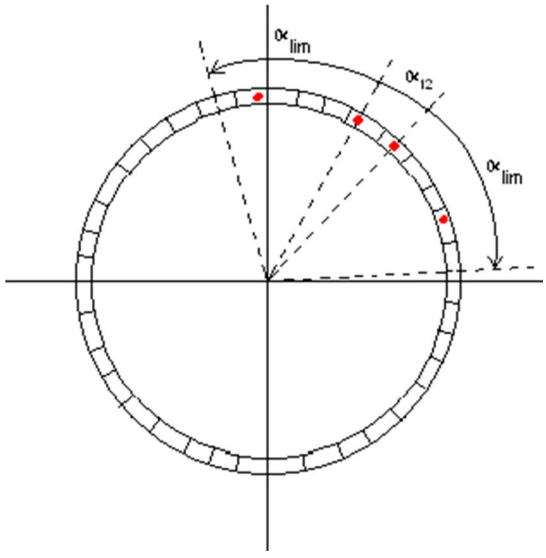

FIGURE 4.9: γ-ray division.

4.3.2 Compton tracing methods

After establishing two groups of events within a sequence (γ-ray 1 group and γ-ray 2 group) two algorithms for Compton tracing are applied in order to choose, for each group, which interaction is going to be used to define the respective LOR, as exemplified in figure 4.10.

The closest to the center algorithm:

For each group, the distances to the centre of the tomograph (0,0,0) are calculated, and the interaction location that corresponds to the shortest distance is accepted for LOR reconstruction. This algorithm is based on the fact that the grand majority of the scattered photons that result from Compton scattering of 511 keV incident photons, are emitted in a forward direction, as explained in subchapter 3.2, and illustrated in figure 3.7.

The shortest LOR algorithm:

The distances between each interaction point of one group, to each of the interaction points of the other group are calculated, i.e., all possible LORs are computed. The shortest LOR is assumed to be the true one.

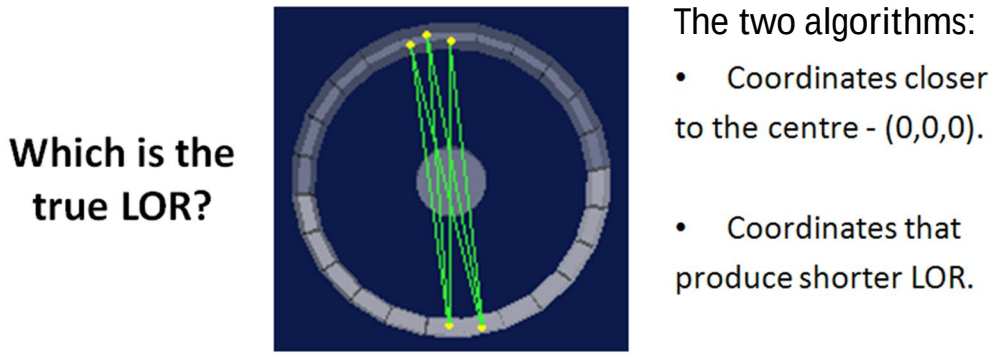

FIGURE 4.10: Choosing the correct LOR.

4.3.3 LOR data files

A number of files are generated as a result the application of the above algorithms to the real detector data. For the sake of comparison, a set

of files containing LORs determined from the exact GEANT4 data, has also been produced.

From the GEANT4 original data files the following LOR files were generated:

- Golden Standard – LORs defined by the true first interactions for each of the two gamma-rays.
- Golden standard 350-650keV - LORs defined by the true first interactions, if the true first interactions correspond to a sequence where the sum of all deposited energies in the detector per gamma-ray is within the energy window [350 keV; 650 keV].
- Known gamma closest to the center – Using the original γ-rays sequence to separate the events due to γ_1 and γ_2, LORs are chosen through the closest to the center algorithm.
- Known gamma shortest LOR - Using the known γ-ray interaction sequences to separate the events due to γ_1 and γ_2, LORs are chosen through the shortest LOR algorithm.
- Unknown gamma closest to the center – Using the parent gamma ray allocation algorithm to separate the events due to γ_1 and γ_2, i.e., as if not knowing the event true parent γ-ray, LORs are chosen through the closest to the center algorithm.
- Unknown gamma shortest LOR – Using the parent gamma ray allocation algorithm to separate the events due to γ_1 and γ_2, LORs are chosen through the shortest LOR algorithm.

From the real detector simulation files, the one with $R1_{E511}$=20%, $R1_{X511}$=2mm, $R1_{Y511}$=2mm, $R1_{Z511}$=2mm, and the one with $R2_{E511}$=10%, $R2_{X511}$=0.5mm, $R2_{Y511}$=0.5mm, $R2_{Z511}$=0.5mm, the following LOR files were obtained:

- Golden standard – Since these files maintain the original true sequence order, and have information regarding the true original parent γ-ray, it is possible to retrieve the first event, with altered (i.e., smeared and clustered) coordinates and energies, of each original γ-ray.

- Golden standard 350-650keV – First events that correspond to sequences where the sum of all event energies of each γ-ray are within the [350 keV;650 keV] energy window.
- Golden standard with γ-ray allocation algorithm – Dividing the events in two groups by the γ-ray allocation algorithm and retrieving for each group the first event to have occurred.
- Traditional PET – Events with only one measured interaction for each γ-ray. Both interactions must be within the [350 keV; 650 keV] energy window to be accepted.
- Unknown gamma closest to the center – Using the parent gamma ray allocation algorithm to separate the events due to γ_1 and γ_2, LORs are chosen through the closest to the center algorithm.
- Unknown gamma shortest LOR– Using the parent gamma ray allocation algorithm to separate the events due to γ_1 and γ_2, LORs are chosen through the shortest LOR algorithm.
- Unknown gamma closest to the center 350-650keV – Using the parent gamma ray allocation algorithm to separate the events due to γ_1 and γ_2, LORs are chosen through the closest to the to center algorithm. The events are only accepted if they correspond to sequences where the sum of all energy depositions for each γ-ray are within the [350 keV; 650 keV] energy window.
- Unknown gamma shortest LOR 350-650keV – Using the parent gamma ray allocation algorithm to separate the events, LORs are chosen through the shortest LOR algorithm. The events are only accepted if they correspond to sequences where the sum of all energy depositions for each γ-ray are within the [350 keV; 650 keV] energy window.

4.4 Image reconstruction

The files produced as explained above, and containing, for each accepted gamma ray pair, the coordinates of the two points chosen to define the LOR as well as the total measured energy, serve as input for the image

reconstruction. This part of the project was performed in MATLAB®, a high level programming language and interactive environment [7].

4.4.1 Image reconstruction

The image reconstruction procedure consisted in the following steps:

1. The 3-D acquired data is rebinned into equivalent sets of 2-D projections, according to the Single Slice Rebinning algorithm (SSRB), explained in subchapter 2.3.2.
2. For that, a set of transaxial slices was defined along the detector length, in our case we divided the 3-D data in 5 slices, of 4 cm each (20cm/5 = 4 cm). Then the midpoint in the *z-axis* of each LOR is calculated ($z_{med}=(z_1+z_2)/2$), and the LOR is allocated to the slice that incorporates the calculated z_{med}.
3. For each slice, a 2-D sinogram is generated as explained in section 3.2.1. The angles between the LOR and the *x-axis* are also calculated, φ. The *r* variable is histogrammed into a predefined number of bins (nr_{bins}) by dividing the tomograph diameter by the bin size desired, and the φ variable is also histogrammed into a predefined number of bins ($n\varphi_{bins}$) by dividing π rad by the desired angle bin size. Finally for each (r,φ) a unit is incremented to the respective cell each time a LOR presents those (r,φ) coordinates and thus a 2-D histogram is created for each slice.
4. Finally, for each of the 2-D sinogram, the filtered backprojection method is applied to obtain the reconstructed images. In this project, the FBP was done using the Inverse Radon transform of the sinograms, with a linear interpolation, and the ramp type of filter (Ram-Lak filter).

4.4.2 Attenuation correction

No attenuation correction was applied to the empty phantoms as there is no photon attenuation in vacuum. However for water filled phantoms attenuation correction is required for quantifiable image information.

Since the phantom is filled with the same material, the linear attenuation coefficient, μ, is uniform throughout the whole phantom. Hence,

the applied correction method utilizes an altered version of equation 2.8, equation 4.8, which inputs the sinogram data pixel values and *r* position.

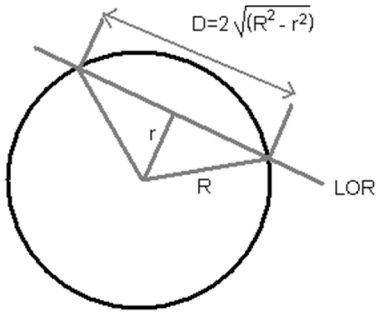

$$N_0 = N e^{D \times \mu\_water(511kev)_{linear}} \quad (4.8)$$

where
N_0 → new sinogram pixel value
N → original sinogram pixel value
$R_{phantom}$ → phantom radius
$\mu\_water(511kev)_{linear}$ = 9,598 x 10^{-2} cm^{-1} → linear attenuation coefficient of water for 511 keV photons [67]

With equation 4.8 a new sinogram is obtained, which is then used for reconstruction of the corrected image.

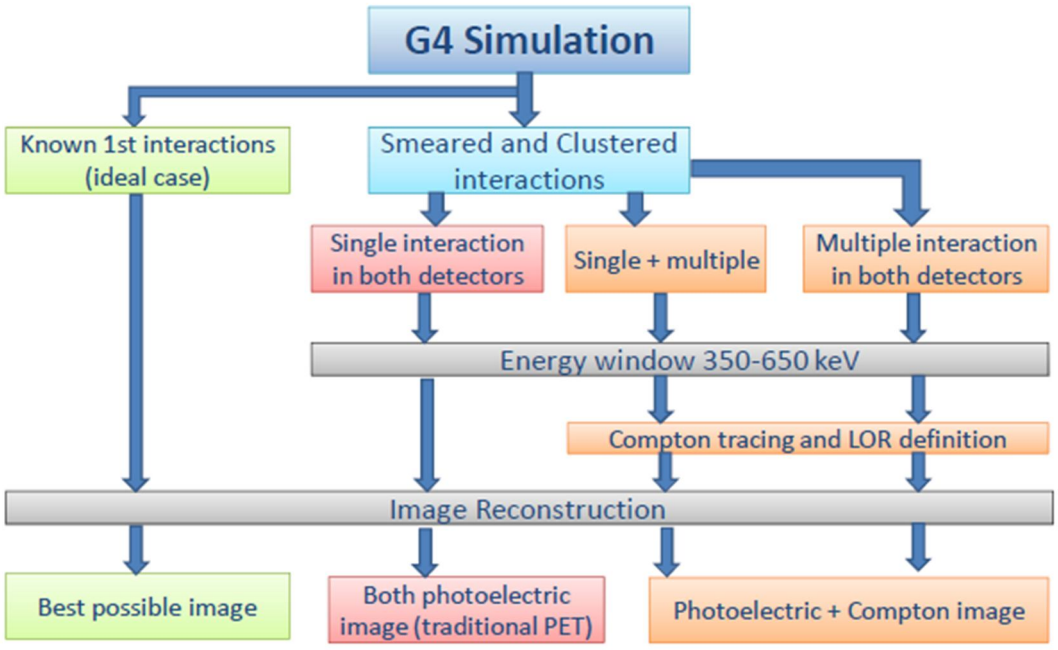

FIGURE 4.11: Classification of the events and their processing.

4.5 Analysis

We used three methods for quantitative comparison of the acquired data. Two of them allow comparing the obtained images and evaluate the effect of the LOR retrieval algorithms. One of them uses image contrast while the other is based on a scatter fraction estimate, as described in section 4.5.1. The third method is previous to image reconstruction. It makes use of the knowledge of the true interaction sequence (from the simulation) to validate the gamma assignment and Compton tracing algorithms (see section 4.5.2.

4.5.1 Image analysis

We used two parameters that allow us to quantitatively compare and analyze image differences: the image contrast, and the scatter fraction. The image contrast was used for comparison of the phantom number 1 images (UTAH-like phantom), and the scatter fraction was used for comparison of the phantoms 3 and 4 images (NEMA-like scatter fraction phantoms).

Image contrast:

Three equally sized areas (same number of pixels) from regions of interest in each of the UTAH-like phantom's images were retrieved, as figure 4.12 illustrates. The pixel counts from each of the three areas were then summed, and the ratios between them obtained.

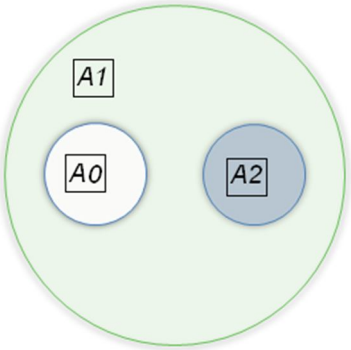

$$C_{01} = \frac{A0}{A1}$$

$$C_{02} = \frac{A0}{A2}$$

$$C_{21} = \frac{A2}{A1}$$

FIGURE 4.12: Definition of the image contrast parameters (C_{01}, C_{02}, C_{12}).

Scatter Fraction:

For each of the NEMA-like Scatter Fraction phantom sinograms, a profile count along the *r-axis* is made. Then four areas of the profile count are defined, as illustrated in figure 4.13 (a). The scatter fraction is retrieved through dividing the counts that correspond to the scatter area by the total counts, equation 4.9. For visual comparison of different reconstruction methods, profile normalization was also used as shown is Fig. 4.13(b). The normalization of the peaks is done by diving each profile bin value by the bin with the maximum count value of the same profile.

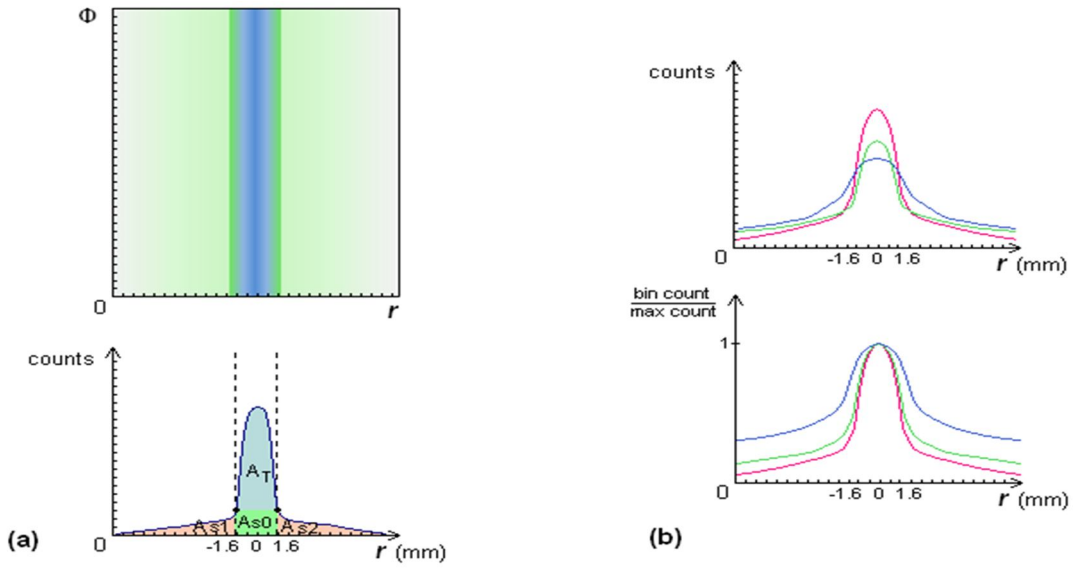

FIGURE 4.13: *(a)* Definition of the scatter areas (As1, As2, As0) and the true events areas (A_T); *(b)* Profile peak normalization.

The integration limits that divide the three areas are defined manually, by choosing the turning point of the profile plot.

$$SF = \frac{A_{S0}+A_{S1}+A_{S2}}{A_T+A_{S0}+A_{S1}+A_{S2}} \times 100 \quad (\%) \qquad (4.9)$$

Unlike phantom 2, the third phantom's activity cylinder is not centered in the phantom's center. Therefore its sinogram must be processed first in order to obtain scatter fraction values. The centered sinogram was

obtained by acquiring the maximum count value in each horizontal line (fig. 4.13-a), i.e., the maximum value for each angle. Afterwards each line is displaced so that the maximum coincides with r=0.

4.5.2 Event allocation analysis

During the LOR retrieval process, it is possible to account for the correctly and incorrectly allocated interactions, regarding both the gamma ray sorting algorithm, and the Compton tracing algorithms. Using the ratios between the correctly and incorrectly allocations enables one to compare the two Compton tracing algorithms, and assess the quality of the parent gamma ray allocation algorithm. This analysis was performed using data for the UTAH-like phantom filled with water and with smeared and clustered coordinates and energy. The results will be present in section 4.6.1.5.

4.6 Results

4.6.1 Image analysis

From all the LOR sets described in section 4.3.3, there are only four relevant ones for the PET image comparisons as stated in 4.5.1: the golden standard 350-650keV set with the original coordinates and energies, the traditional PET simulation set, the unknown gamma closest to the center 350-650keV, and the unknown gamma shortest LOR 350-650keV. Since real PET phantoms are always constituted by some material, then the simulated empty phantoms (vacuum) serve only as control data.

4.6.1.1 Effect on the image of the gamma ray allocation algorithm

In order to discern the effects on the image due to the gamma sorting algorithm, as explained in section 4.3.1, from the ones created by the Compton tracing algorithms, two sets of sinograms and images were used. The first set corresponds to a LOR selection without the gamma sorting algorithm (i.e., using the original interaction sequence), and the second set with the gamma sorting algorithm. For this comparison the empty UTAH-like phantom was used, since the scatter fraction like phantom presents an activity region too small, and so that there is no interference of photons scattered in water.

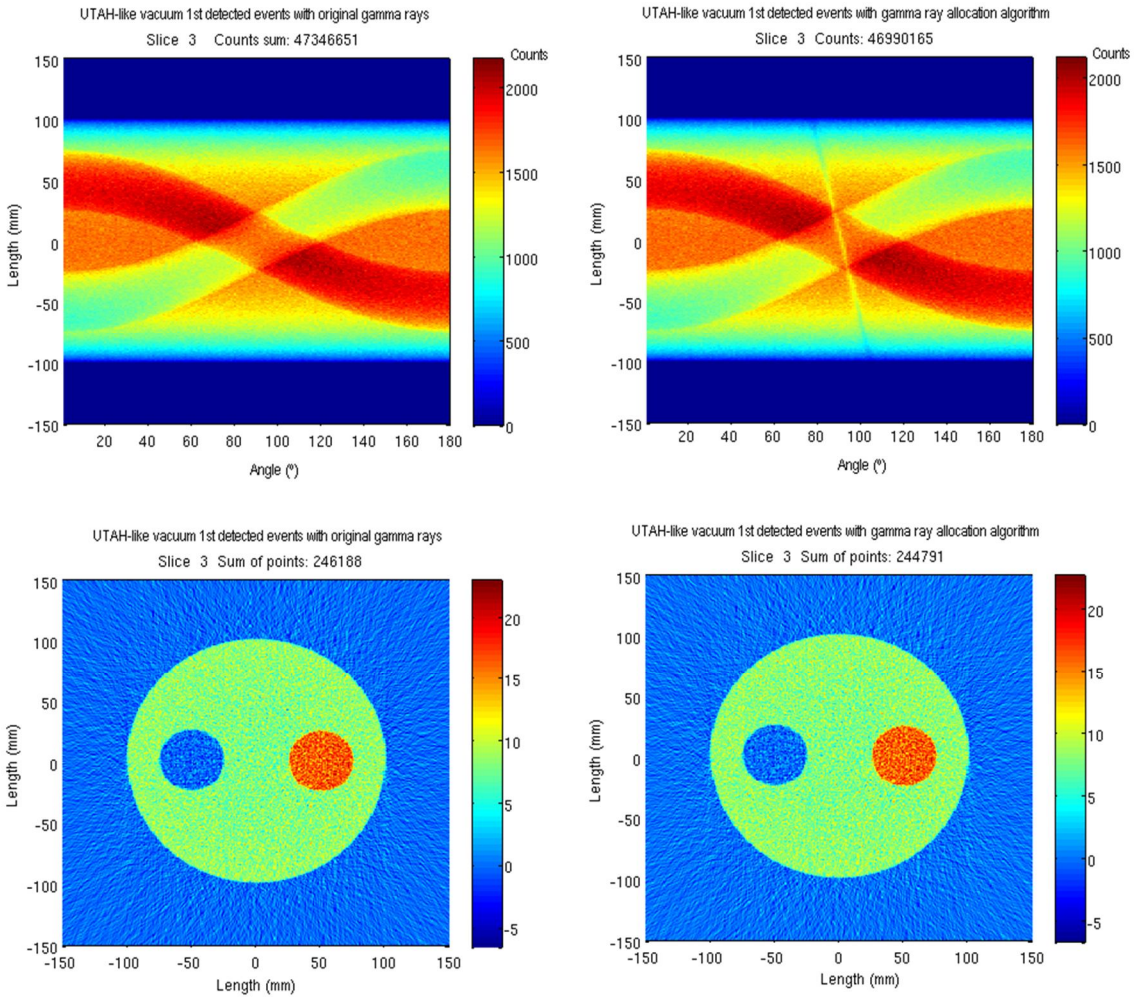

FIGURE 4.14: Reconstructed images of the UTAH-like phantom in vacuum using LORs from the golden standard (left) versus the golden standard with gamma allocation algorithm (right). The interaction sequence is known in both cases.

TABLE 4.2: Image contrast ratios correspondent to the figure 4.14 as explained in figure 4.12

	A_0	A_1	A_2	C_{01}	C_{02}	C_{21}
Golden Standard	-22.6645	2592.58	5214.71	-0.00874206	-0.00434626	2.0114
Golden Standard with gamma allocation	-18.0619	2535.63	5088.55	-0.00712324	-0.00354952	2.00682

4.6.1.2 Effect on the image of the attenuation correction

In order to ascertain the proper functioning of the attenuation correction routine, and check if no undesirable effects or artifacts were created, the following images were used as example:

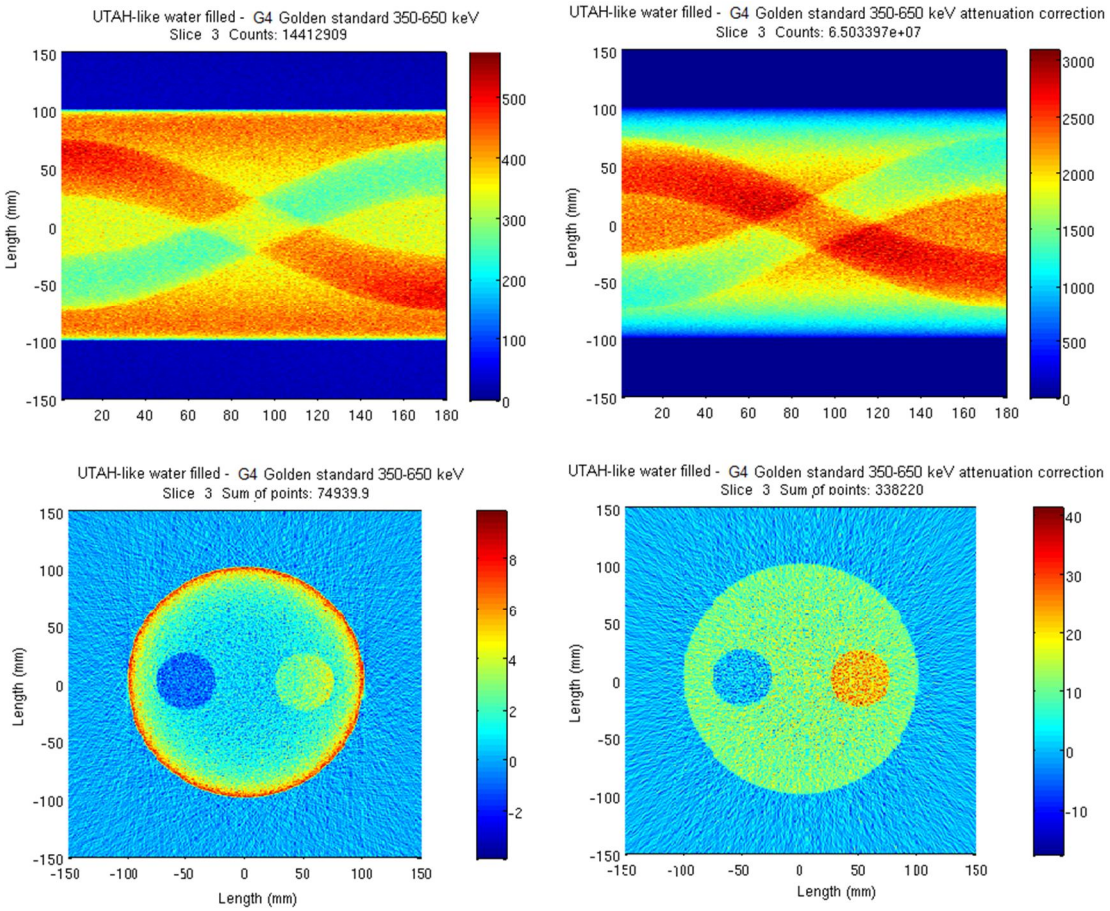

FIGURE 4.15: UTAH-like phantom in water from the GEANT4 Golden standard 350-630 keV file; *Left:* Without attenuation correction; *Right:* With attenuation correction

4.6.1.3 Image contrast

Detector response corresponding to R_{E511}=10% and $R_{X511,\ Y511,\ Z511}$=0.5mm, angle bin size of 1º, *r* bin size of 1 mm:

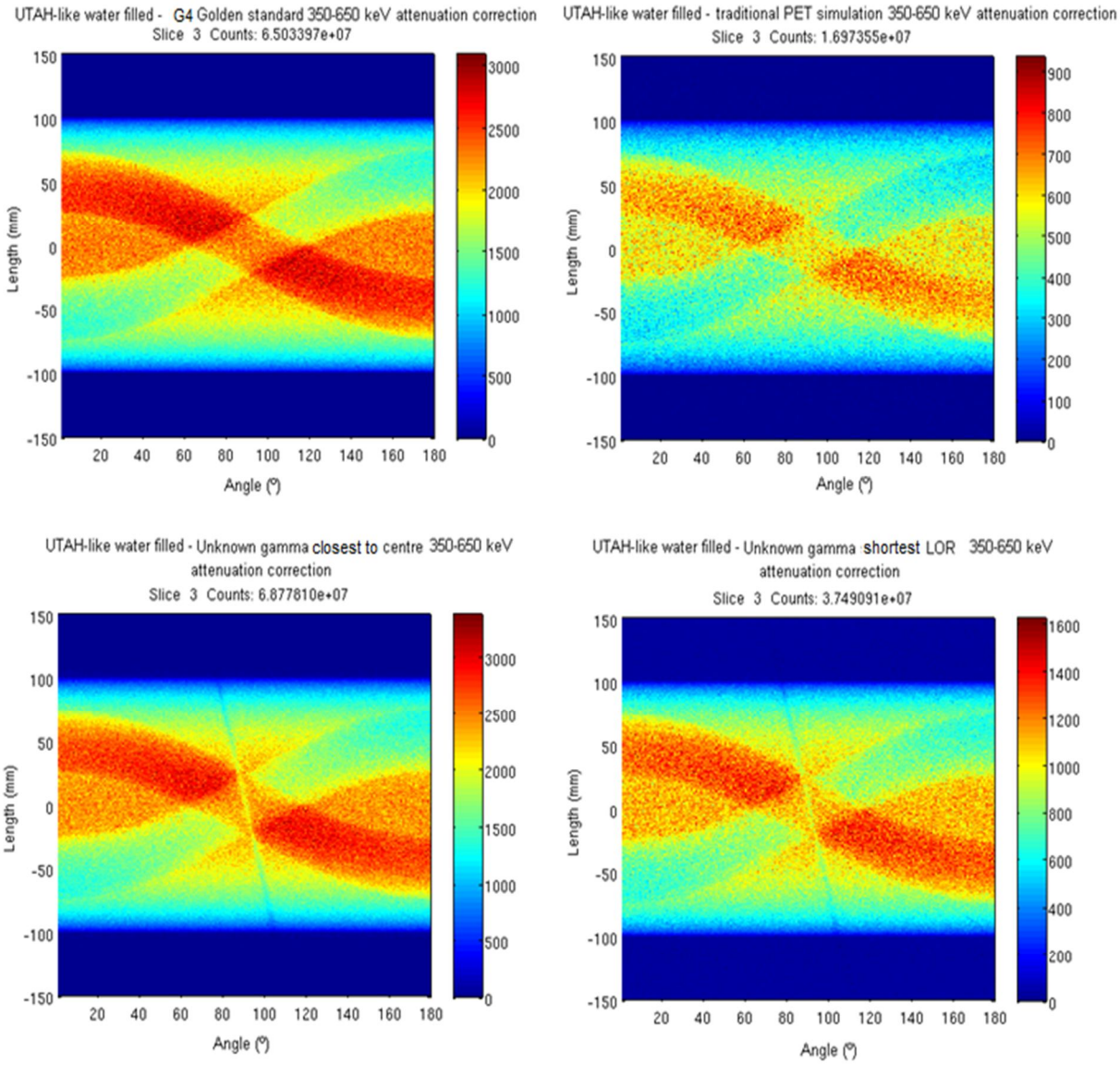

FIGURE 4.16: Sinograms of the UTAH-like phantom in water, with attenuation correction.

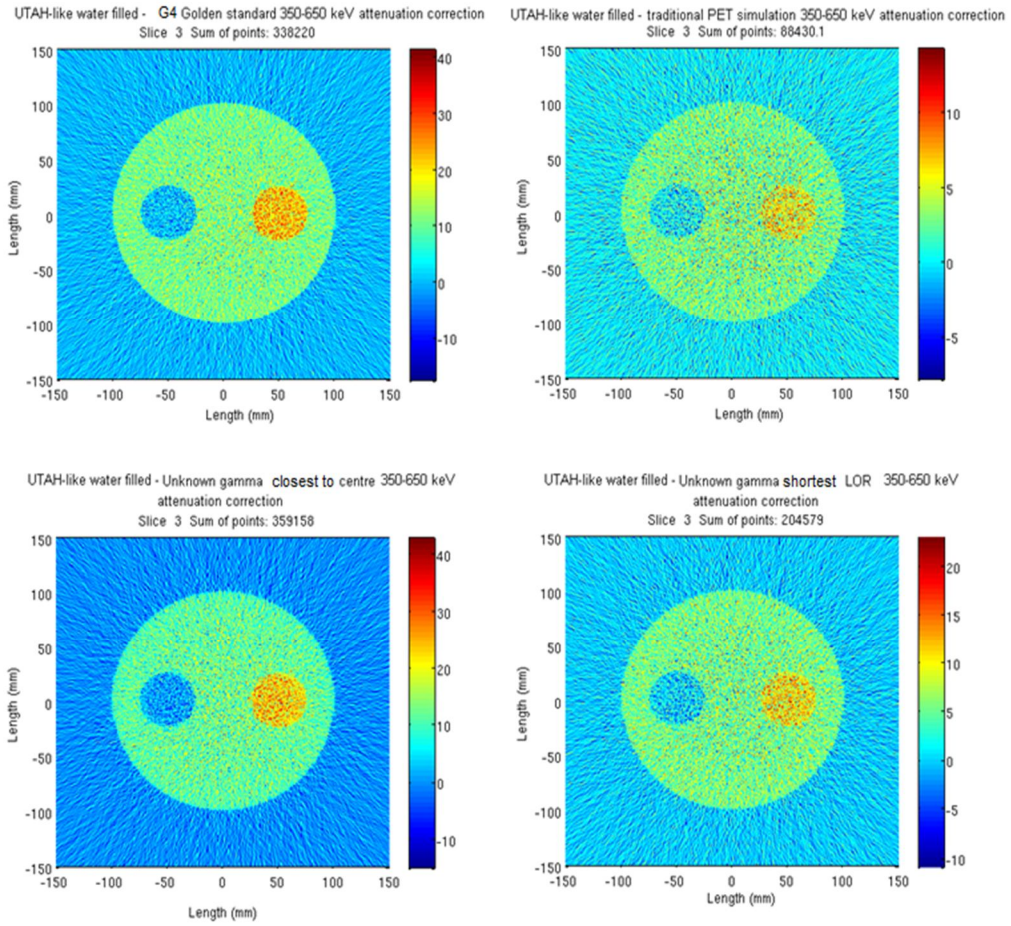

FIGURE 4.17: Images of the UTAH-like phantom in water, with attenuation correction.

TABLE 4.3: Image contrast ratios correspondent to the figure 4.17.

	A_0	A_1	A_2	C_{01}	C_{02}	C_{21}
Golden Standard 350-650 keV	294.635	3502.79	7017.53	0.0841144	0.0419856	2.00341
Traditional PET 350-650 keV	47.9102	887.09	1756.65	0.0540083	0.0272736	1.98024
Unknown gamma closest to center 350-650 keV	278.877	3622.81	7197.93	0.0769781	0.0387441	1.98684
Unknown gamma shortest LOR 350-650 keV	78.1984	1353.18	2812.63	0.0577885	0.0278026	2.07853

Detector simulation of R_{E511}=20%, and $R_{X511, Y511, Z511}$=2mm, angle bin size of 1°, *r* bin size of 1 mm:

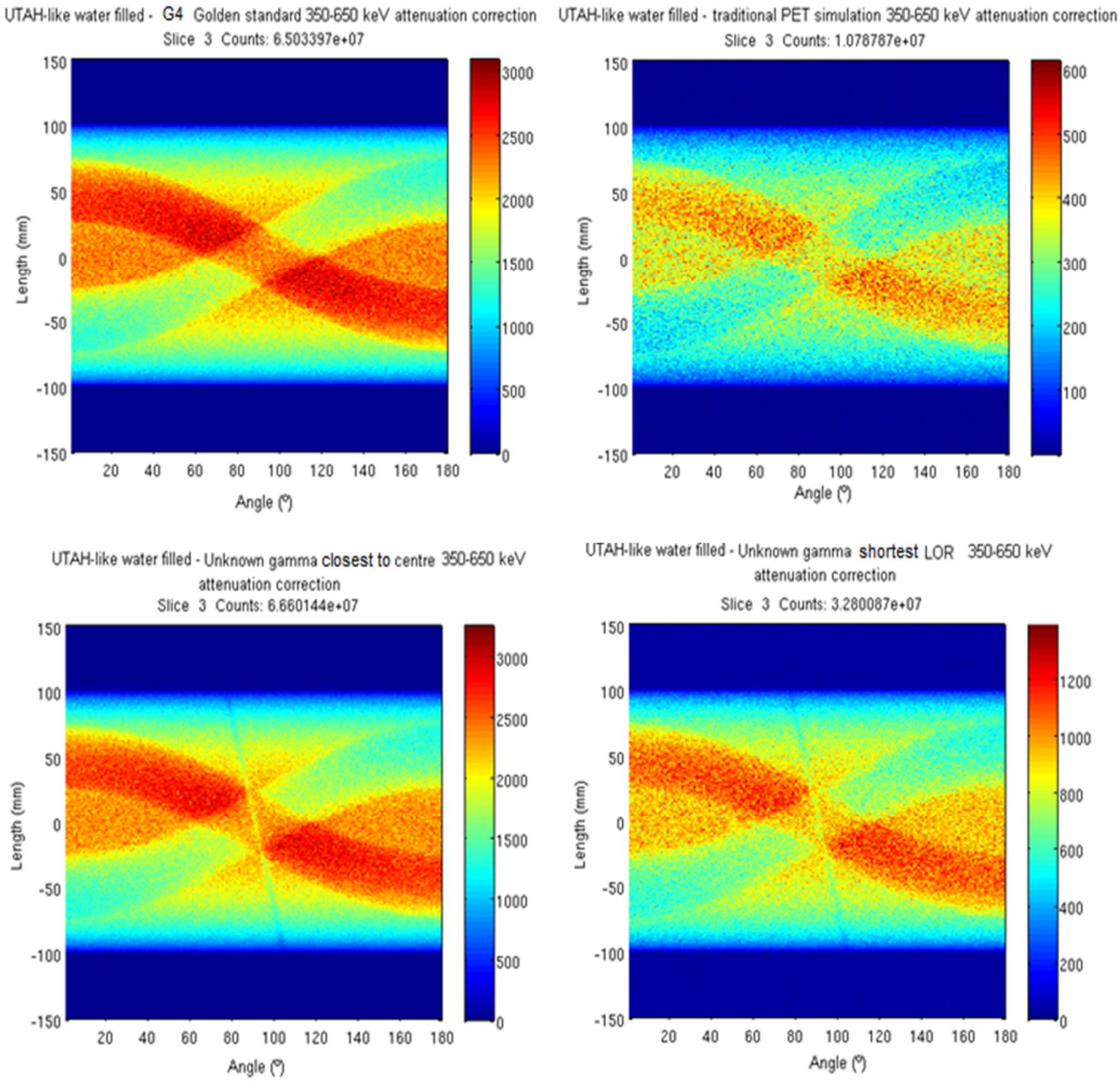

FIGURE 4.18: Sinograms of the UTAH-like phantom in water, with attenuation correction

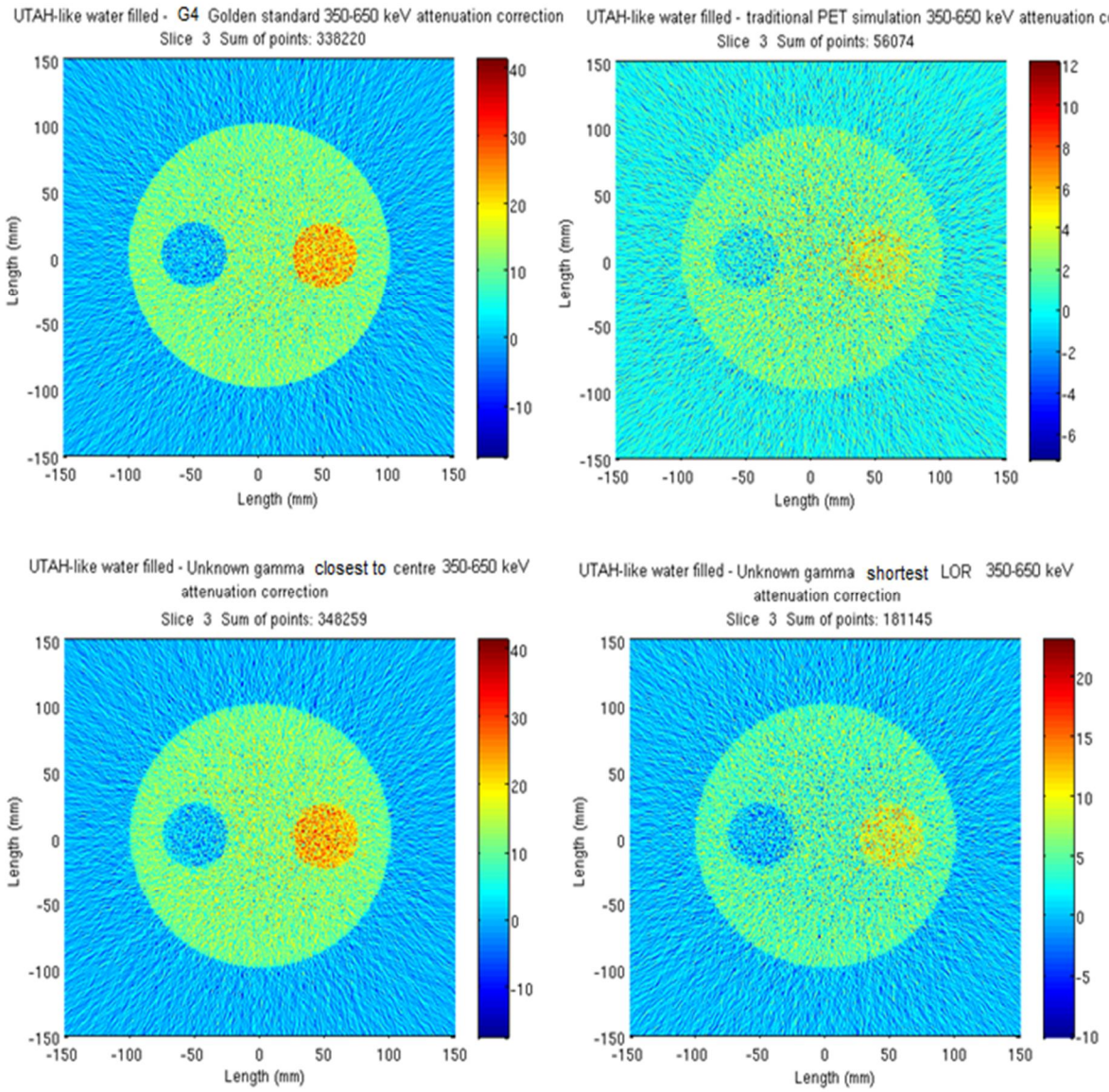

FIGURE 4.19: Images of the UTAH-like phantom in water, with attenuation correction.

TABLE 4.4: Image contrast ratios correspondent to the figure 4.19.

	A_0	A_1	A_2	C_{01}	C_{02}	C_{21}
Golden Standard 350-650 keV	294.635	3502.79	7017.53	0.0841144	0.0419856	2.00341
Traditional PET 350-650 keV	27.0565	553.115	1118.17	0.0489167	0.0241973	2.02158
Unknown gamma closest to center 350-650 keV	293.766	3727.95	7417.21	0.078801	0.039606	1.98962
Unknown gamma shortest LOR 350-650 keV	110.041	1654.14	3314.64	0.0665247	0.0331984	2.00385

4.6.1.4 Scatter Fraction

Phantom 2:

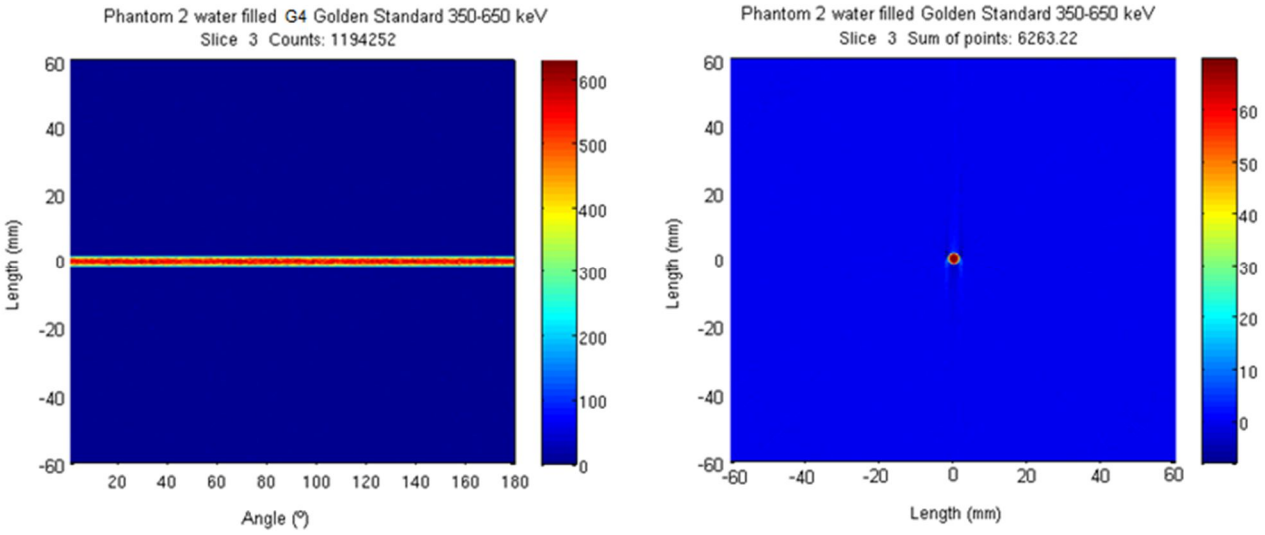

FIGURE 4.20: Golden Standard 350-650 keV sinogram and image from phantom 2.

Detector simulation of R_{E511}=10%, and $R_{X511, Y511, Z511}$=0.5mm, angle bin size of 1º, *r* bin size of 0.4mm:

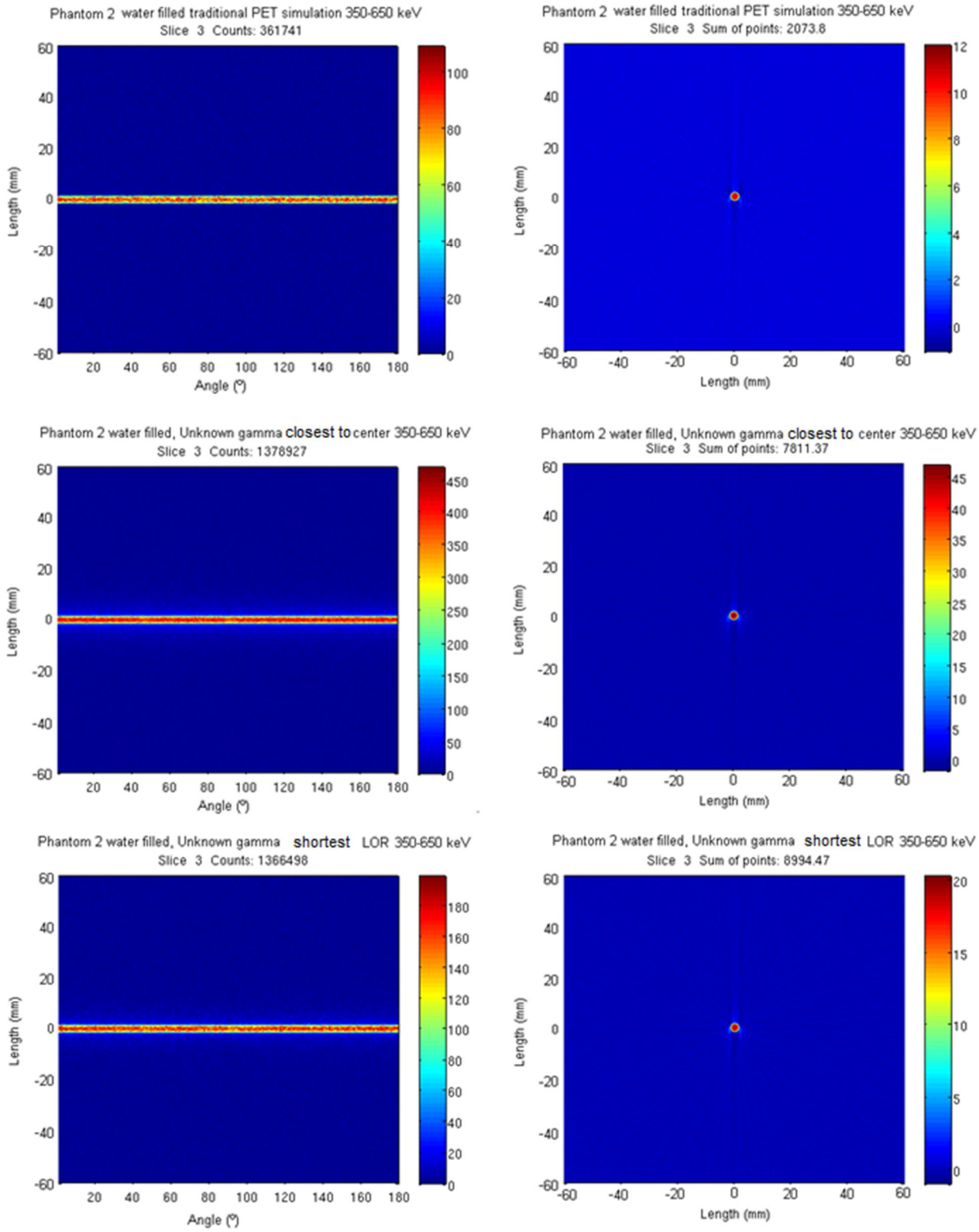

FIGURE 4.21: Detector response 350-650 keV sinograms and images from phantom 2.

Scatter Fraction comparison of the sinograms:

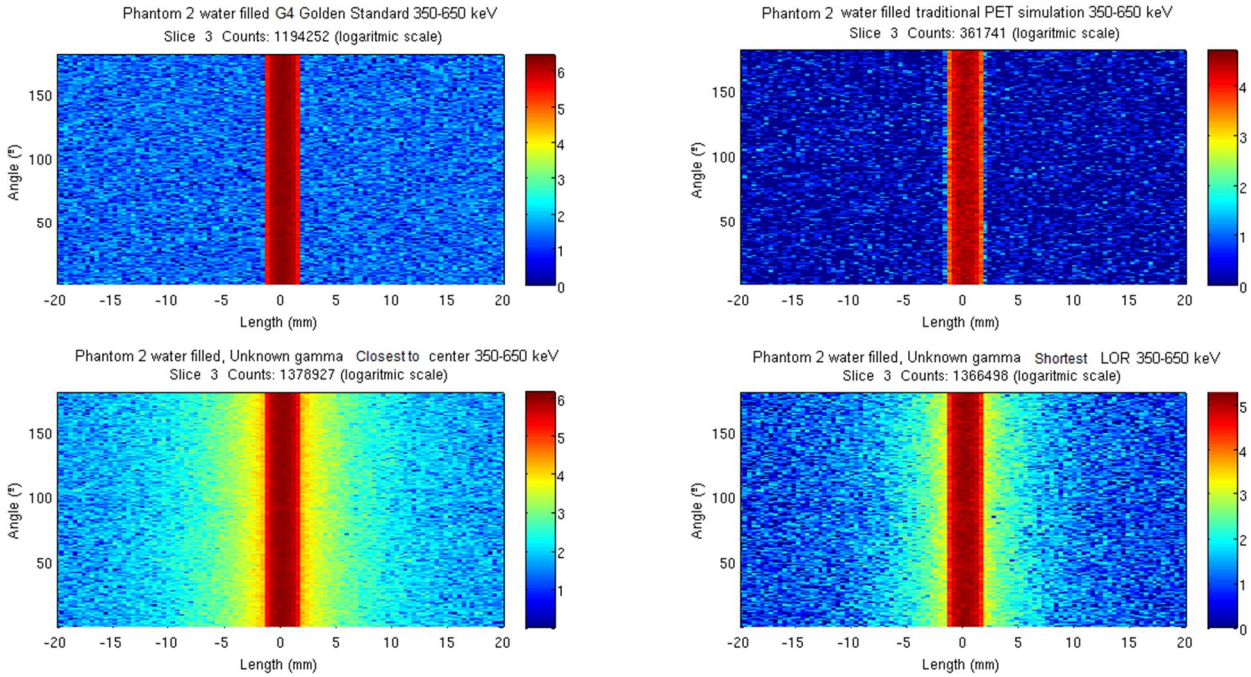

FIGURE 4.22: Phantom 2 sinograms in logarithmic scale.

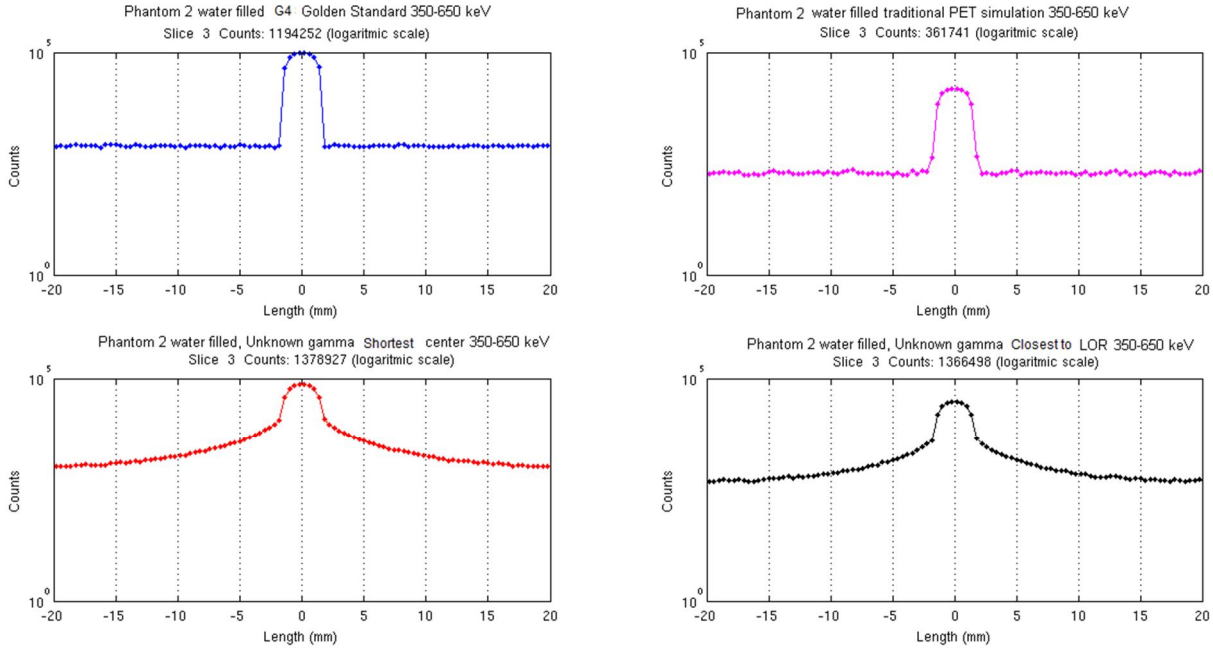

FIGURE 4.23: Phantom 2 count profiles of the sinograms in figure 4.22

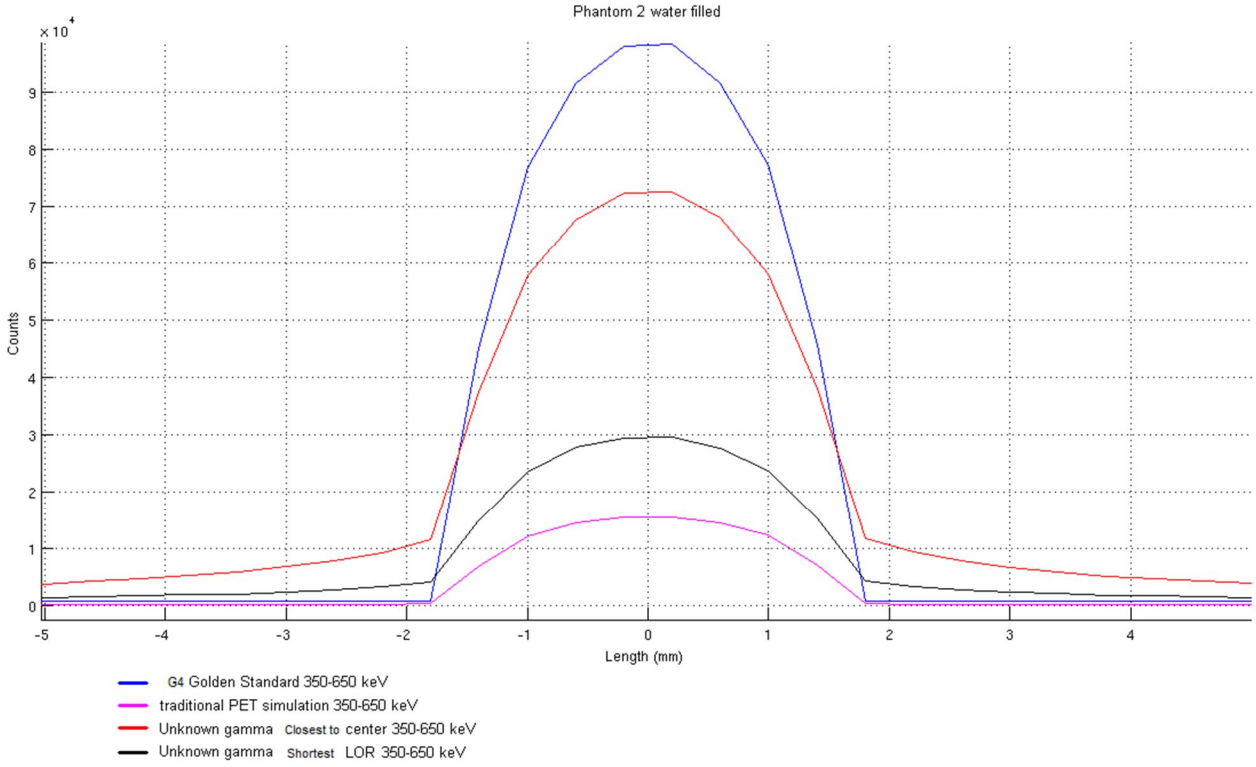

FIGURE 4.24: Superimposed count profiles of the sinograms for phantom 2 in figure 4.22.

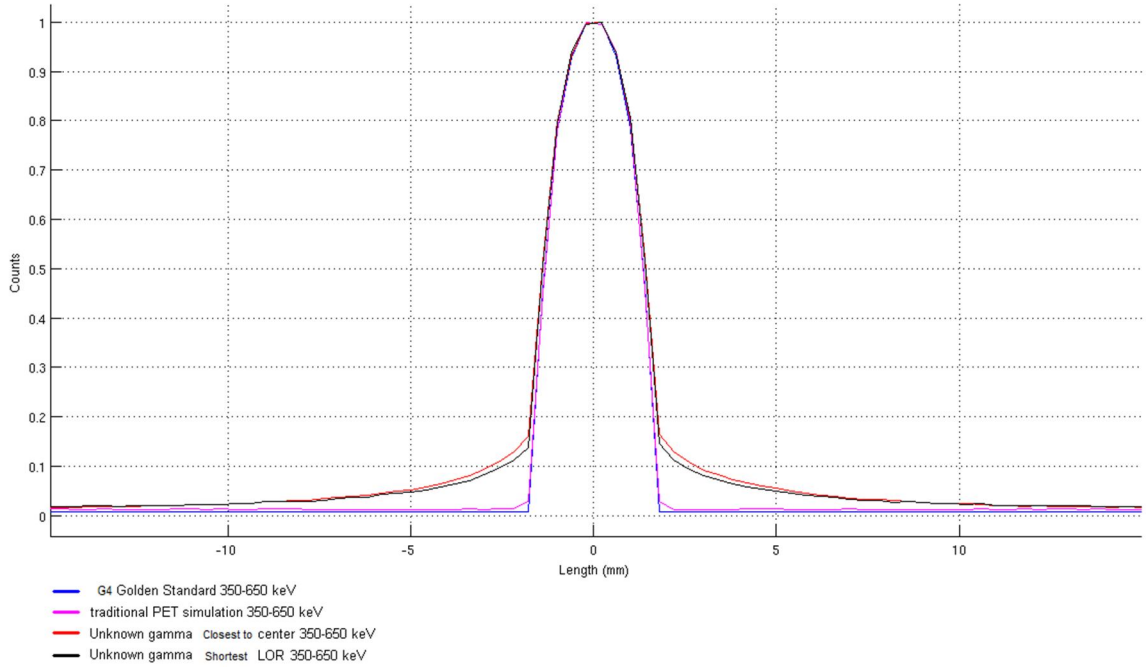

FIGURE 4.25: Superimposed normalized count profiles of the sinograms for phantom 2 in figure 4.22.

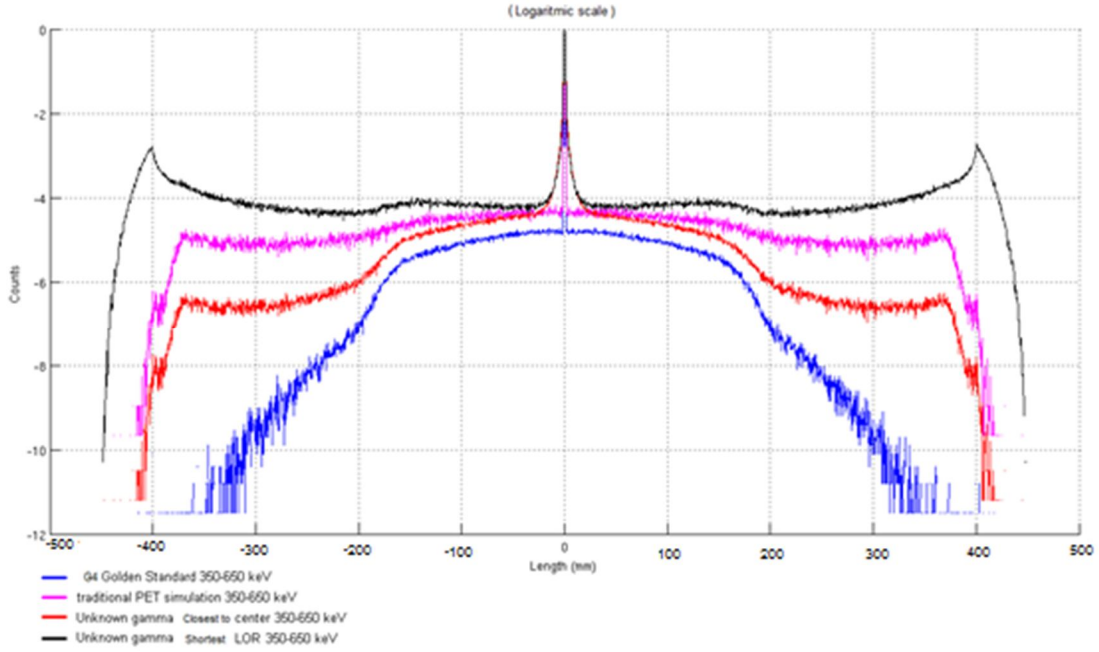

FIGURE 4.26: Superimposed normalized count profiles of the sinograms for phantom 2 in figure 4.22 without zoom.

TABLE 4.5: Scatter fractions corresponding to the figure 4.22, as explained in figure 4.13.

	A_{s1}	A_{s0}	A_{s2}	A_T	SF (%)
Golden Standard 350-650 keV	283695	6786	284976	618795	0.481856
Traditional PET 350-650 keV	130696	2519	131112	97414	0.730708
Unknown gamma closest to center 350-650 keV	453244	92832	453912	378939	0.725193
Unknown gamma shortest LOR 350-650 keV	587166	28378	587340	148362	0.890204

Detector simulation of R_{E511}=20%, and $R_{X511, Y511, Z511}$=2mm, angle bin size of 1º, *r* bin size of 0.4mm:

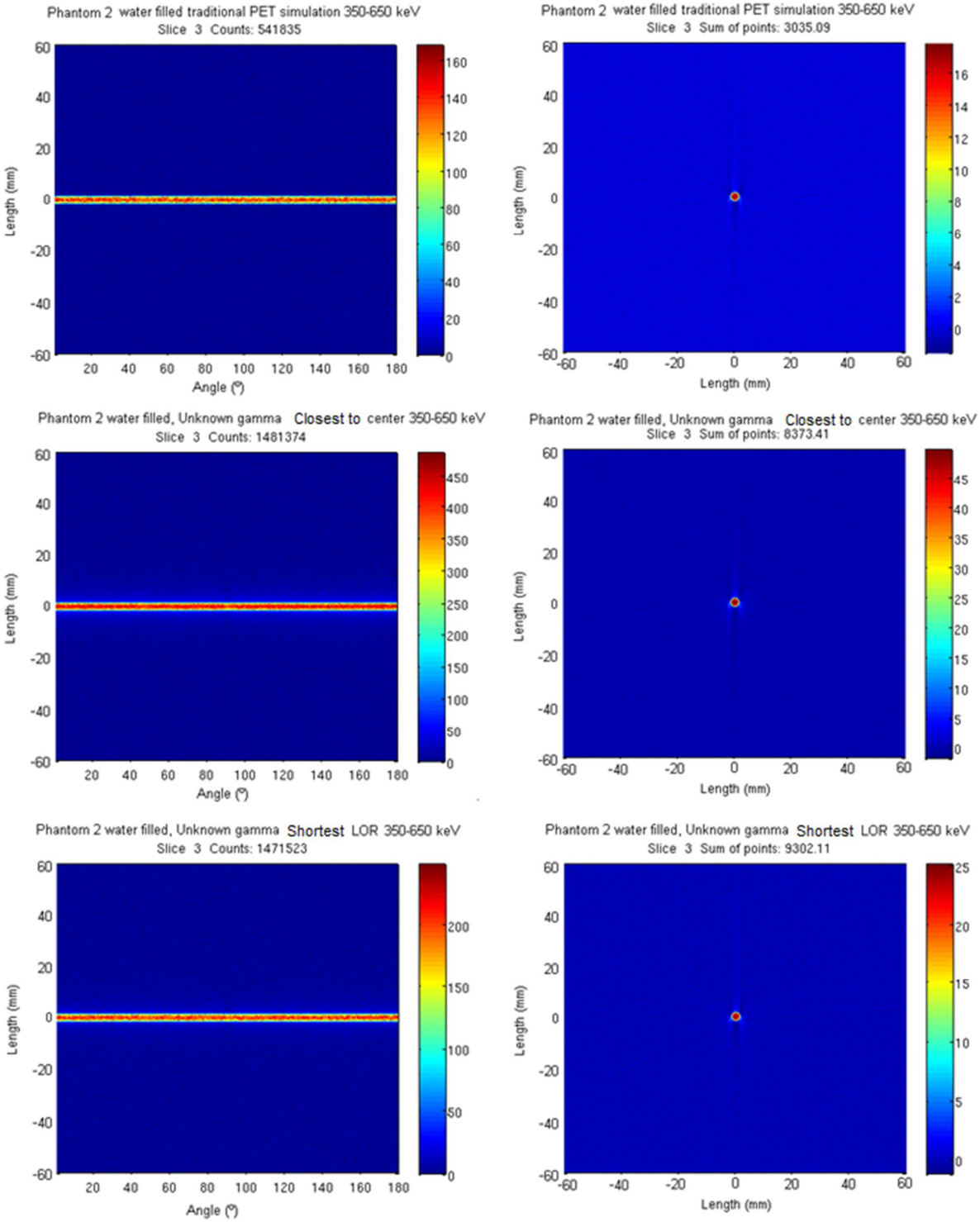

FIGURE 4.27: Detector response 350-650 keV sinograms and images from phantom 2.

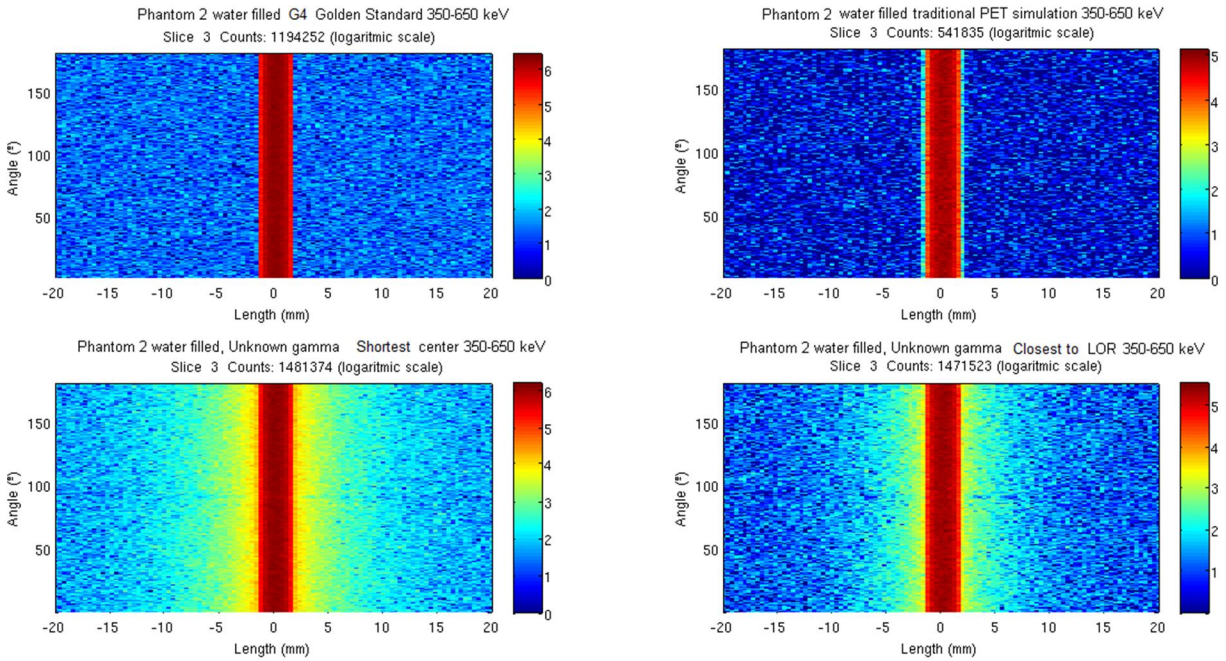

FIGURE 4.28: Phantom 2 sinograms in logarithmic scale.

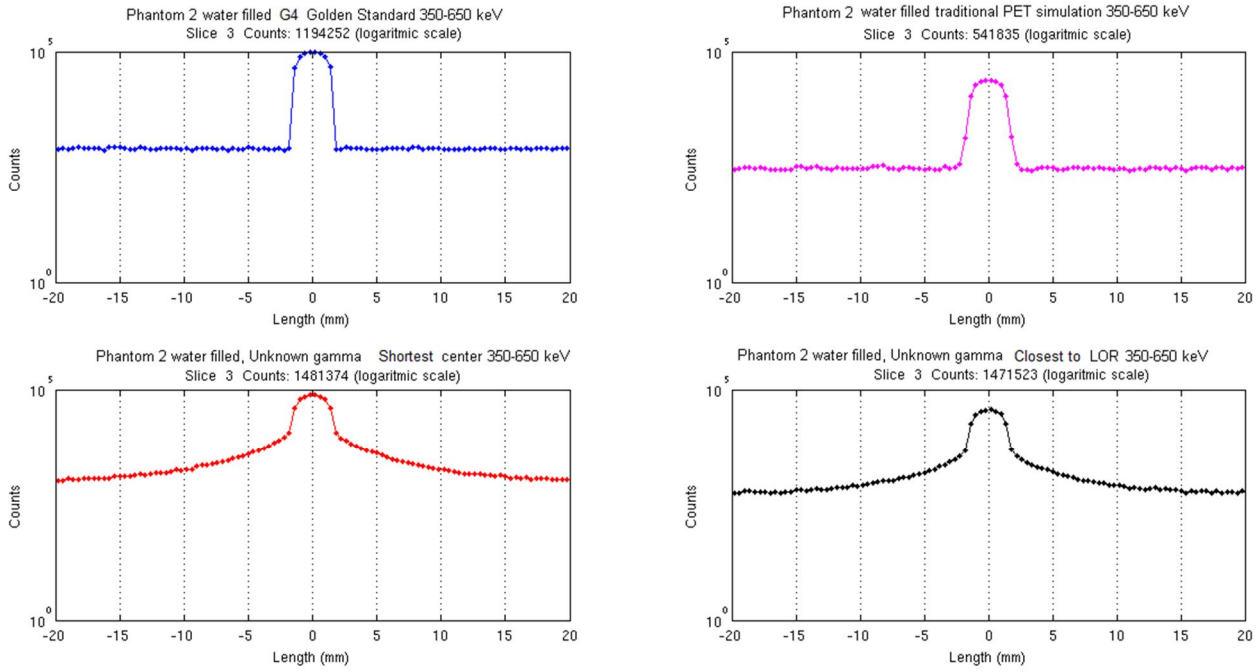

FIGURE 4.29: Phantom 2 count profiles of the sinograms in figure 4.28.

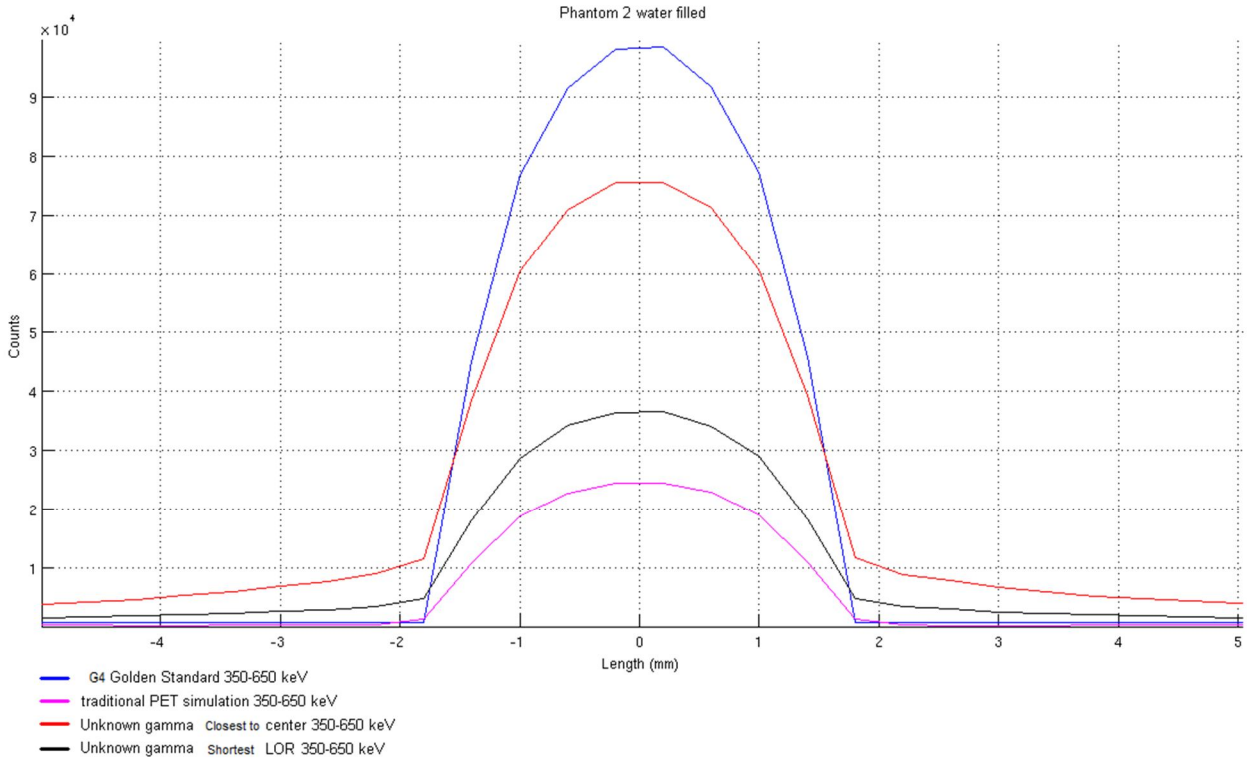

FIGURE 4.30: Phantom 2 superimposed count profiles of the sinograms in figure 4.28.

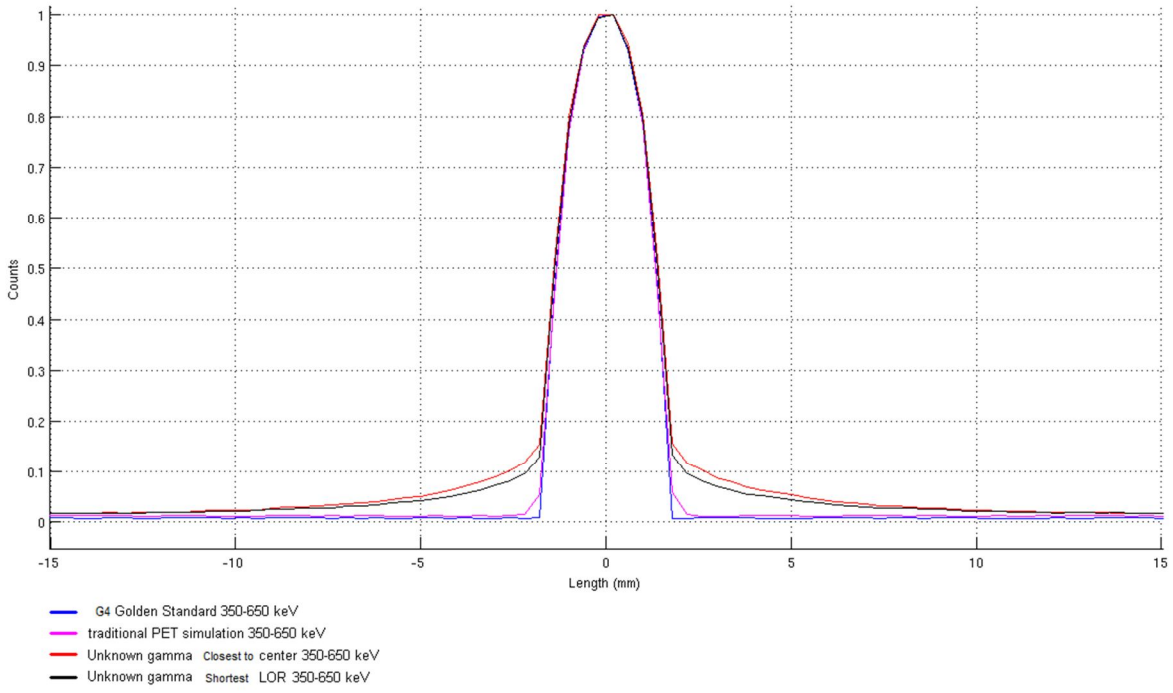

FIGURE 4.31: Superimposed normalized count profiles of the sinograms for phantom 2 in figure 4.28.

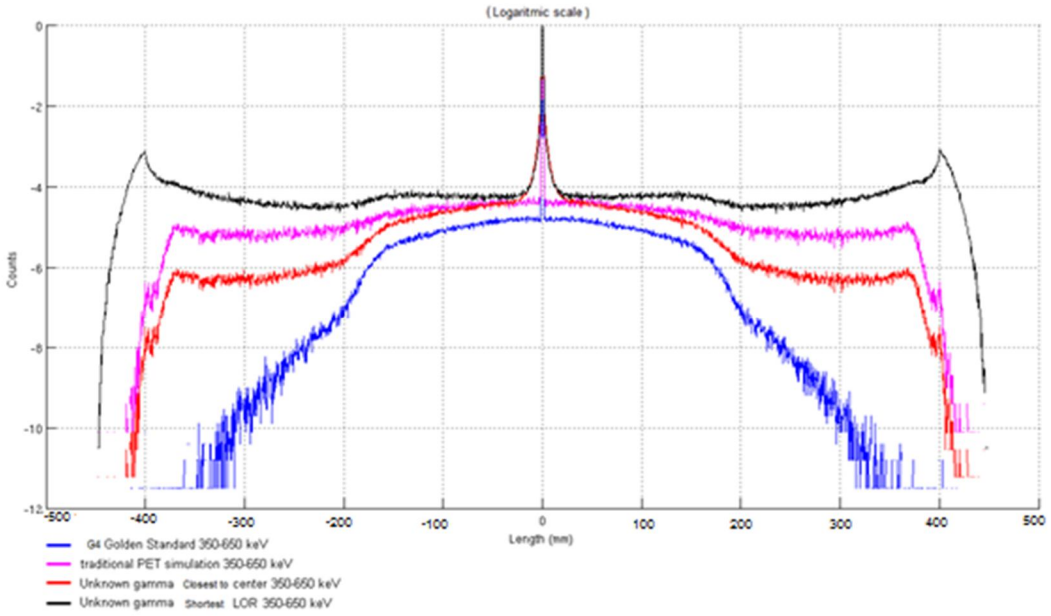

FIGURE 4.32: Superimposed normalized count profiles of the sinograms for phantom 2 in figure 4.28 without zoom.

TABLE 4.6: Scatter fractions corresponding to the figure 4.26.

	A_{s1}	A_{s0}	A_{s2}	A_T	SF (%)
Golden Standard 350-650 keV	284500	6440	284976	618336	0.482240
Traditional PET 350-650 keV	192005	3553	192225	154052	0.715685
Unknown gamma closest to center 350-650 keV	482661	80739	494880	423094	0.714391
Unknown gamma shortest LOR 350-650 keV	612818	27976	618370	194127	0.866422

Phantom 3:

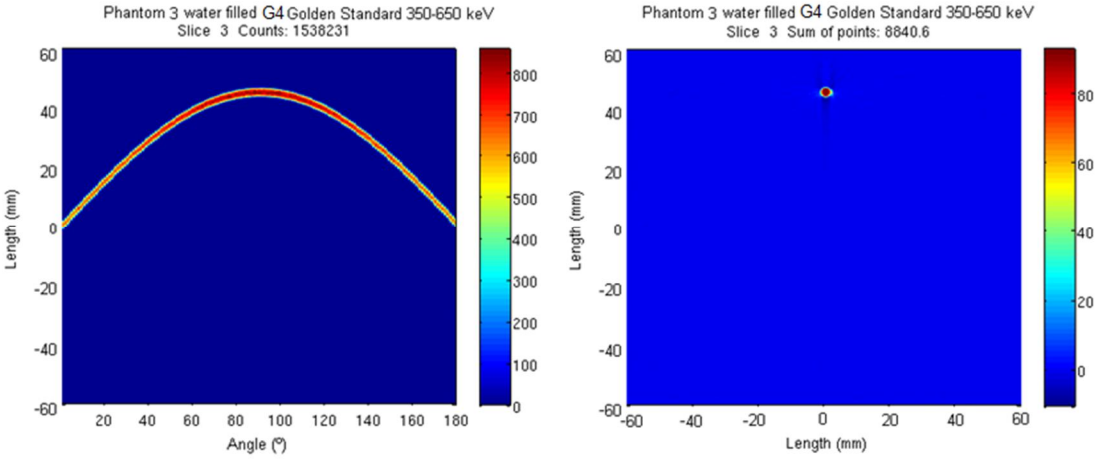

FIGURE 4.33: Golden Standard 350-650 keV sinogram and image from phantom 3.

Detector simulation of R_{E511}=10%, and $R_{X511, Y511, Z511}$=0.5mm, angle bin size of 1º, *r* bin size of 0.4mm:

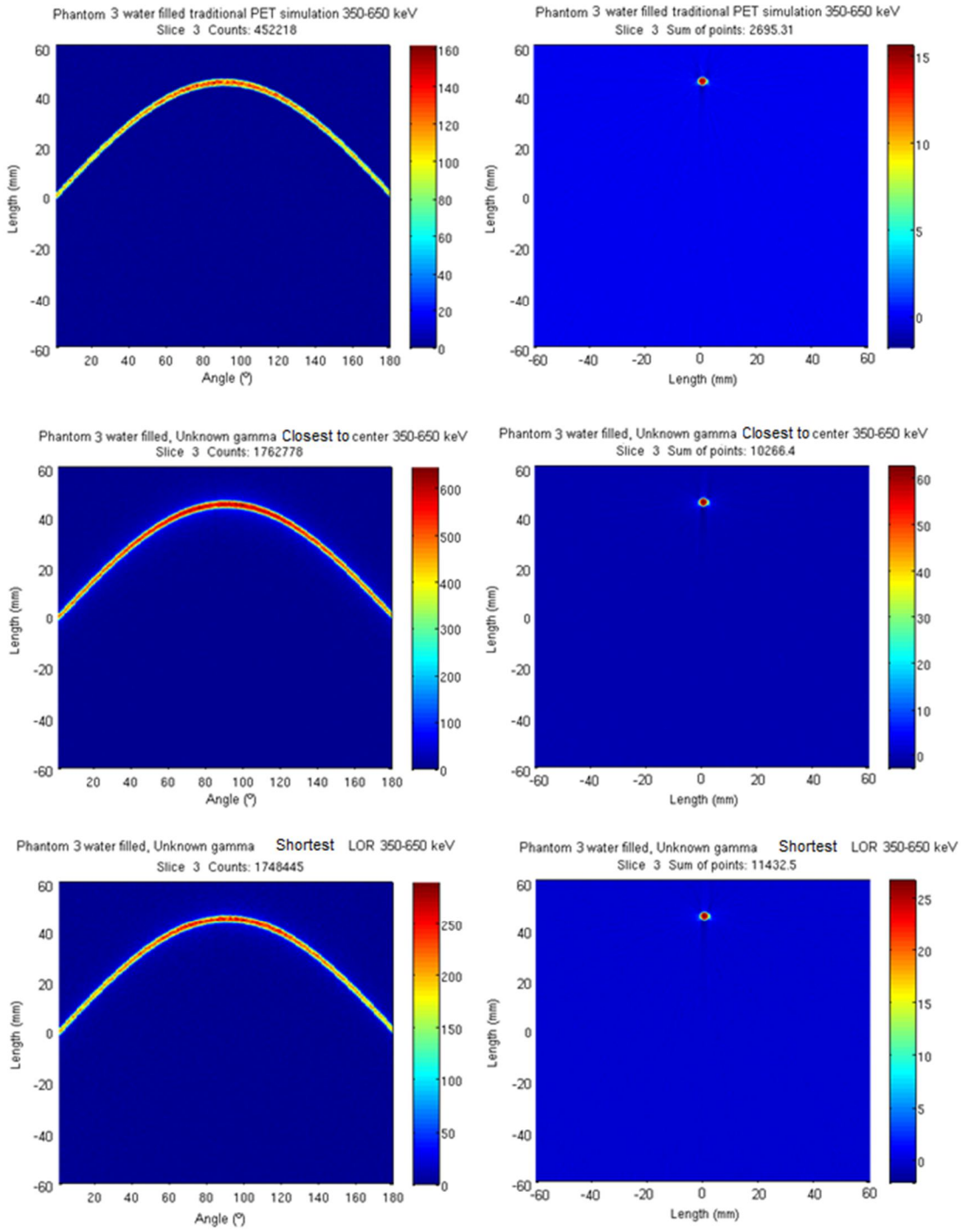

FIGURE 4.34: Detector response 350-650 keV sinograms and images from phantom 3

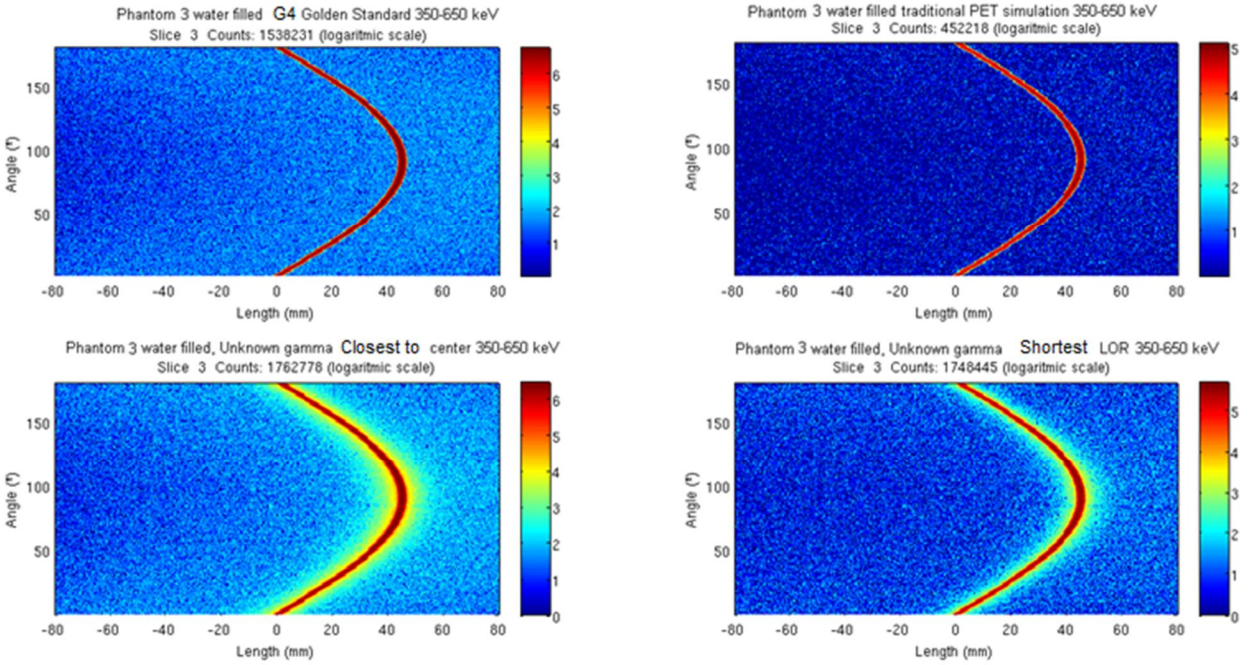

FIGURE 4.35: Phantom 3 sinograms in logarithmic scale

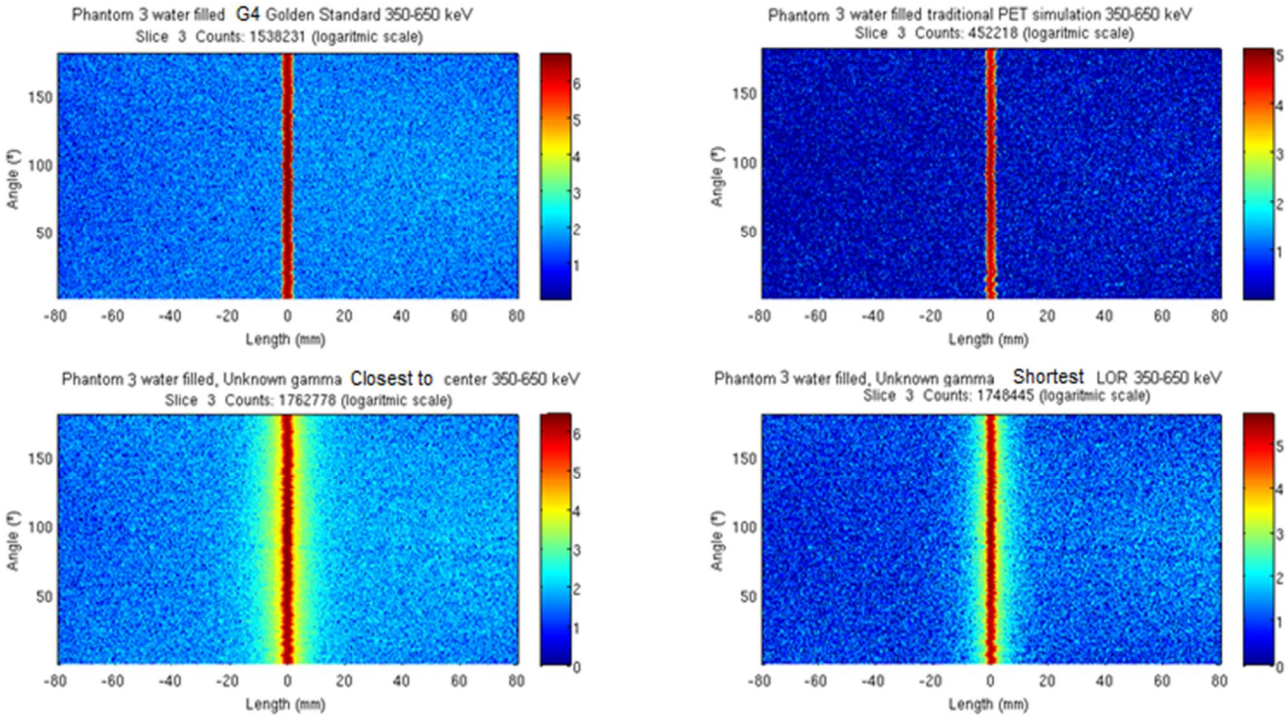

FIGURE 4.36: Phantom 3 centered activity sinograms in logarithmic scale.

From the centered sinograms, it is possible to obtain the count profiles and therefore calculate the scatter fraction values.

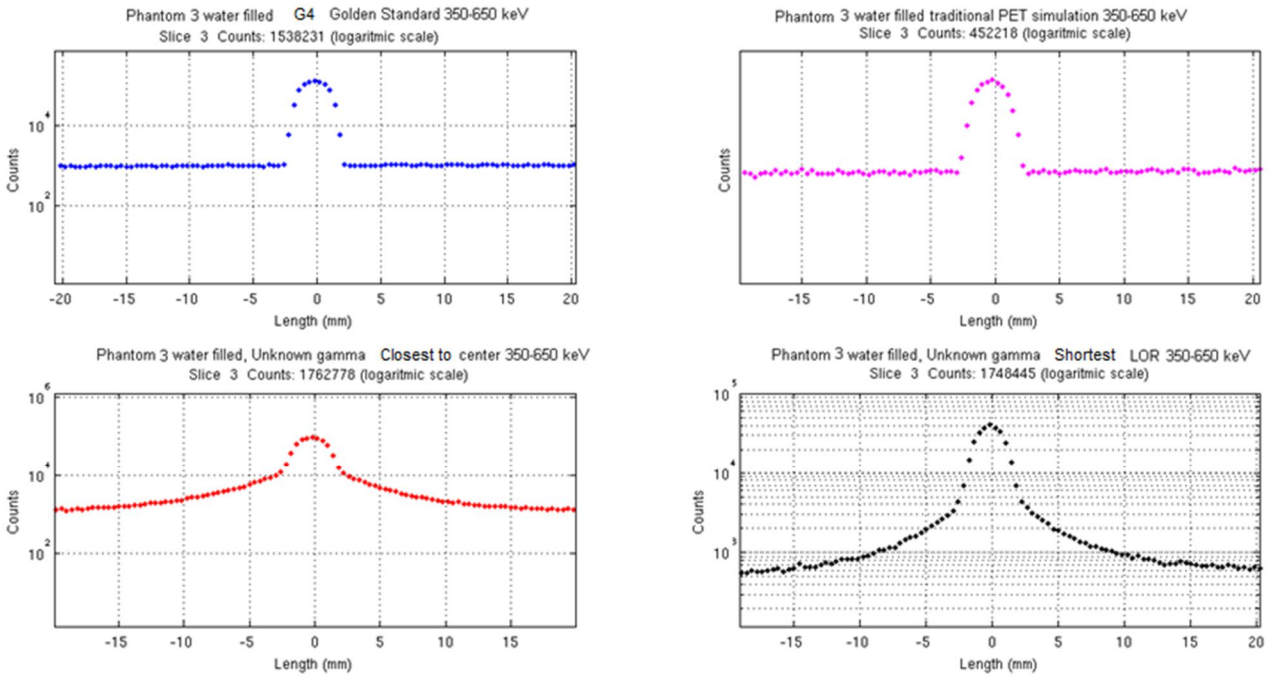

FIGURE 4.37: Phantom 3 count profiles of the sinograms in figure 4.36.

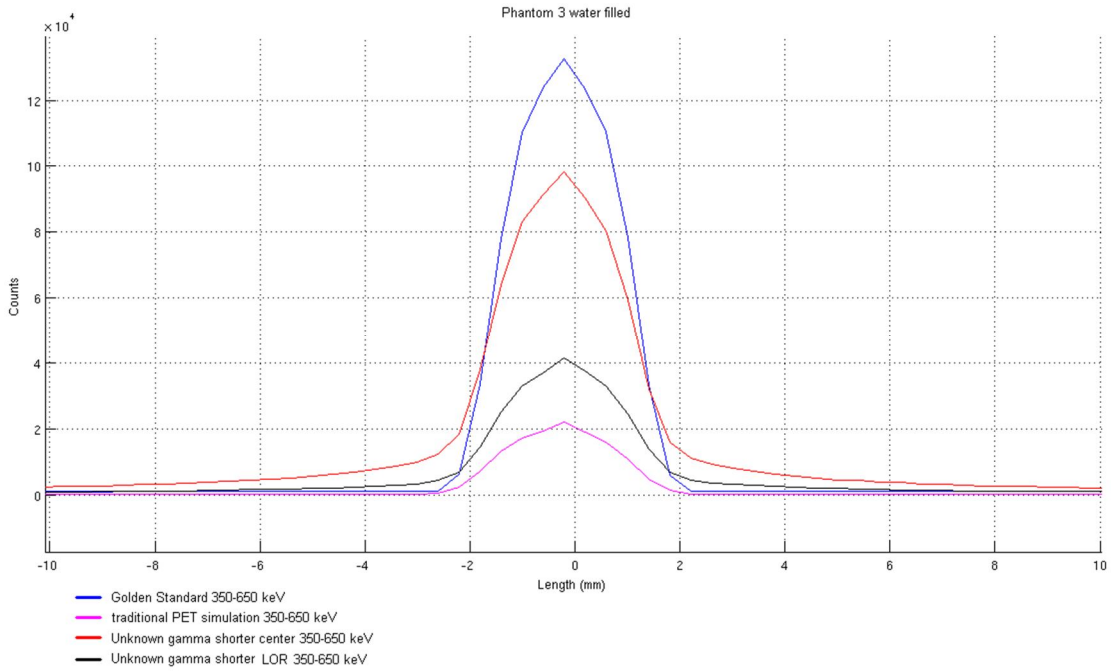

FIGURE 4.38: Phantom 3 superimposed count profiles of the sinograms in figure 4.36.

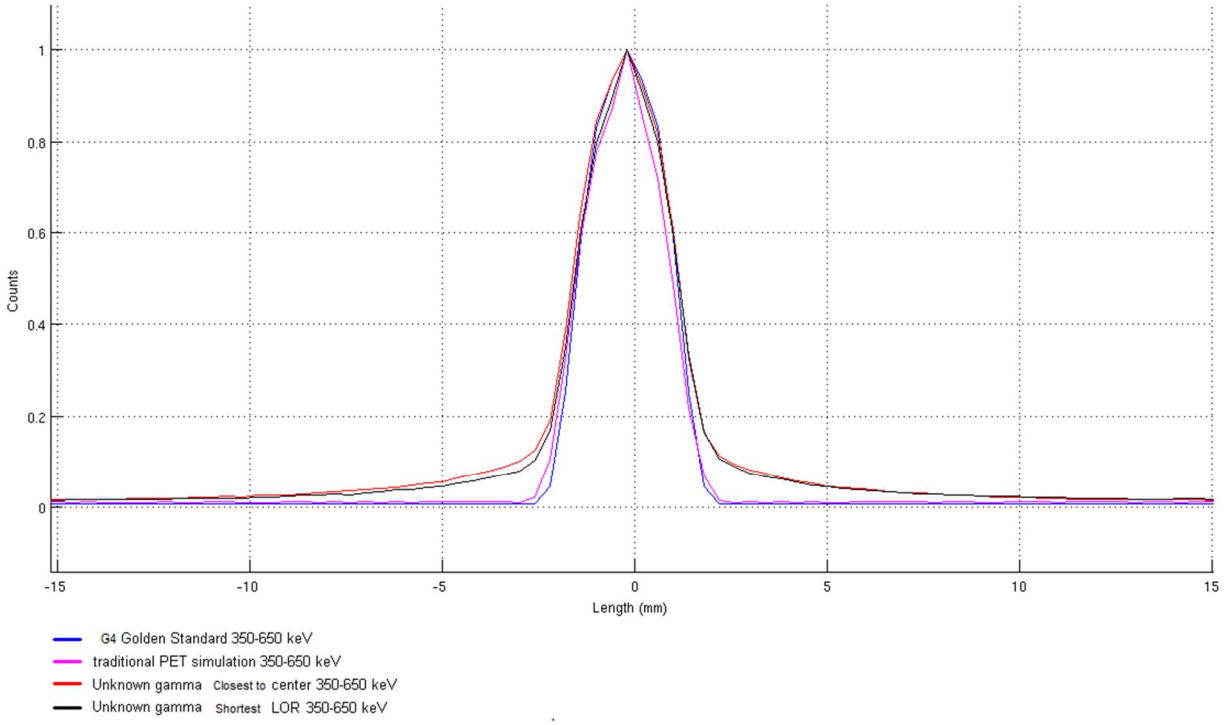

FIGURE 4.39: Phantom 3 superimposed normalized count profiles of the sinograms in figure 4.36.

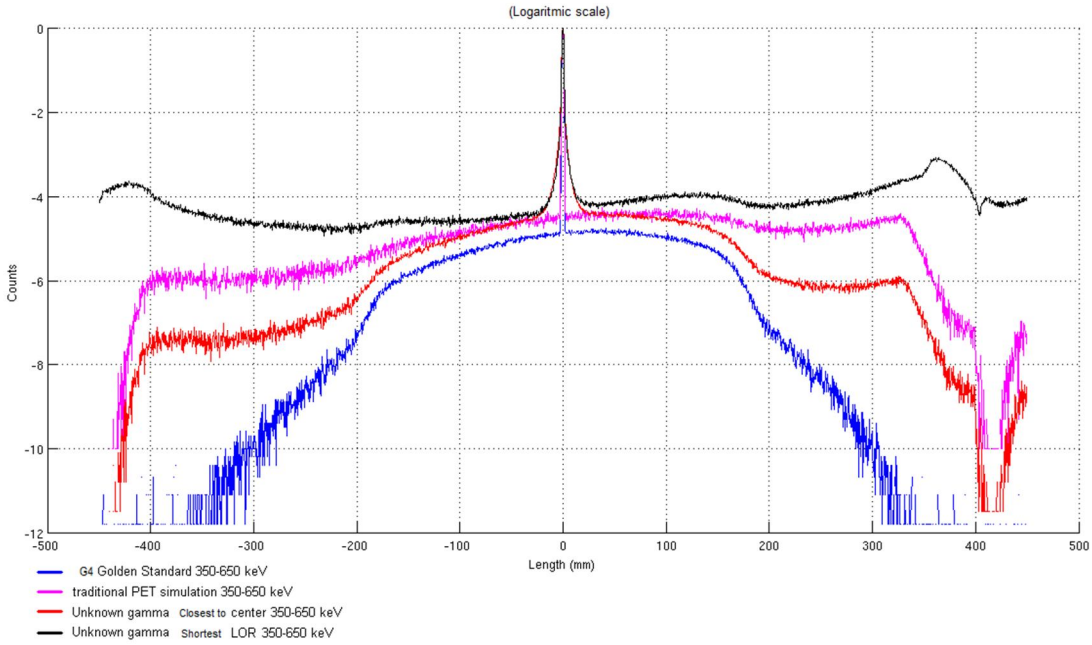

FIGURE 4.40: Phantom 3 superimposed normalized count profiles of the sinograms in figure 4.36 without zoom.

TABLE 4.7: Scatter fractions correspondent to the figure 4.34.

	A_{s1}	A_{s0}	A_{s2}	A_T	SF (%)
Golden Standard 350-650 keV	301351	10820	406810	819263	0.467404
Traditional PET 350-650 keV	117182	3081	201347	131202	0.710254
Unknown gamma closest to center 350-650 keV	457421	110154	637987	557804	0.683671
Unknown gamma shortest LOR 350-650 keV	580173	36685	941024	234851	0.869

Detector simulation of R_{E511}=20%, and $R_{X511, Y511, Z511}$=2mm, angle bin size of 1º, *r* bin size of 0.4mm:

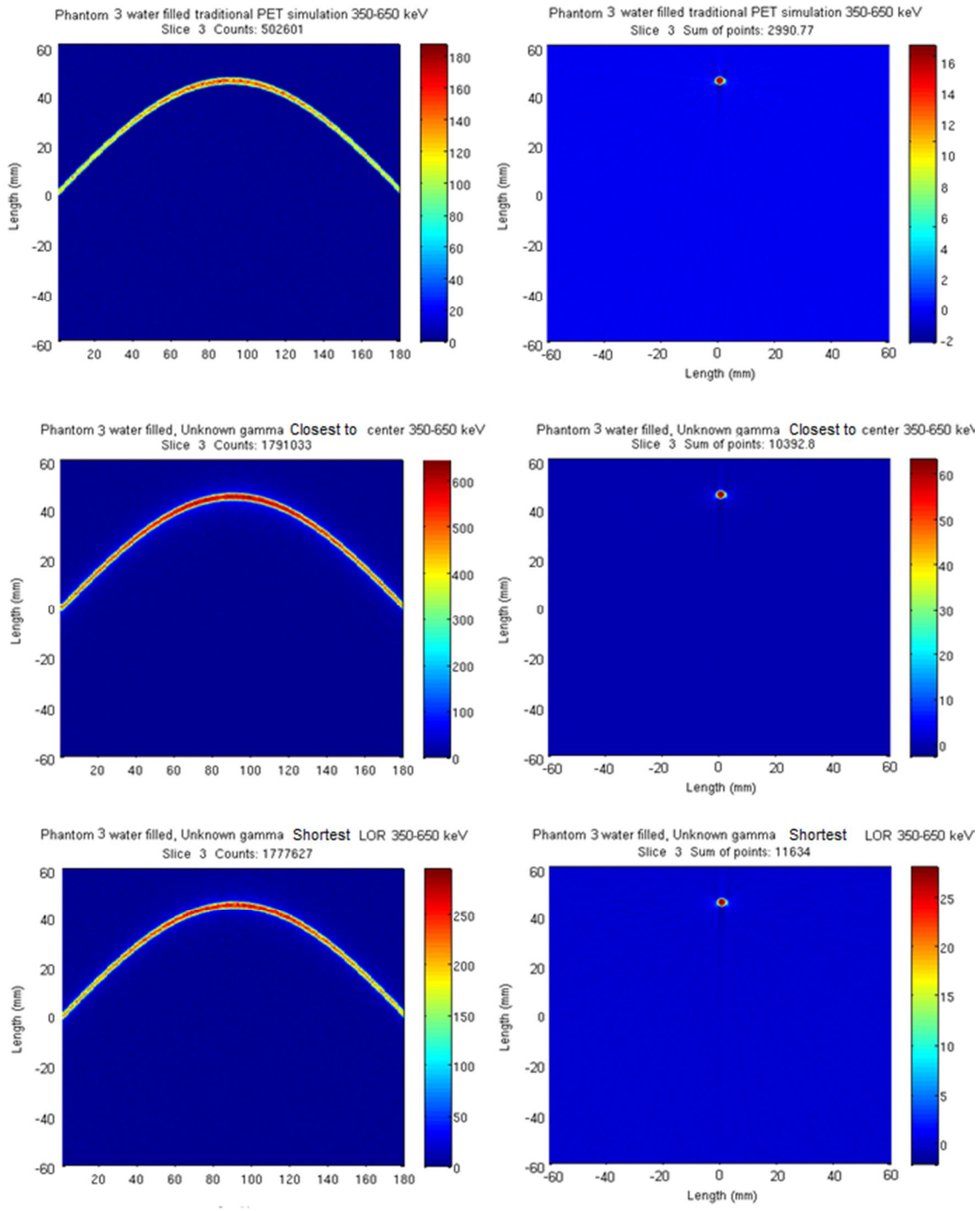

FIGURE 4.41: Detector response 350-650 keV sinograms and images from phantom 3.

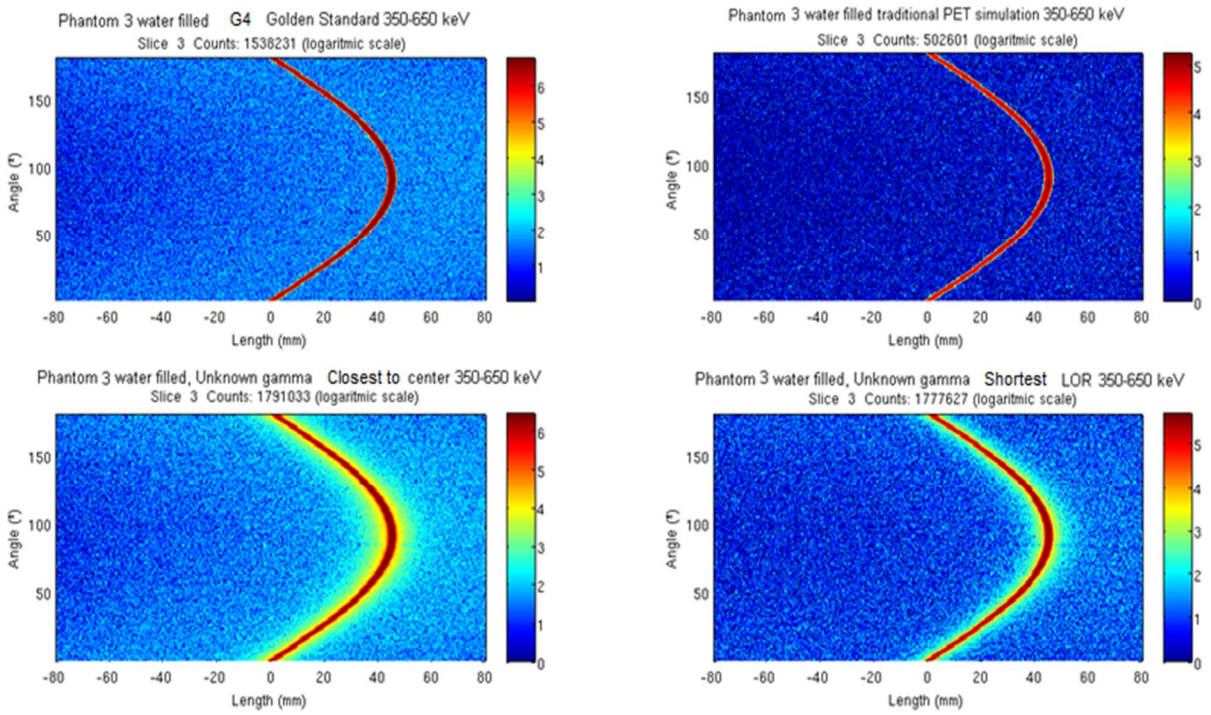

FIGURE 4.42: Phantom 3 sinograms in logarithmic scale.

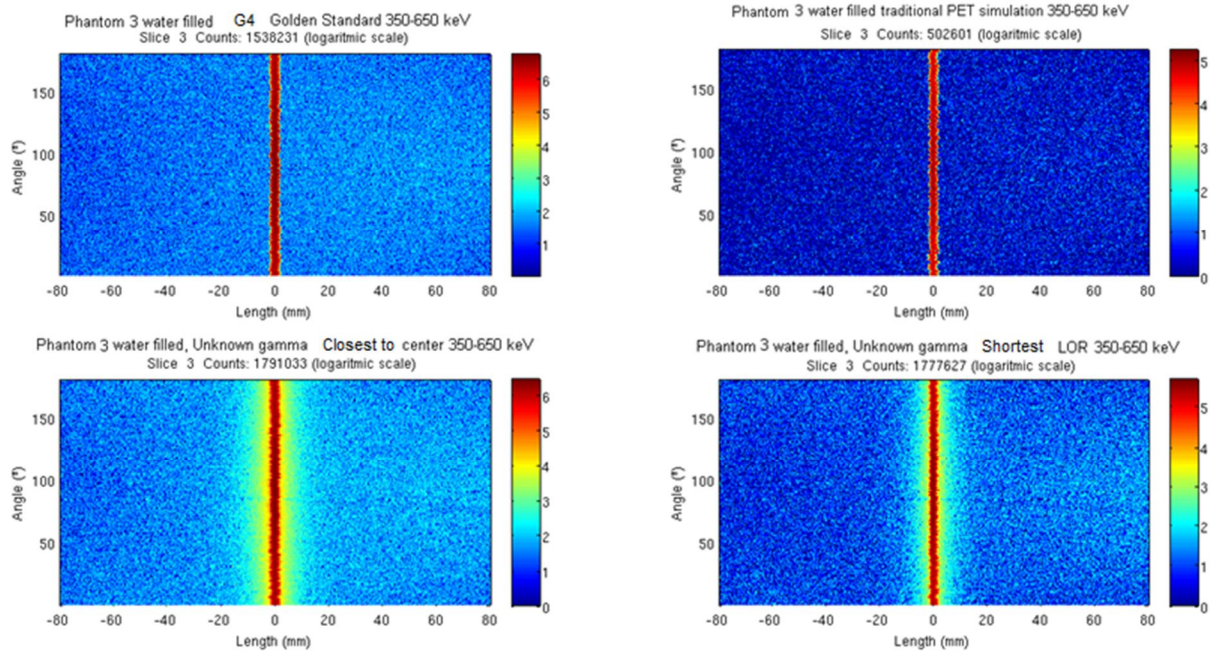

FIGURE 4.43: Phantom 3 centered activity sinograms in logarithmic scale.

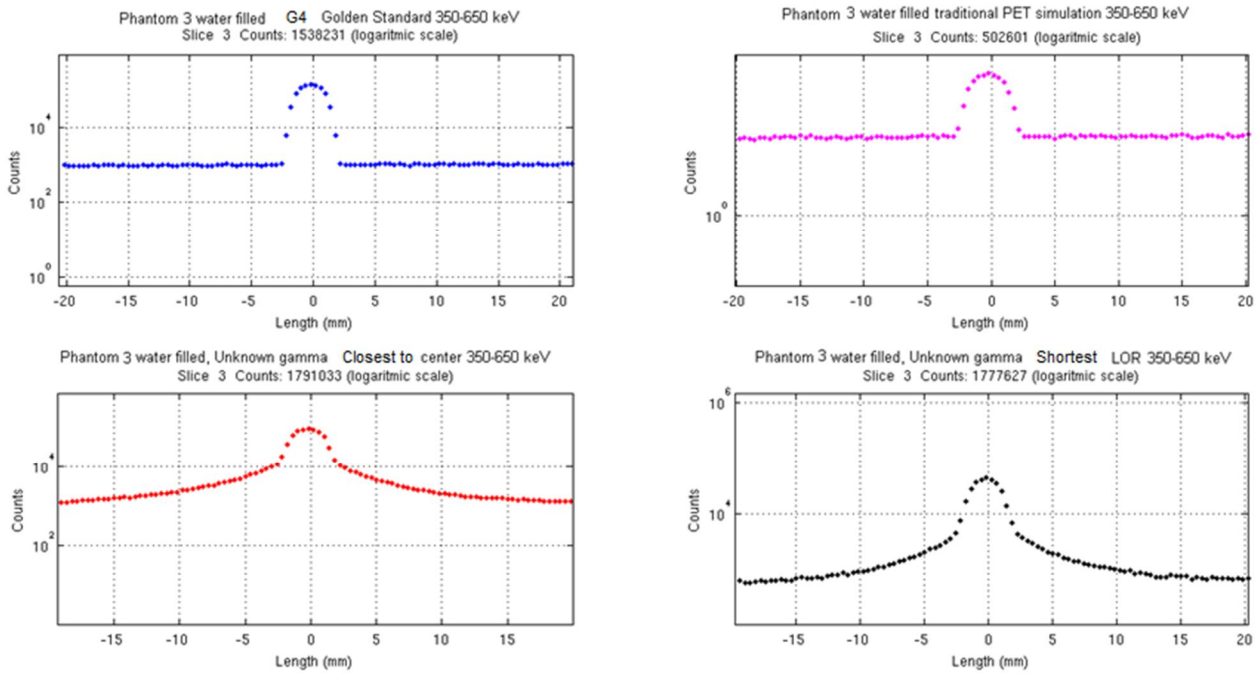

FIGURE 4.44: Phantom 3 count profiles of the sinograms in figure 4.43.

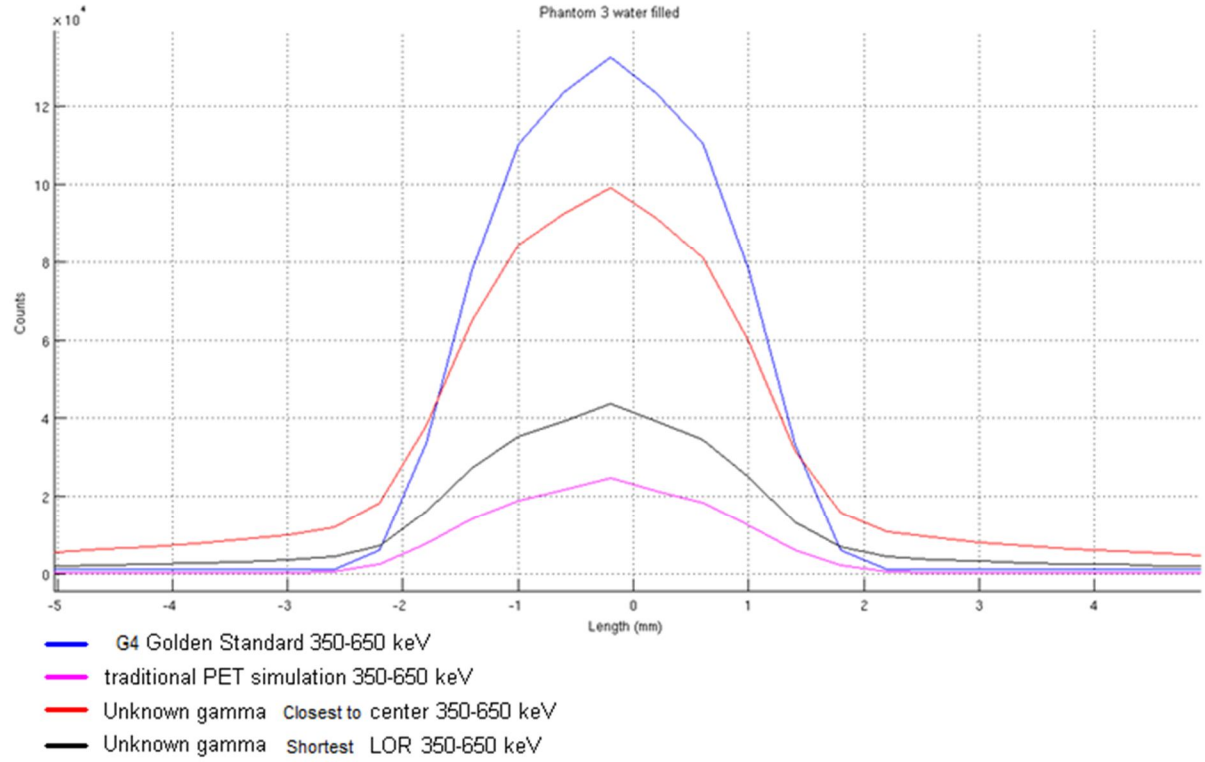

FIGURE 4.45: Phantom 3 superimposed count profiles of the sinograms in figure 4.43.

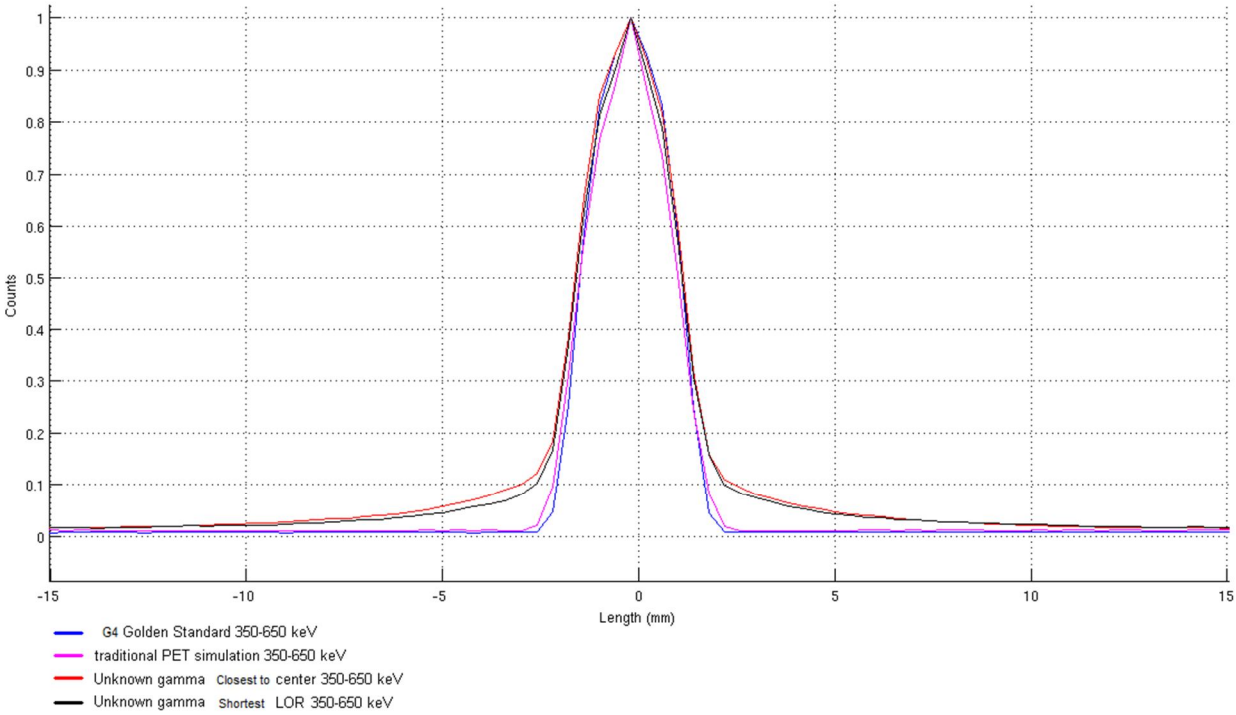

FIGURE 4.46: Phantom 3 superimposed normalized count profiles of the sinograms in figure 4.43.

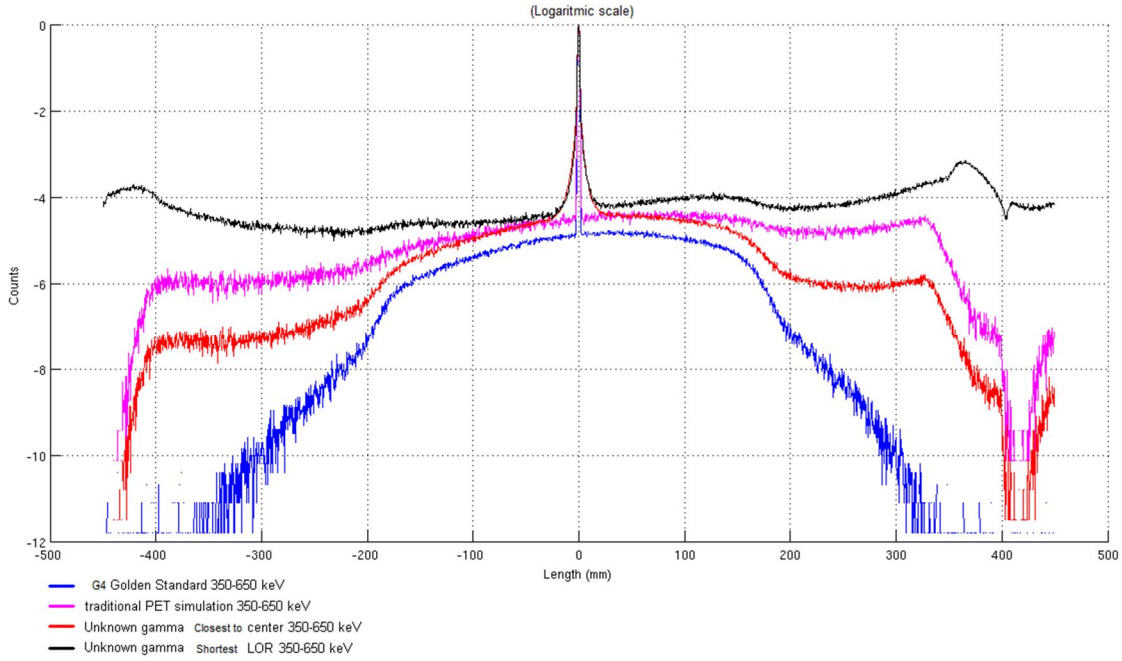

FIGURE 4.47: Phantom 3 superimposed normalized count profiles of the sinograms in figure 4.43 without zoom.

TABLE 4.8: Scatter fractions correspondent to the figure 4.37.

	A_{s1}	A_{s0}	A_{s2}	A_T	SF (%)
Golden Standard 350-650 keV	301351	10820	406810	819263	0.467404
Traditional PET 350-650 keV	129751	3300	223028	147173	0.707556
Unknown gamma closest to center 350-650 keV	477658	132869	636776	544379	0.696163
Unknown gamma shortest LOR 350-650 keV	590987	49610	942085	238333	0.869121

4.6.1.5 Event allocation analysis

This section is in accordance to the explanations given in section 4.5.2, regarding the ratios between the correctly and incorrectly allocated interactions.

TABLE 4.9: Comparison of the true positive and false positive percentages of the Compton tracing algorithms

	Closest to the center method with E window [350;650]keV	Shortest LOR method with E window [350;650]keV
Total Interactions	24174598	24174598
True Positive (True and accepted)	10729413	4004249
False positive (False but accepted)	13445185	20170349
True Positive (%)	44,383	16,5639
False positive (%)	55,617	83,4361

Chapter 5

Conclusions and future work

From the various results present in the previous chapter, we can assert which of the two Compton tracing algorithms is more adequate, by analyzing the effects of using the Compton interactions for image reconstruction regarding image contrast and the scatter fraction.

5.1 Conclusion

From the images presented in section 4.6.1.1., it is possible to verify that the gamma ray allocation algorithm creates a deviated artifact in the middle of the sinogram, whose origin we have been unable to deduce so far. However, despite the artifact in the sinogram, the final image does not present artifacts visible to the naked eye, and so both images are very identical, as table 4.2 confirms, with negligible variations between both contrast values C_{01}, C_{02} and C_{21} of the two images.

Section 4.6.1.2 allows us to confirm the proper functioning of the attenuation algorithm. Besides this, we can also verify that the image to the left explicitly shows the photon attenuation in water, where one can easily see that the photon attenuation diminishes for coincidences closer to the border of the phantom, and that as expected, the count rate significantly increases from the non-corrected sinogram, 1.4×10^7, to the corrected sinogram, 6.5×10^7.

Considering the image contrast analysis of phantom number 1 and the ratios presented in tables 4.3 and 4.4, we conclude that the Compton tracing algorithms do not considerably alter the images contrast, as all contrast ratios are very close to the Golden standard ratios values. Notwithstanding,

it is also possible to see from images 4.17 and 4.19, that the best images are the ones correspondent to the closest to the center algorithm, which are the more similar to the Golden standard ones. Moreover, we can also see that the closest to the center algorithm image shows an improvement of the traditional PET image.

Regarding the scatter fraction analysis from phantoms 2 and 3, the obtained results indicate that there are significant difference between the Compton tracing algorithms and the golden standard scatter fraction results (Table 4.5). Again the closest to the center algorithm presents better results than the shortest LOR algorithm, being the scatter fraction values of the closest to the center algorithm similar to the traditional PET scatter fraction values. Phantom three was simulated in order to ascertain that the better results of the closest to the center algorithm in phantom 2 were not derived from the fact that the activity cylinder is in the center of this phantom and thus favoring the closest to the center algorithm. Despite of this, the shortest LOR algorithm still presented worse results than the closest to the center algorithm. In addition to all these conclusions on scatter fractions, we can also see from images 4.25, 4.31, 4.39, and 4.46 that in these phantoms' case it is not advantageous to use the Compton tracing algorithms, because the traditional PET reconstruction presents a more discernible peak in the count profiles, and less interference due to incorrectly allocated LORs close to the activity cylinders.

Furthermore, from table 4.9 we can also verify that the closest to the center algorithm is better than the shortest LOR algorithm, and in spite of having a false positive acceptance percentage of 55,6%, the images show that these false positives are still close in space to the true first interactions in the detector, and therefore, they do not deteriorate appreciably the final images.

All things considered, the closest to the center algorithm shows potential for utilization in PET image reconstructions, and presents some improvements in relation to the traditional PET images for a given radiation dose administered to the patient. Contrary, it also suggests that a similar image quality can be obtained with a lower dose. On the other hand, the shortest LOR algorithm has always presented worse results and thus for further studies only the closest to the center algorithm is favored.

5.2 Future work

Although the improvements of the closest to the center algorithm in comparison to the traditional PET in phantom 1 are good, there are still many improvements to the algorithm that can be made, and may result in a better image quality for a given radiation dose administered to the patient.

First of all, for further work it is important that the gamma ray allocation algorithm is improved, so that the artifacts created by it are removed and thus do not interfere with the images obtained with Compton tracing algorithms.

Secondly, the closest to the center algorithm can also be enhanced, by implementing Compton kinematics consistency tests to compare the measured local energy depositions and their distribution in space with the equations 3.7 and 3.8. The interaction sequence that presented to have the closest energies to the computed ones would be accepted as the true one and thus the first interaction identified. This approach is discussed in Ref.[68] and [69].

Bibliography

[1] Webster J. “Positron Emission Tomography”. *Encyclopedia of Medical Devices and Instrumentation, Second Edition, Volume 5*. New Jersey: John Wiley & Sons, Inc. 2006.

[2] PE, Delbeke D, Bailey DL, Townsend DW, Maisey MN. *Positron Emission Tomography: Clinical Practice*. Springer-Verlag London Ltd. 2003.

[3] Philips sense and simplicity. [Online]. Available: http://www.search.philips.com/search/search?l=global&s=about&q=pet/mr&n=10

[4] *See what’s never been seen before: Philips Ingenuity TF PET/MR*. Philips sense and simplicity. Koninklijke Philips Electronics N.V. 2011. [Online]. Available: http://www.newscenter.philips.com/pwc_nc/be_nl/standard/about/news/downloads/ce-markering/Ingenuity_PETMR_Brochure_RSNA_2010.pdf

[5] Kaplan DA. *Philips Gets CE Mark for PET/MR System*. Diagnostic Imaging. 28 January 2011. [Online]. Available: http://www.diagnosticimaging.com/mri/content/article/113619/1785723?CID=rss#

[6] *Philips' PET/MR system receives CE mark.* Health Imaging. 26 January 2011. [Online]. Available: http://www.healthimaging.com/index.php?option=com_articles&article=25963

[7] H Zaidi, Ojha N, Morich M, Griesmer J, Hu Z, Maniawski P, Ratib O, Izquierdo-Garcia D, Fayad ZA, Shao L. *Design and performance evaluation of a whole-body Ingenuity TF PET-MRI system*. IOP Publishing. Phys. Med. Biol. 56 (2011) 3091–3106. DOI: 10.1088/0031-9155/56/10/013

[8] Eijk CWE. *Inorganic scintillators in medical imaging detectors.* Elsevier Science. Nuclear Instruments and Methods in Physics Research A 509 (2003) 17-25. DOI: 10.1016/S0168-9002(03)01542-0

[9] Kramer E, Ko J, Ponzo F, Mourtzikos K. *Positron Emission Tomography/Computed Tomography: A Disease-Oriented Approach*. Informa Healthcare USA, Inc. 2008.

[10] Moore J, Zouridakis G. *Biomedical Technology and Devices Handbook*. CRC Press LLC. 2004.

[11] Krane KS. *Introductory Nuclear Physics*. John Wiley & Sons, Inc. 1987.

[12] Knoll GE. *Radiation Detection and Measurement*. 3rd edition. John Wiley & Sons, Inc. 2000.

[13] Pedroso de Lima JJ. *Nuclear Medicine Physics*. Coimbra University Press and CRC Press. 2011.

[14] Suri JS, Wilson DL, Laxminarayan S. *Handbook of Biomedical Image Analysis, Volume 1: Segmentation models Part A*. Kluwer Academic/ Plenum Publishers. 2005.

[15] Podgorsak EB. *Radiation Physics for Medical Physicists.* Springer-Verlag Berlin Heidelberg. 2006.

[16] Saha GB. *Basics of PET Imaging: Physics, Chemistry, and Regulations*. Springer Science+Business Media, Inc. 2005.

[17] *Universidade de Coimbra - Centro de medicina nuclear ao nível "dos melhores" da Europa abre portas em 2009*. Público. 29 December 2008. [Online]. Available: http://www.publico.pt/Ci%C3%AAncias/centro-de-medicina-nuclear-ao-nivel-dos-melhores-da-europa-abre-portas-em-2009_1354390

[18] Bronzino JD. *Biomedical Engineering Handbook, 2nd edition, volume 1*. CRC Press in cooperation with IEEE Press. 2000.

[19] Ghosh P, Kelly M. *Expanding the power of PET with ^{18}F-Sodium Fluoride*. Siemens Medical Solutions. 2010. [Online]. Available: http://www.medical.siemens.com/siemens/en_US/gg_nm_FBAs/files/whtpap/wp_10_sodium_fluoride.pdf

[20] Vallabhajosula S, Solnes L, Vallabhajosula B. *A Broad Overview of Positron Emission Tomography Radiopharmaceuticals and Clinical Applications: What Is New?*. Elsevier Inc. Seminars in Nuclear Medicine. 2011. DOI: 10.1053/j.semnuclmed.2011.02.003.

[21] Meyer GJ, Waters SL, Coenen HH, Luxen A, Maziere B, Langström B. *PET radiopharmaceuticals in Europe: Current use and data relevant for the formulation of summaries of product characteristics (SPCs)*. European Journal of Nuclear Medicine. Vol. 22, No. 12, December 1995 - Springer-Verlag 1995. DOI: 10.1007/BF01791152.

[22] *Cavaco inaugura Instituto de Ciências Nucleares em Coimbra.* Ciência Hoje. 3 September 2011. [Online]. Available: http://www.cienciahoje.pt/index.php?oid=30852&op=all

[23] Miyake Y, Iida H, Hayashida K, Ishida Y. *New method for the synthesis of ^{15}O-labeled carbon monoxide and ^{15}O-labeled dioxide for rapid supply in clinical use*. Elsevier B.V. International Congress Series 1265 (2004) 93–96. DOI:10.1016/j.ics.2004.04.060

[24] Kutz M. *Biomedical Engineering and Design Handbook, 2nd edition, Volume 2.* McGraw-Hill Companies, Inc. 2009

[25] Leroy C, Rancoita PJ, *Principles of Radiation Interaction in Matter and Detection, 2nd edition*. World Scientific Publishing Co. Pte. Ltd. 2009.

[26] Committee on the Mathematics and Physics of Emerging Duynamic Biomedical Imaging, Board on Mathematical Sciences, Board on Physics and Astronomy, Commission on Physical Sciences, Mathematics and applications, National Research Council, Board on Biobehavioral Sciences and Mental Disorders, Institute of Medicine. *Mathematics and Physics of Emerging Biomedical Imaging*. Washington D.C.: National Academy Press. 1996.

[27] Bryman D, *Development of Liquid Xenon detectors for PET*, TRIUMF Liquid Xenon Positron Emission Tomography. 8 December 2009. [Online]. Available: https://lixenon.triumf.ca/InternalDocuments/Talks/Bryman-ComptonWorkshop2008.pdf/view

[28] Vallabhajosula S. *Positron Emission Tomography Radiopharmaceuticals for Imaging Brain Beta-Amyloid*. Elsevier Inc. Seminars in Nuclear Medicine 41:283-299. 2011. DOI: 10.1053/j.semnuclmed.2011.02.005

[29] Feng DD. *Biomedical Information Technology*. Academic Press from Elsevier Inc. 2008.

[30] Raylman RR, Majewski S, Kross B, Popov V, Proffitt J, Smith MF, Weisenberger AG, Wojcik R. *Development of a dedicated positron emission tomography system for the detection and biopsy of breast cancer*. Elsevier B.V. Nuclear Instruments and Methods in Physics Research A 569 (2006) 291–295. DOI:10.1016/j.nima.2006.08.052.

[31] Oliveira N, Matela N, R.Bugalho R, Ferreira N, Almeida P. *Optimization of 2D image reconstruction for positron emission mammography using IDL.* Elsevier Ltd. Computers in Biology and Medicine 39 (2009) 119 – 129. DOI:10.1016/j.compbiomed.2008.11.011.

[32] Kim CL, McDaniel DL, Ganin A. *Time-of-Flight PET Detector Based on Multi-Pixel Photon Counter and Its Challenges.* IEEE Transactions on Nuclear Science, Vol. 58, No. 1, February 2011. DOI: 10.1109/TNS.2010.2100085.

[33] Eriksson L, Townsend D, Eriksson M, Casey ME, Conti M, Bendriem B, Nutt R. *The NEC dependence of different scintillators for Positron Emission Tomography*. IEEE. Nuclear Science Symposium Conference Record. October 2004. DOI: 10.1109/NSSMIC.2004.1466704.

[34] Surti S, Karp JS, Muehllehner G, Raby PS. *Investigation of Lanthanum Scintillators for 3-D PET.* IEEE Transactions on Nuclear Science, Vol. 50, No. 3, June 2003. DOI: 10.1109/TNS.2003.812450.

[35] Thompson CJ, Murthy K, Y Picard Y, Weinberg IN, Mako R. *Positron Emission Mammography (PEM): A Promising Technique for Detecting Breast Cancer*. Nuclear Science Symposium and Medical Imaging Conference, 1994 IEEE Conference Record, page(s): 1893 - 1897 vol.4. DOI: 10.1109/NSSMIC.1994.474696.

[36] *Positron emission mammography effective in detecting breast cancer*. News Medical. 3 December 2008. [Online]. Available: http://www.news-medical.net/news/2008/12/03/43687.aspx

[37] *New Mammography Technology Effective in Detecting Breast Cancer*. RedOrbit. 1 December 2008. [Online]. Available: http://www.redorbit.com/news/health/1606091/new_mammography_technology_effective_in_detecting_breast_cancer/index.html

[38] Azevedo V. *Portugueses lançam nova máquina contra o cancro da mama*. Expresso notícias. 15 January 2011. [Online]. Available: http://aeiou.expresso.pt/video-portugueses-lancam-nova-maquina-contra-o-cancro-da-mama=f625900

[39] *A nova máquina portuguesa contra o cancro da mama*. Expresso notícias. 15 January 2011. [Online]. Available: http://umonline.uminho.pt/uploads/clipping/NOT_38282/2011011523c3d915012011113700.pdf

[40] Chen Y, Glick SJ, King MA. *Compensation of Patient Motion in PET Using a Rotator and List-Mode Reconstruction*. IEEE Nuclear Science Symposium Conference Record, M06-4, 2007. DOI: 10.1109/NSSMIC.2007.4436700.

[41] Daube-Witherspoon ME, Matej S, Werner ME, Surti S, Karp JS. *Comparison of List-Mode and DIRECT Approaches for Time-of-Flight PET Reconstruction*. IEEE Nuclear Science Symposium Conference Record (NSS/MIC), 2010. DOI: 10.1109/NSSMIC.2010.5874184.

[42] Moses WW. *Advantages of Improved Timing Accuracy in PET Cameras using LSO Scintillator*. IEEE Transactions on Nuclear Science LBNL-51788. 27 October 2003. DOI: 10.1109/NSSMIC.2002.1239645.

[43] Nannan Cao N, Huesman RN, Moses WW, Qi J. *Detection performance analysis for time-of-flight PET*. IOP sciences. Phys. Med. Biol. 55 6931, 2010. DOI: 10.1088/0031-9155/55/22/021.

[44] Casey ME. *Improving PET With HD•PET + Time of Flight*. Siemens Medical Solutions USA, Inc. 2008. [Online]. Available: http://www.medical.siemens.com/siemens/en_GB/gg_nm_FBAs/files/brochures/2008/ultraHD-PET_White_Paper.pdf

[45] *TruFlight Select PET/CT*. Philips sense and simplicity. [Online]. Available: http://www.healthcare.philips.com/main/products/nuclearmedicine/products/pet/truflightselect/index.wpd

[46] *Gemini TF PET/CT*. Philips sense and simplicity. [Online]. Available: http://www.healthcare.philips.com/main/products/nuclearmedicine/products/geminitf/index.wpd

[47] Ito M, Hong SJ, Lee JS. *Positron Emission Tomography (PET) Detectors with Depth-of-Interaction (DOI) Capability*. The Korean Society of Medical & Biological Engineering and Springer 2011. Biomed Eng Lett (2011) 1:70-81. DOI: 10.1007/s13534-011-0019-6.

[48] Pichler B, Lorenz E, Mirzoyan R, Pimp W, Roder F, Schwaiger M, Ziegler SI. *Performance Test of a LSO-APD PET Module in a 9.4 Tesla Magnet*. IEEE Nuclear Science Symposium, 1997. DOI: 10.1109/NSSMIC.1997.670533.

[49] Hong SJ, Kim CM, Cho SM, Woo H, Ko GB, Kwon SI, Rhee JT, Song IC, Lee JS. *A Feasibility Study on the Use of Optical Fibers for the Transfer of Scintillation Light to Silicon Photomultipliers*. IEEE Transaction on Nuclear Science, Vol. 58, No. 3, June 2011. DOI: 10.1109/TNS.2011.2112778.

[50] Delfino EP, Majewski S, Raylman RR, Stolin A. *Towards 1mm PET Resolution Using DOI Modules Based on Dual-Sided SiPM Readout*. IEEE

Nuclear Science Symposium Conference Record (NSS/MIC), 2010. DOI: 10.1109/NSSMIC.2010.5874446.

[51] Kyba CC, Wiener RI, Newcomer FM, Member, Berg RV, Dressnandt N, Karp JS. *Timing Measurements from a TOF-PET Scanner Using Local PMT Triggering*. 2007 IEEE Nuclear Science Symposium Conference Record M22-4. DOI: 10.1109/NSSMIC.2007.4437030.

[52] Shah KS, Glodo J, Klugerman M, Moses WW, Derenzo SE, Weber MJ. *LaBr3:Ce Scintillators for Gamma Ray Spectroscopy*. Transactions on Nuclear Science. IEEE. 2003. DOI: 10.1109/TNS.2003.820614.

[53] Surti S, Karp JS, Muehllehner G. *Image quality assessment of LaBr3-based whole-body 3D PET scanners: a Monte Carlo evaluation*. IOP Publishing Ltd. Phys. Med. Biol. 49 (2004) 4593–4610. DOI: 10.1088/0031-9155/49/19/010.

[54] Thers D, Breskin A, Carlier T, Chechik R, Couturier O, Cussonneau JP, Ferrer L, Grignon C, Luquin L, Métivier V, Peskov V, Phéron F, Servagent N, Vasseur A. *A proposal for a high performance gamma camera based on liquid xenon converter and gaseous photomultiplier for PET*. Inventeurs du Monde Numérique. [Online]. Available: http://hal.inria.fr/docs/00/06/80/59/PDF/ProceedingDThers.pdf

[55] Tsoulfanidis Nicholas. *Measurement and Detection of Radiation, second edition*. Taylor & Francis publishers. 1995.

[56] Chepel V, Lopes MI. *Electronic Excitations in Liquefied Rare Gases, chapter 11 - Rare Gas Liquid Detectors*. American Scientific Publishers. 2005.

[57] *XCOM: Photon Cross Sections Database*. NIST Physical Measurement Laboratory. [Online]. Available: http://www.nist.gov/pml/data/xcom/index.cfm

[58] Allison J. *Geant4 Developments and Applications*. IEEE Transactions on Nuclear Science, Vol. 53, No. 1, February 2006. DOI: 10.1109/TNS.2006.869826.

[59] Rodrigues P, Moura R, Peralta L, Pia MG, Trindade A, Varela J. *GEANT4 Applications and Developments for Medical Physics Experiments*. IEEE Transactions on Nuclear Science, Vol. 51, No.4, 1412 – 1419, 16 August 2004. DOI: 10.1109/TNS.2004.832314.

[60] *Atomic Weights and Isotopic Compositions for All Elements*. NIST Physical Measurement Laboratory. [Online]. Available: http://physics.nist.gov/cgi-bin/Compositions/stand_alone.pl?ele=&ascii=html&isotype=some

[61] *NEMA Standards Publication NU 2-2000 Performance Measurements of Positron Emission Tomograph*. National Electrical Manufacturers Association. 1 September 2000.

[62] Prokhorov AV. *Pólya distribution*. SpringerLink. [Online]. Available: http://eom.springer.de/p/p073540.htm

[63] Feller W. *An Introduction to Probability Theory and Its Applications, 3rd edition, volume 1*. John Wiley & Sons, Inc. 1968.

[64] Zwillinger D. *Standard Mathematical Tables and Formulae, 31st Edition*. Chapman & Hall/CRC Press LLC. 2003.

[65] *Negative Binomial Distribution.* Mathworks Matlab. [Online]. Available: http://www.mathworks.com/help/toolbox/stats/brn2ivz-101.html

[66] Miceli A, Amaudruz P, Benard F, Bryman DA, Kurchaninov L, Martin JP, Muennich A, Retiere F, Ruth TJ. Sossi V, Stoessl AJ. *Liquid Xenon Detectors for Positron Emission tomography.* 7 April 2011.

[67] NIST Physical_Measurement_Laboratory. [Online]. Available: http://physics.nist.gov/cgi-bin/Xcom/xcom3_2

[68] Boggs SE, Jean P. *Event reconstruction in high resolution Compton telescopes*. Astron. Astrophys. Suppl. Ser. 145, 311-321 (2000). DOI: 10.1051/aas:2000107.

[69] Oberlack UG, Aprile E, Curioni A, Egorov V, Giboni KL. *Compton scattering sequence reconstruction algorithm for the liquid xenon gamma-ray imaging telescope (LXeGRIT)*. SPIE. 2000. DOI: 10.1117/12.407578.

[70] Chepel V, Solovov V, van der Marel J, Lopes MI, Janeiro L, Santos D, Ferreira Marques R, Policarpo AJPL. *The Liquid Xenon detector for PET: recente results*. IEEE Transactions on Nuclear Science, Vol. 46, No.4, August 1999. DOI: 10.1109/23.790822.

[71] Bailey DL, Townsend DW, Valk PE, Maisey MN. *Positron Emission Tomography: Basic Sciences*. Springer-Verlag London Limited. 2005.